Max-Planck-Institut
für Kolloid- und Grenzflächenforschung

Universität Potsdam

Max-Planck-Institut für Kolloid und Grenzflächenforschung

Abteilung für Biomaterialien

Forming magnetic chain with the help of biological organisms

Dissertation

zur Erlangung des akademischen Grades

"doctor rerum naturalium"

(Dr. rer. nat.)

in der Wissenschaftsdisziplin "Molekulare Biotechnologie"

eingereicht an der

Mathematisch-Naturwissenschaftlichen Fakultät

der Universität Potsdam

von

Agata Olszewska

Potsdam, den 30. September 2015

Published online at the
Institutional Repository of the University of Potsdam:
URN urn:nbn:de:kobv:517-opus4-89767
http://nbn-resolving.de/urn:nbn:de:kobv:517-opus4-89767

Abstract

Magnetite nanoparticles and their assembly comprise a new area of development for new technologies. The magnetic particles can interact and assemble in chains or networks. Magnetotactic bacteria are one of the most interesting microorganisms, in which the assembly of nanoparticles occurs. These microorganisms are a heterogeneous group of gram negative prokaryotes, which all show the production of special magnetic organelles called magnetosomes, consisting of a magnetic nanoparticle, either magnetite (Fe_3O_4) or greigite (Fe_3S_4), embedded in a membrane. The chain is assembled along an actin-like scaffold made of MamK protein, which makes the magnetosomes to arrange in mechanically stable chains. The chains work as a compass needle in order to allow cells to orient and swim along the magnetic field of the Earth.

The formation of magnetosomes is known to be controlled at the molecular level. The physico–chemical conditions of the surrounding environment also influence biomineralization. The work presented in this manuscript aims to understand how such external conditions, in particular the extracellular oxidation reduction potential (ORP) influence magnetite formation in the strain *Magnetospirillum magneticum* AMB-1. A controlled cultivation of the microorganism was developed in a bioreactor and the formation of magnetosomes was characterized.

Different techniques have been applied in order to characterize the amount of iron taken up by the bacteria and in consequence the size of magnetosomes produced at different ORP conditions. By comparison of iron uptake, morphology of bacteria, size and amount of magnetosomes per cell at different ORP, the formation of magnetosomes was inhibited at ORP 0 mV, whereas reduced conditions, ORP – 500 mV facilitate biomineralization process.

Self-assembly of magnetosomes occurring in magnetotactic bacteria became an inspiration to learn from nature and to construct nanoparticles assemblies by using the bacteriophage M13 as a template. The M13 bacteriophage is an 800 nm long filament with encapsulated single-stranded DNA that has been recently used as a scaffold for nanoparticle assembly. I constructed two types of assemblies based on bacteriophages and magnetic nanoparticles. A chain – like assembly was first formed where magnetite nanoparticles are attached along the

phage filament. A sperm – like construct was also built with a magnetic head and a tail formed by phage filament.

The controlled assembly of magnetite nanoparticles on the phage template was possible due to two different mechanism of nanoparticle assembly. The first one was based on the electrostatic interactions between positively charged polyethylenimine coated magnetite nanoparticles and negatively charged phages. The second phage –nanoparticle assembly was achieved by bioengineered recognition sites. A mCherry protein is displayed on the phage and is was used as a linker to a red binding nanobody (RBP) that is fused to the one of the proteins surrounding the magnetite crystal of a magnetosome.

Both assemblies were actuated in water by an external magnetic field showing their swimming behavior and potentially enabling further usage of such structures for medical applications. The speed of the phage - nanoparticles assemblies are relatively slow when compared to those of microswimmers previously published. However, only the largest phage-magnetite assemblies could be imaged and it is therefore still unclear how fast these structures can be in their smaller version.

Zusammenfassung

Magnetit-Nanopartikel (Fe_3O_4) und deren Anordnungen umfassen einen neuen Bereich in der Entwicklung neuer Technologien. Diese magnetischen Teilcheninteragieren miteinander und unter bestimmten Umständen lassen sie sich in Ketten anordnen. Magnetotaktische Bakterien stellen eine Gruppeinteressanter Mikroorganismen dar, in welchen ebendiese kettenförmige Anordnung von Nanopartikeln vorkommt. Diese Mikroorgansimen gehören zu einer heterogenen Gruppe an Gram negativen Prokaryoten, welche die Produktion von speziellen magnetischen Organellen, den sogenannten Magnetosomen, aufweist. Die Magnetosomen bestehen entweder aus Magnetit- oder Greigit (Fe_3S_4)- Nanopartikeln, welche in einer Membran eingebettet sind. Die Kette ist entlang eines Aktin ähnlichen Gerüstes angeordnet, welches aus dem Protein MamK besteht und dafür verantwortlich ist, dass sich die Magnetosomen in mechanisch stabilen Ketten arrangieren können. Diese Ketten fungieren als Kompass Nadeln und ermöglichen es den Zellen sich entlang des Magnetfeldes der Erde zuorientieren.

Es ist bekannt, dass die Bildung der Magnetosomen auf molekularer Ebene kontrolliert wird. Die physiko-chemischen Bedingungen der direkten Umgebung beeinflussen die Biomineralisierung. Die in diesem Manuskript vorgestellte Arbeit setzt sich zum Ziel, die äußeren Bedingungen, im Speziellen der Einfluss des extrazellulären Oxidations- und Reduktions-Potentials (ORP) auf die Magnetit Bildung im Bakterienstamm *Magnetospirillum magneticum* AMB-1 besser zu verstehen. Eine kontrollierte Anzucht des Mikroorganismus wurde im Bioreaktor entwickelt und die Magnetosomenbildung wurden charakterisiert.

Unter verschiedenen ORP-Bedingungen wurde untersucht, wieviel Eisen von den Bakterien aufgenommen wird und welche Auswirkungen das auf die Zahl und Größe der Magnetosomen hat. Untersucht man die Parameter Eisenaufnahme, Morphologie der Bakterien, Größe und Menge der Magnetosomen pro Zelle kommt man zu dem Schluss, dass die Magnetosomenbildung bei einem ORP von 0 mV inhibiert wird, wobei reduzierende Bedingungen bei einem ORP von -500 mV den Biomineralisationsprozess fördern.

Inspiriert von der Fähigkeit der Selbstorganisation von Magnetosomen in MTB wurde versucht Nanopartikel-Anordnungen mit Hilfe des Bakteriophagen M13 als Vorlage zu konstruieren. Der Bakteriophage M13 ist ein 800 nm langes Filament mit eingekapselter

einzelsträngiger DNA und wurde schon zuvor als Gerüst für Nanopartikel-Konstrukte verwendet. Ich habe zwei Typen von Anordnungen basierend auf Bakteriophagen und magnetischen Nanopartikeln konstruiert. Es wurde eine kettenartige Struktur, an der magnetische Nanopartikel entlang eines Phagenfilamentes angebracht sind und ein spermienähnliches Konstrukt mit einem magnetischen Kopf und einem Phagenfilament als Schwanz, entwickelt.

Um eine kontrollierte Anordnung von Magnetit-Nanopartikeln an den Phagen zu ermöglichen, wurden zwei verschiedene Ansätze verfolgt. Der erste basierte auf elektrostatischen Wechselwirkungen zwischen den mit positiv geladenem Polyethylenimin dekorierten Magnetit-Nanopartikeln und den negativ geladenen Phagen. Das zweite Phagen-Nanopartikel-Konstrukt wurde mit Hilfe von biologisch veränderten Erkennungsseiten hergestellt. Die Phagen weisen ein mCherry Protein auf, welches als Verbindungsstück für den red binding nanobody (RBP) verwendet wurde. Dieser wurde mit einem der Proteine fusioniert, welches die Magnetit Kristalle der Magnetosomen umhüllt.

Beide Konstrukte wurden mit Hilfe eines externen Magnetfeldes im Wasser angeregt, wobei sich ihr Schwimmverhalten und das Potential für medizinische Anwendungen dieser Strukturen zeigten. Die Geschwindigkeit der Phagen-Nanopartikel-Konstrukte war im Vergleich zu den bisher veröffentlichten Mikroschwimmern relativ langsam. Es konnten jedoch nur die größten Phagen-Magnetit-Konstrukte visualisiert werden, wodurch die Geschwindigkeit der kleineren Versionen dieser Strukturen noch unklar bleibt.

Table of Contents

1. Introduction

Magnetite nanoparticles exhibit perhaps a major field of interest in the material science, chemistry and physics. Nanoparticles of the iron oxide magnetite (Fe_3O_4) are widely exploited for diverse applications, *e.g*. in magnetic data storage, ferrofluids, as contrast agents in magnetic resonance imaging, in drug delivery or cancer treatment by hyperthermia therapy [1] [2]. Due to size dependency on magnetic properties of particles, much research has focused on the formation of magnetic particles with controlled size [3]. Functional groups on the surface of the particles can cause them to interact and assemble in a certain way that together leads to assembly of the particles in chains or networks [4]. Assemblies of nanoscale components are important for many areas of science and as a drive to scale down new technologies. The organization of nanoscale magnetic particles opens a new field of technologies through the controlled fabrication of mesoscopic materials with unique magnetic properties [5].

Important characteristic of the chains made of magnetic nanoparticles is their flexibility and ability to change conformation when the external magnetic fields are applied. Dreyfus et al. showed that micrometer-sized paramagnetic particles connected by polymer bridges are capable of propelling themselves through a fluid *via* bending motions [6]. Goubault et al. demonstrated that long flexible chains made of superparamagnetic particles linked by polymer chains, can adopt under magnetic field a hairpin configuration [7]. The ability to control minerals formation by living organisms is widespread all over the six biological kingdoms. This process takes the name of biomineralization and it is made in order to fulfill a different and very diverse set of functions, from defense to mechanical support and navigation. Many living organisms have developed particular systems that precisely regulate the chemical environment where the biomineralization takes place. Therefore the produced minerals show outstanding properties, such as particular shapes and crystallinity, which are often not found in their inorganic or synthetized counterparts [8]. Iron minerals are also a highly diverse group found in many different living organisms, from bacteria to vertebrates, responsible for different functions [9]. Many organisms store iron as a poorly-crystalline form ferrihydrite. Highly crystalline iron minerals are found in the radular teeth of certain mollusks, such as limpets and chitons [10]. Magnetotactic bacteria (MTB) are one of such an example. These microorganisms are an heterogeneous group of gram negative prokaryotes, found in various aquatic environments, which all show the production of special magnetic organelles called magnetosomes [11]. Those organelles consist of a magnetic nanoparticle, which could either

be a crystal of magnetite (Fe_3O_4) or greigite (Fe_3S_4), enveloped in a lipid bilayer containing different proteins [12]. Magnetosomes are arranged in mechanically stable chains. This allows the bacteria to orientate itself with the magnetic field and to swim along the geomagnetic field lines. MTB have attracted a lot of interest in research due to the particularity of their magnetic organelles and the implications that they could have for different branches of science. From their ecological role in the cycle of elements such as iron and sulphur, to the study of the process of biomineralization of the magnetic nanoparticles, and considering the different engineering applications under development; MTB represent an exciting discovery that could lead to interesting future developments.

Natural scaffolds have been recently interesting as a promising approach for building nanostructures, including chains of nanoparticles [1]. In particular, the bacteriophage M13 has been widely used for constructing phage – based materials for biomedical applications, such as biosensing [13] [14], drug delivery, and antibiotic therapies [15]. The M13 bacteriophage is 6 nm in diameter and ~ 800 nm long virus [16]. The phage structure is robust to heat, organic solvents, acidic or alkali conditions [17]. Therefore, the phage filaments could serve as promising scaffold for nanoparticles assembly into chain-like structures.

Driven by these practical needs, efforts have been conducted towards functional microscale assemblies, in particular towards microscale robots. Challenges associated with achieving microscale robots are mostly dedicated to their actuating systems since on board control is practically impossible [18]. The most common mechanisms are magnetic actuation [19], electrostatic actuation [20], as well as biologic propulsion using for example chemotaxisas the actuating system [21]. Such structures like phage – nanoparticle assembly could be actuated in the external magnetic fields and serve as a promising micro robot in future work.

1.1. Objectives and scope of work

The general objective of this work is to better understand if external conditions, such as extracellular oxidation – reduction potential (ORP) conditions can influence magnetite formation *Magnetospirillum magneticum* AMB-1 as it is seen for chemical process. Specifically, the aim of this work was to develop and establish a system, which enables the investigation of the effects of specified redox potential of the growth medium on the formation of magnetosomes in *Magnetospirillum magneticum* AMB-1 strain. In principle, such change in redox potential of the surrounding medium could have a strong influence on the growth of the bacteria, iron uptake process and finally size, morphology of biomineralized nanoparticles. This would have one important impact – longer chains of magnetosomes and in consequence higher yield of magnetosomes, which is of interest for further potential applications, where the use of magnetosomes is restrained due to the low production yield. As such conditions cannot be obtained by standard flask cultivation, the system has to enable the study in a strictly controlled environment, therefore the experiments were conducted in a bioreactor, where all of the significant parameters, such as pH, temperature, ORP and O_2 could be continuously monitored and kept stable trough feedback systems.

The chemical stability of magnetite is restricted to a limited E_h – pH ratio. Magnetite typically forms at E_h values from - 200 mV to – 400 mV and above pH > 8 [22]. Biological systems are limited to rather mild alkaline conditions. It is not understood how MTB are able to for the appropriate iron phase under the very soft physiological conditions. Compartmentalization might allow them to control local pH and redox potential in order to precipitate magnetite phase. Syntheses of magnetic nanoparticles, in magnetotactic bacteria require strict control over these parameters. Thus, the experiments were investigated anaerobically, under neutral pH 7, reduced (ORP – 500 mV) and oxidized (ORP 0 mV) conditions.

The second part of the thesis deals in particular with magnetic nanostructures, the basics of their assembly and the possibility of actuating them by external magnetic fields. The biotemplate used in this study was composed of flexible filaments of bacteriophage M13. The nanoparticle chain like formation was achieved by studying the electrostatic interactions between magnetic nanoparticles and phages; and establishing optimal conditions for their self-assembly. Two second type of phage-nanoparticle assembly was constructed from the magnetic nanoparticle as a head and M13 phage filament as a tail.

The formation of such assembly required genetic modifications in order to build a linker between the phage and the nanoparticles. Phage display is a powerful technique that enabled displaying mCherry protein on the p3 protein of the phage. The magnetic head of the construct was built from magnetite nanoparticles called magnetosomes, which were isolated from magnetotactic bacterium *Magnetospirillum gryphiswaldense*. These so called MamC-RBP magnetosomes possess a red fluorescent protein (RFP) – binding nanobody (RBP) fused to the magnetosome membrane (MM) protein MamC. The isolated magnetosomes recognize their antigen *in vitro* and therefore could bind to mCherry protein displayed on the phage. Methods such as transmission electron microscopy were used for visualization of phage – nanoparticle assembly. Fluorescent labeling was utilized to detect phage filaments; atomic force microscopy was investigated for topography measurements. Both types of assembly were actuated by external magnetic fields and their propelling behavior was analyzed. The propulsion speeds of phage-nanoparticles assemblies were calculated from videos recorded with the high speed camera.

2. Background and Methods

2.1. Magnetosome chains in magnetotactic bacteria

Magnetotactic bacteria (MTB) are a heterogeneous group of gram negative prokaryotes, found in various aquatic environments, which all show the production of special magnetic organelles, called magnetosomes [23]. Those organelles consist of a crystal either of magnetite (Fe_3O_4) or greigite (Fe_3S_4), enveloped in a lipid bilayer containing different proteins [24]. Magnetosomes are arranged in chains, and fixed within the cell; this allows the bacteria to orient and migrate along the Earth magnetic field [22]. MTB comprise a varied group of organisms considering their morphology, phylogeny and metabolism. Salvatore Bellini was the first one who described the observation of bacteria, in which the swimming direction was affected by magnetic fields. His research was only published recently [21, 22]. It was Richard Blakemore who in 1975 firstly reported MTB species [27]. Since then, a great amount of different species and phyla were found. Different cell morphologies, ranging from cocci, spirilla, vibrios, rods and ovoid shapes [22] and even multicellular MTB have been observed [28]. Such as diversity is also genetically reflected; according to the analysis of the 16s ribosomal DNA genes, MTB are the part of five different Phyla, belonging to the proteobacteria Phylum, specifically *Alpha*- *Beta*- and *Delta*-proteobacteria. Some are found to be part of the *Nitrospirae*, while others to *Candidus* OP3 group [29] (Figure 2.1). MTB cover a wide range of metabolic pathways; all of them so far observed are either obligate anaerobic, facultative anaerobic, or obligate micro-aerobic. All known MTB are only able to undertake respiratory processes, with just one exception (*Desulfovibrio magneticus*), which is able to perform fermentation processes [30].

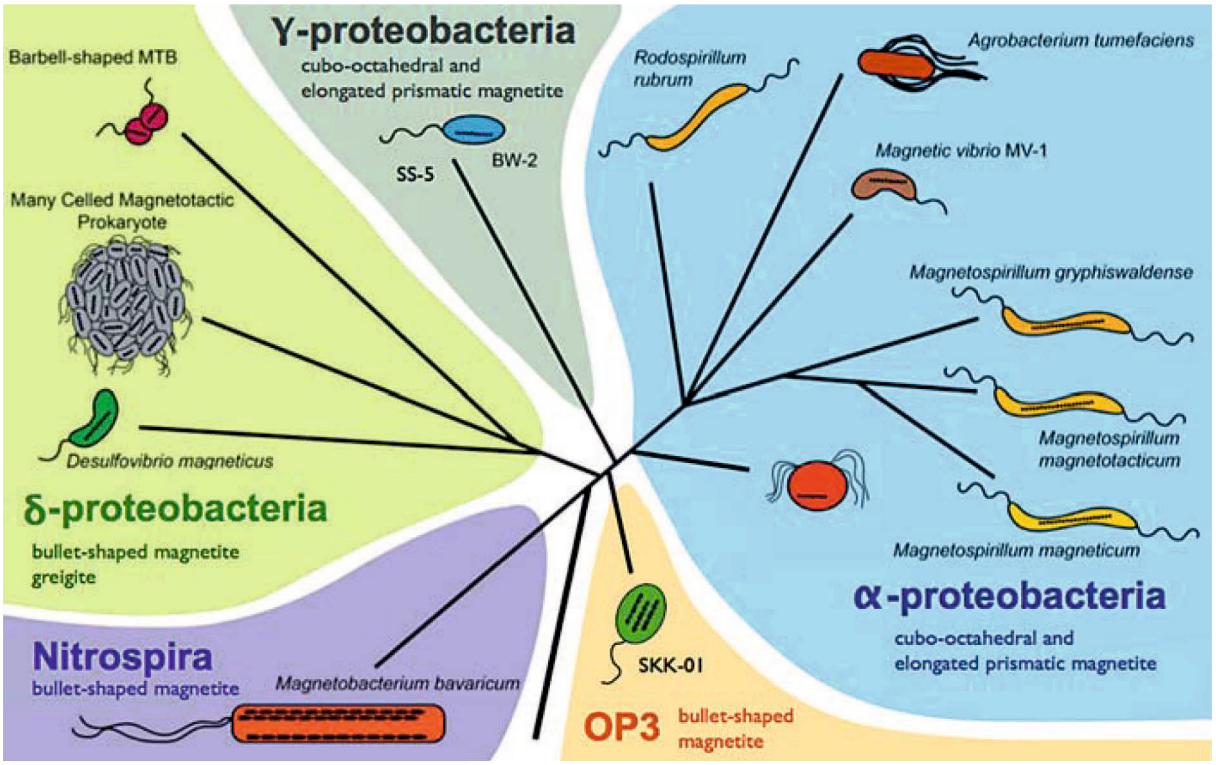

Figure 2.1 Phylogenetic distribution of known cultured and uncultured magnetotactic bacteria. The five major evolutionary lineages produce magnetosomes with different shapes. Adapted with permission [31]**.**

MTB are ubiquitous in different aquatic environments. They were found so far in environments, ranging from marine to freshwater, excluding really acidic water ponds and thermal springs. They are often abundant at the oxic – anoxic transition zone (OATZ).

Chains of magnetosomes

Magnetosomes are intracellular crystals of either magnetite (Fe_3O_4) or greigite (Fe_3S_4) surrounded by a protein lipid membrane [32]. The high degree of control on the biomineralization process gives rise to particles formation with controlled physical and magnetic properties. The geometry of magnetosomes is known to be specie-specific; different species produce magnetosomes having different shapes. Three general magnetosome crystal morphologies have been observed: cubooctahedral, elongated prismatic and bullet- or tooth-shaped [33]. The chemical composition of the crystals was reported to be precisely controlled by the bacteria, showing a high purity, not found in abiotic synthesized minerals [34].

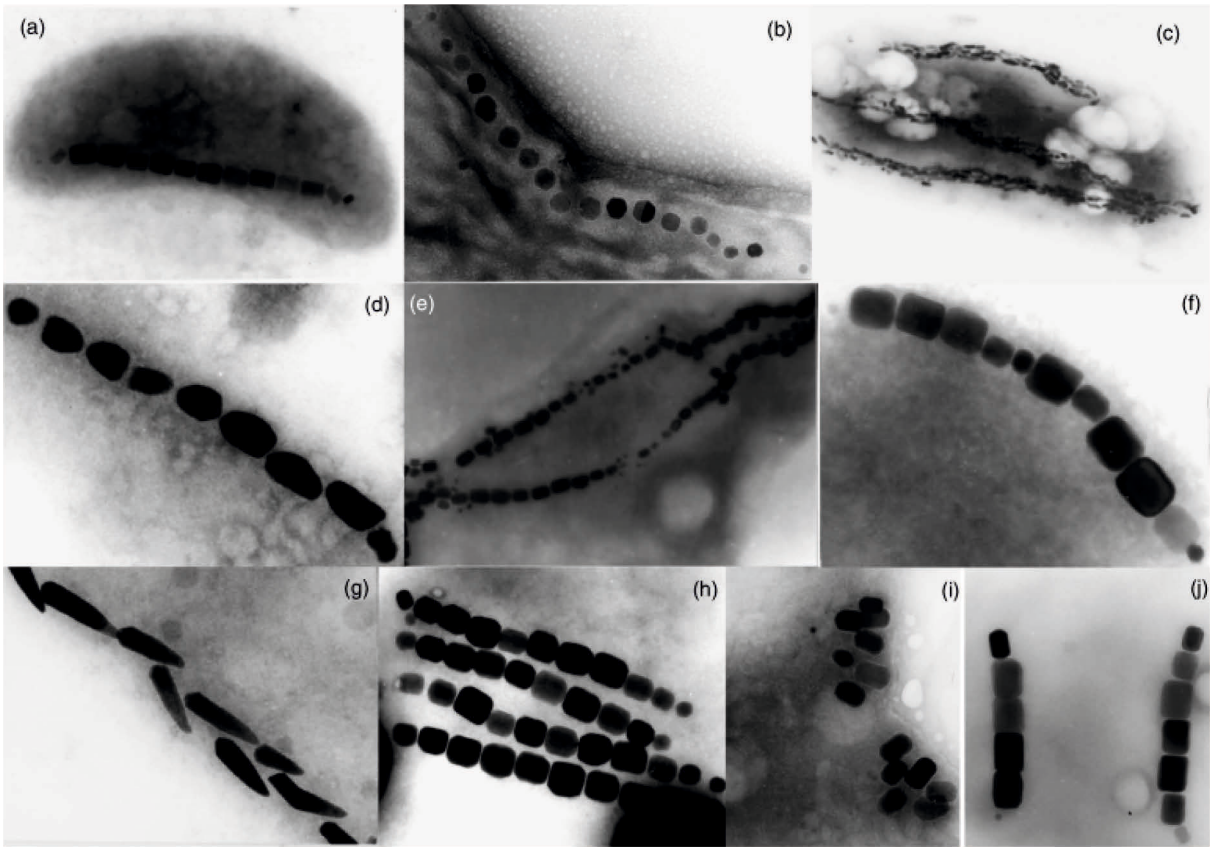

Figure 2.2 Diversity of magnetosome crystals and arrangements in various MTB. Image was adapted with permission from Schüler (2008).

The 4 nm thick bilayer surrounding the magnetite crystal, called magnetosome membrane (MM), is mainly composed of different phospholipids with various proteins embedded. It is known that the magnetosome membrane originates from an invagination of the cytoplasmic membrane; this provides a first-regulated small environment to start the nucleation of the crystal [35]. The magnetic properties are strictly determined by the domain state of the particle, which is dependent on grain size and aspect ratio [36]. It is know that these magnetic nanoparticles have dimensions comprised between 35 and 120 nm, which falls into the single magnetic domain for magnetite and greigite [37]. Single magnetosomes are thus the most efficient conditions in terms of maximization of the particle remanent magnetization: particles with a size smaller than 20-30 nm are superparamagnetic (SP). One the other hand, particles larger than 120 nm are multidomain (MD), meaning that they are constituted by different magnetic domains oriented in different directions and this results in reduced remanent magnetization of the particle [38]. Magnetite crystals, produced in abiotic reactions, have so far led to magnetite crystals with lower crystallinity [39]. Therefore, magnetosomes represent a model for the synthesis of size and morphology-controlled magnetic nanoparticles.

In turn, the magnetosome chain is also a paradigm of a 1D magnetic nanostructure. Such nanostructures are intrinsically unstable as magnetic interactions and the minimization of the energy rather result in closed rings than in long chains [34, 35]. Recent studies have shown that the alignment of the magnetosomes along the axis indeed depends on additional biological determinants: the actin – like cytoskeleton MamK and the MamJ protein that comprises a link between the filament and the magnetosomes. This has a crucial function in the establishment of the magnetosome assembly into a chain [42]. MamK is homolog of the eukaryotic and prokaryotic actins and for its unique function and sufficient distance sequence homology represents its own family [43]. Mutants of MamK in the *Magnetospirillum magneticum* AMB-1 and the *Magnetospirillum gryphiswaldense* MSR-1 strain showed that the absence of the magnetosome chain, leading to the formation of groups of 2 – 3 magnetosomes dispersed in the cell, suggesting that MamK is the main organizer of the magnetosome alignment inside the cell [38, 39]. Finally, it has been shown *in silico* that the biological determinants are the critical players in the process [46].

Process of biomineralization

Beside the development of new technologies, the process of biomineralization in MTB is subject of intense studies. It can represent a simple path for a better understanding of a wide range of mineralization processes taking place in different organisms. The biomineralization process for greigite-producing MTB is still not as well explored as for magnetite producers; therefore, this paragraph will discuss the process for magnetite-producing bacteria, in particular on the *Magnetospirillum* genus. Magnetospirillum became widely used in research due to the facility in cultivating them in axenic conditions.

Magnetospirillum are able to take up both Fe (II) and Fe (III) [36, 37, 38, 45]. Even though the iron uptake in MTB is several orders of magnitude higher compared to other bacteria, no exclusive iron uptake system was so far reported [10, 31]. Studies show that in *M. magneticum* strain AMB-1, iron is stored within the cell in a phosphate-rich ferric hydroxide phase (ferritin) [51]. In parallel, the magnetosome membrane is generated by invagination of the cytoplasmic membrane. The magnetosome membrane remains attached to the cytoplasmic membrane also once the magnetosome is fully formed [44]. The magnetic nanocrystals nucleate and grow within the magnetosome membrane invagination. Many proteins are thus involved for transport inside the vesicle. During transportation, Fe and P

become separated and ferrihydrite is formed ($Fe_2O_3 \cdot n \cdot H_2O$) [51]. It was speculated that the nucleation takes place in contact with the membrane [22]. The ferrihydrite is reduced to magnetite, and the crystal grows within the membrane with a strict cellular control [51].

Most of the genes that regulate the process of magnetosome formation are located in a genomic region called magnetosome island (MAI), highly conserved among almost all the MTB species [52]. It was demonstrated that the deletion of the MAI leads to the loss of magnetosome formation. This also happens in the case of a partial deletion of particular sections of the MAI called operons [52].

Environmental influences on the magnetosome formation

Although bacteria can recreate a synthetic environment for the magnetosome formation process, many studies have found that differences in the chemical and physical conditions of cell cultures can have a significant impact on the cell physiology and the bacteria crystal morphology. Such an effect can indeed be expected since intermediates are found in the process of magnetite formation. As such, changing the physic-chemical environment might directly impact the formation pathway as some intermediates formation might be altered or alternatively kinetically favored. As an example, *Magnetospirillum* were shown to be able to take up both Fe (II) and Fe (III) [43, 44, [49], [50]. If the conditions in the medium are rather reduced or oxidized, either an active or a passive iron uptake might be going on [53] [54], and thereby the whole chain of biomineralization is influenced and potentially changed.

The chemical composition of the growing medium, besides providing the nutrients needed for the cell's vital metabolism, also therefore directly influences the biomineralization process.; For example, Faivre et al. showed that the crystal morphology is directly connected to iron uptake rates in MSR-1 cells and thus to the iron availability in the medium [55]. When the uptake rate is high, the biological control is suggested to be less efficient, explaining why the magnetosomes exhibited irregular morphologies in these conditions.

The impact of extracellular pH was also investigated on *Magnetospirillum gryphiswaldense* MSR-1 strain [39]. Moisescu et al. suggested that the ability of MSR-1 to control the biomineralization process was altered when the pH was shifted away from the optimum (pH 7) between pH 5.0 and 9.0. As the consequence, the size of synthesized magnetosomes and crystal morphologies were dramatically changed, exhibiting pyramidal shapes. Results

presented by Moisescu et al. revealed that at ambient conditions, when the pH of the growth medium was changed, the rates of Fe uptake at all pH values (except at pH 5.0) were still high.

Another parameter affecting magnetosome formation is the oxygen concentrations. Blakemore tested the effect of oxygen on the growth and production of magnetosomes in *M. magnetotacticum* MS-1 revealing that the nanoparticle formation can happen only in microaerobic conditions [27]. Similar studies were conducted on *M. magneticum* AMB-1 [56] and on *M. gryphiswaldense* [54]. Generally, magnetosomes are produced under a threshold of oxygen concentration; above which the production is inhibited. Heyen & Schüler used a fermenter and reported a threshold limit for the magnetosome production of 20 mbar of oxygen pressure for strains belonging to *Magnetospirillum* genus [57]. Popa et al. (2009) attributed this inhibition to oxidative stress [58]. As shown in Figure 2.3, iron ions in water have different oxidation states at various ORP values, while magnetite occurs at specific redox and pH conditions. Following this scheme, standard physiological conditions do not allow magnetite formation. Magnetotactic bacteria therefore have a system to strictly control the internal redox conditions in order to produce the correct ratio of mixed valence Fe(II)-Fe(III) necessary for magnetite synthesis. The intracellular compartments within the magnetosome membrane is an ideal place for the synthesis of the magnetite under conditions far from physiological ones without endangering other cellular processes.

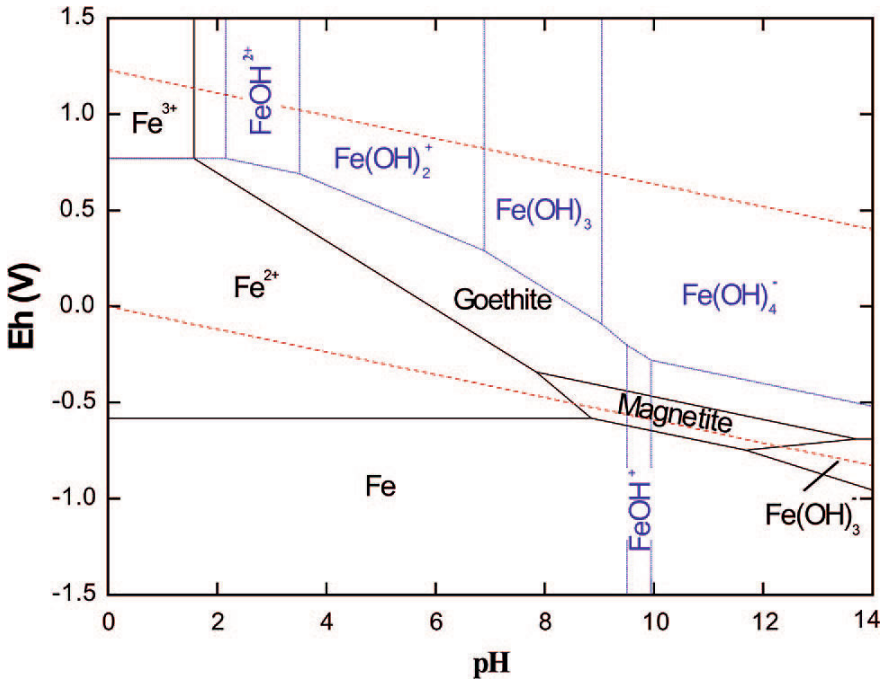

Figure 2.3 Pourbaix (ORP-pH) diagram of iron in water system. Figure adapted with permission from Faivre & Schüler (2008).

To sum up, magnetite formation in *Magnetospirillum* ssp. requires microaerobic or anaerobic conditions [57]. This agrees with the chemical conditions reported in the above figure (Figure 2.3) for abiotic synthesis conditions, which require low or no oxygen in order to prevent oxidation of ferrous to ferric iron. However, if magnetite forms under slightly reducing conditions (E_h ~ - 0.2 to – 0.4 V) and alkaline pH (> 8) [22], only the indirect effect of the oxygen concentration on magnetosome formation has been studied. The effect of the ORP has not been reported.

Many studies have been conducted for on the role of ORP and the impact of oxidizers and reducers on growth and on the production of fermentation products from microorganisms [46, 47], providing an insight on how efficient regulation of ORP could direct energetic and metabolic pathways through a higher production of desirable products [60]. Magnetotactic bacteria belong to the group of microorganisms that require particular redox conditions for living. A narrow band in water bodies, where oxygen concentration rapidly decreases until completely disappearing, so called OATZ comprises the environment for bacteria to live [61]. This particular environment is represented by a rapid decrease of ORP potential, passing from an oxidizing condition in aerobic environments to reducing conditions in the anoxic zone below OATZ. In natural environments, MTB are mainly found in reducing conditions, between values of 0 –400 mV [62] such that the influence of the ORP on magnetosome formation will be studied here.

Magnetospirillum species

Magnetospirillum magneticum AMB-1 strain was firstly isolated from sediments of a pond in Tokyo, Japan [63]. A particularity of this strain is the ability to grow in different conditions: aerobically, microaerobically and in anoxic conditions. [64].

M. magneticum AMB-1 are helically shaped bacteria, with a usual length of 3-4 microns and a single flagellum at both poles. They can exhibit different morphologies at different growth phases, i.e. they can either elongate when kept in stress conditions or turn into round cocci when close to death [65]. They produce magnetosomes with an octahedral shape [22] and an average diameter of 50 nm [63].

Magnetospirillum gryphiswaldense MSR-1 strain is used as another model organism in biomineralization studies. *M. gryphiswaldense* was isolated from the river Ryck near

Greifswald, in Germany. This helical bacterium, possessing monotrichous flagellum on both poles, is highly motile [66]. This α-proteobacterium is one of the most studied strain, especially in terms of the biochemistry of proteins involved in the formation of magnetosomes [52].

All *Magnetospirillum* species grow chemoorganoheterotrophically and use organic acids as sources of electrons and carbon. They do not use sugars neither for respiration nor for fermentation. In fact, fermentation has not been found to occur in any *Magnetospirillum* species. Oxygen and nitrate are utilized as terminal electron acceptors and they can be considered denitrifying bacteria, able to reduce nitrate to nitrous oxide (N_2O) and N_2 [67].

2.1.1. Experimental

This section describes all of the bacterial strains used during performed experiments, the preliminary tests on precultures, such as aging of the preculture and toxicity of chemicals used to control ORP in the bioreactor, and their influence on bacterial growth. Furthermore it introduces control experiments by using mutant strain. Samples preparation and investigation are also described.

Bacterial strains used in this work

For the purpose of the work presented in this manuscript, the strain *Magnetospirillum magneticum* AMB-1 was used. It was purchased from the American Collection of Cell Cultures (No. 700264). For the control experiment *Magnetospirillum magneticum* AMB-1 mutant was used; *ΔmamAB* was kindly provided by the group of Prof. A. Komeili (University of Berkeley, Department of Plant & Microbial Biology).

Growth conditions in flasks

Bacteria were grown in modified flask standard medium (FSM) containing (per liter deionized water) 0.1 g KH_2PO_4 (Acros organics, Belgium), 0.15 g $MgSO_4 \times 7\ H_2O$, 2.38 g Hepes,

0.34 g $NaNO_3$ (Sigma Aldrich, USA), 0.1 g yeast extract, 3 g soya peptone, and 100 µM iron (III) citrate (Alfa Aesar, Germany) [57]. If not specified otherwise, all chemicals were purchased from Carl Roth (Karlsruhe, Germany). The medium contained 27 mM sodium pyruvate (Alfa Aesar, Germany) as carbon source, modified trace elements, and iron depleted, prepared according to [68]. Inoculation was done with 10 % (v/v) subculture and incubated under gentle shaking (100 rpm) at 28 °C for 24-48 hours.

Three different cultivation conditions were used along all the experiments: aerobic, microaerobic and anaerobic. The media was bubbled for 15 minutes with N_2 in order to provide anaerobic conditions. The mixture of 99% N_2 and 1 % O_2 was used to generate microaerobic conditions, whereas for aerobic conditions no bubbling was needed. Afterwards, the flasks were sealed with open ended caps and rubber stoppers and autoclaved. A UV/VIS-spectrophotometer (Nanophotometer, IMPLEN, Germany) was used to determine the cell growth by measuring the optical density (OD) at 565 nm (OD_{565}). The optical density was measured with two bar magnets (Supermagnete, Germany) placed parallel (OD_{min}) and perpendicular to the light beam (OD_{max}). The coefficient of magnetically induced differential light scattering (C_{mag}), describing the magnetic orientation of the cells was calculated using following equation [69]:

$$Cmag = \frac{ODmax}{ODmin} - 1 \qquad \textbf{eq 2.1}$$

In order to correlate OD values with amount of cells, cell counting experiment was performed through growing cells in 100 mL modified FSM, under microaerobic conditions. 10 mL of a fully grown subculture was transferred into fresh culture media. OD_{565} was measured after 40 hours of growth and the cells were counted using a Neubauer improved counting chamber (Brand, Germany) and optical microscope (AXIO-microscope, Zeiss, Germany).

Non-magnetic culture preparation

From a fully grown microaerobic FSM iron-rich culture, 3 % (v/v) was inoculated into 100 mL of fresh iron–depleted culture medium, prepared under aerobic conditions. After 72 h, the entire culture was used as a second preculture for 2 L flasks containing 1 L iron-depleted fresh medium, prepared under aerobic conditions. The final, third, 1 L subculture was used for

the experiments performed in the bioreactor. A schematic showing inoculation steps is presented in Figure 2.4.

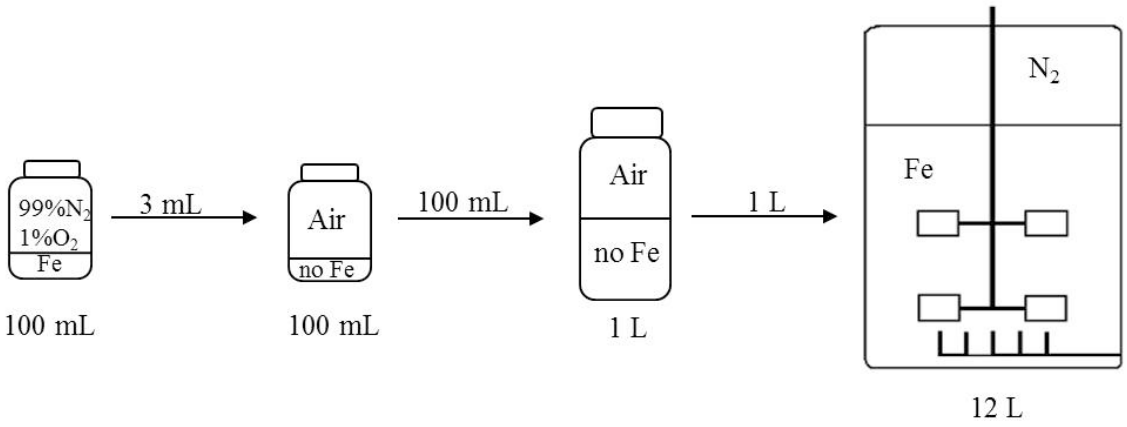

Figure 2.4 Schematic showing steps of inoculum preparation and final inoculation into the bioreactor. From a fully grown magnetic preculture, 3 mL was transferred into 100 mL of fresh culture iron-depleted medium. The entire second subculture was then transferred into 1 L of iron-depleted medium. As the final inoculation step, 1 L subculture was transferred into 12 L of medium containing 100 µM iron (III) citrate.

Ageing of the preculture

The influence of redox potential during AMB-1 growth required performing preliminary tests such as aging of the preculture and toxicity tests: showing the influence of the chemicals on bacterial behavior. The experiment was done in order to understand whether 'older' precultures have an effect on AMB-1 growth rates. A preculture was prepared in 500 mL flask filled with 250 mL of iron depleted FSM medium, sealed under aerobic conditions. Bacteria were inoculated by injection through the stopper. The preculture was incubated for 24 hours, under shaking conditions (100 rpm). After that time 10 mL of the preculture was injected into the new flask and further cultivated. The initial preculture was continuously cultivated and a second inoculum was prepared after 48 hours and a third one and final one, after 72 hours. OD_{565} of new subcultures was measured immediately after the inoculation, and after 4, 20 and 24 hours respectively.

Toxicity test of chemicals used for ORP control

The experiments were performed in 100 mL flasks filled with 70 mL FSM medium containing different concentrations of $K_3[Fe(CN)_6]$. $K_3[Fe(CN)_6]$ was added to the final concentration

of 0.1; 0.3; 0.7; 1.5; 3.6 mM. The reactant is used as chemical to impose a higher ORP within the fermenter. Before autoclaving, the flasks were bubbled with nitrogen in order to mimic further experiments in the bioreactor. 10 mL of fully grown subculture was transferred to previously prepared flasks and OD_{565} of the bacteria was measured immediately after the inoculation and after 4, 20, and 24 hours respectively. The essay was repeated 3 times.

A similar procedure was repeated with titanium (III) citrate. The reactant is used as chemical to impose a smaller (reduced) ORP within the fermenter. In order to test the toxicity of titanium (III) citrate, the preculture was prepared in the same manner as during toxicity test performed with potassium ferricyanide and transferred to 500 mL flask containing 300 mL FSM, bubbled with nitrogen. In this case, the flasks were supplemented, before inoculation, with different volumes of titanium (III) citrate in order to obtain the following concentrations in the final volume: 0.22; 0.45; 0.9; 1.9; 3.8; 7.5; and 15 mM. OD_{565} was measured immediately after the inoculation and after 4, 20 and 24 hours. The essay was repeated 3 times.

Culture growth in the bioreactor

Bacteria were grown in a bioreactor with a volume of 16 liters (L1523, Bioengineering, Switzerland). The bioreactor was filled with 12 L of FSM medium, omitting Hepes; sodium pyruvate was substituted by aqueous solution of 0.3 % (v/v) of L-(+)-lactic acid (Sigma Aldrich, USA).The experiments with the AMB-1 strain at various ORP tensions were performed in the fermentor equipped for the automatic control of temperature, dissolved oxygen concentration, pH and ORP. The pH of the culture was controlled by the addition of either 1 M NaOH or 0.5 M H_2SO_4. The ORP control was obtained by the addition of either 0.8 M of titanium (III) citrate or 0.3 % (w/v) potassium ferricyanide solution. The oxygen concentration was continuously measured using an oxygen probe (Bioengineering, Switzerland). After sterilization of the filled reservoir (121°C for 35 min), the syringe providing nitrogen source was plugged in, during the cooling process, to sparge nitrogen through the medium and obtain oxygen-free conditions. After the desired temperature was reached, the pH and the ORP values were adjusted. As such, the bioreactor was prepared to inoculate bacteria and perform experiments.

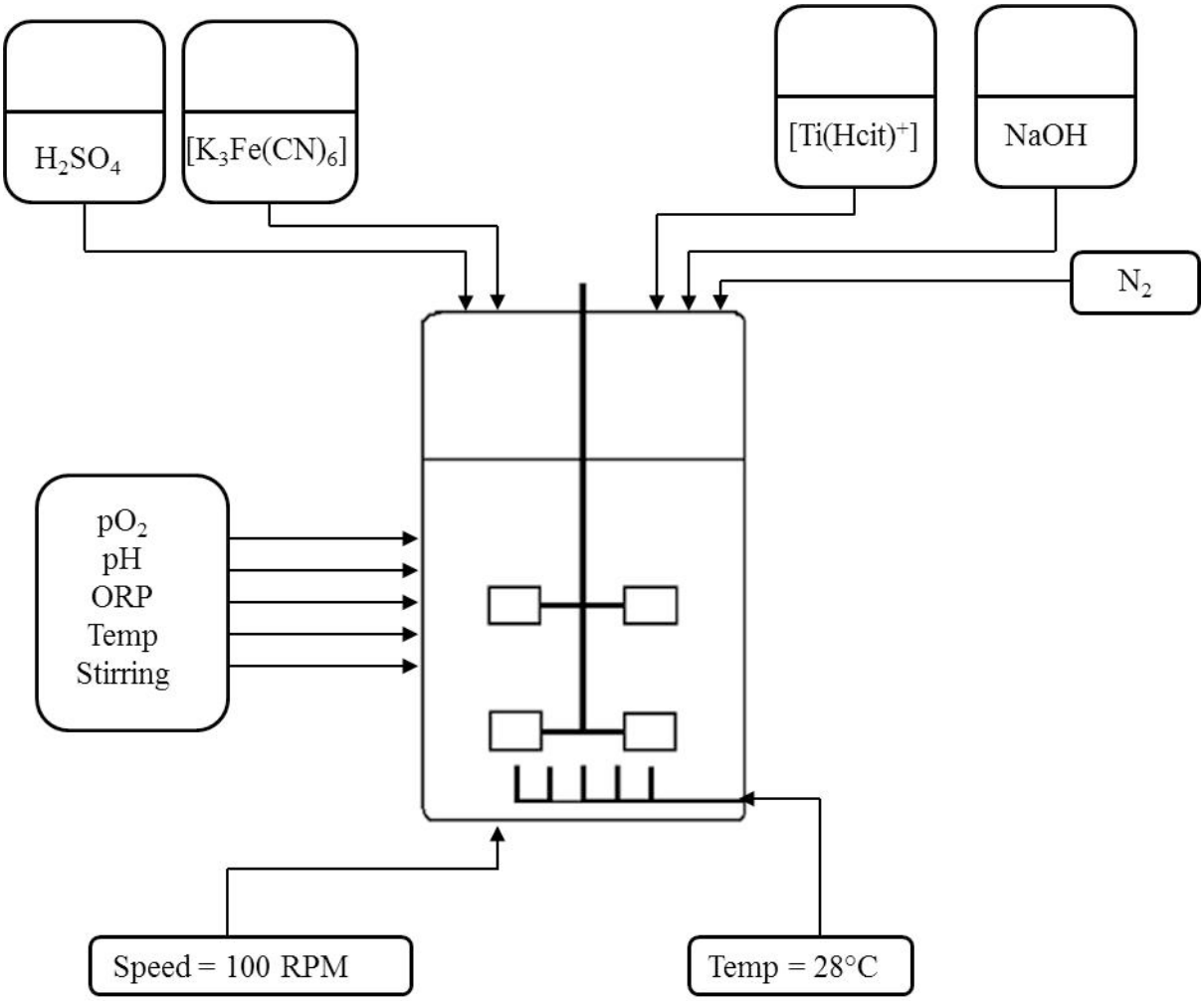

Figure 2.5 Schematic of the bioreactor utilized. pH and ORP were regulated through feedback systems. H_2SO_4 and NaOH were used for pH control, and titanium (III) citrate and potassium ferricyanide for ORP control. The temperature was kept constant during the entire experiment. Oxygen level, pH, ORP, and temperature were constantly monitored and corrected.

The experiments were carried for 42 hours. During the cultivation, the temperature was set to 28°C, and stirring speed to 100 rpm. Both redox potential and pH were regulated with feedback systems. pH was set to 7 with the threshold set at ± 0.2, and ORP was set to either to 0 or -500 mV respectively, with the threshold ± 0.3 mV. The fermentation without ORP adjustment was performed in order to investigate what are the ORP values when the bacteria are grown at pH 7 without ORP control. A blank fermentation without cells and without regulating ORP and pH was done in order to observe the behavior of ORP in the culture medium.

2.2. Bacteriophages

Filamentous phages correspond to the genus Inovirus and belong to the family Inoviridae. [70]. Inovirus (filamentous bacteriophage) contains circular single-stranded DNA arranged in a double-stranded helix [71]. Gram-negative bacteria are predominant hosts of filamentous phages. Ff bacteriophages infect *Escherichia coli* cells carrying the F factor plasmid and therefore displaying F pili on their surface [72]. Bacteriophages f1, M13, or fd are 98 % identical at the DNA sequence level and have been used interchangeable in different studies [71][73].

M13 is a specific bacteriophage; composed of a single-stranded DNA encapsulated with major (p8) and minor (p3, p6, p7, and p 9) coat proteins (see Figure 2.6). Two minor coat proteins p3 and p6 cap one end and two other minor coat proteins p7 and p9 encapsulate the other end. Each minor coat protein is present at about 5 copies per phage. The major coat protein consists of 2700 copies and comprises 98 % of the whole mass of the virus. All of the five proteins are necessary for structural stability. M13 phage is approximately 800 nm in length and 6 nm in width. The p3 is the largest of all coating proteins; it contains 406 amino acids and and 42 kDa in molecular weight [74]. The major coat protein, containing 112 amino acids and around 12 kDa in molecular weight, is arranged in five-fold rotational axis in a α-helical structure [74]. The n-terminal of p8 protein is negatively charged due to acidic amino acids which give the phage and overall negative charge.

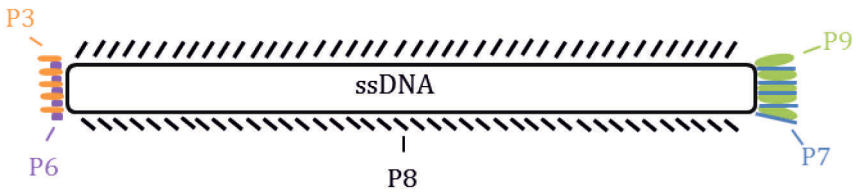

Figure 2.6 Scheme illustrating various coat proteins of the M13 filamentous bacteriophage.

The replication process starts by the p3 end of the phage binding to the F pilus of the *E.coli* cell and inserting the DNA inside the bacterial cell. The various coat proteins are assembled inside the host cell and the assembly is initiated by the incorporation pf p7 and p9 at one end of the virus. Copies of p8 are then assembled along the phage. The termination of the

assembly occurs by the addition of p3 and p6 at the other end of the phage particle. The assembled bacteriophage is then released into the environment. The freshly assembled phages extrude continuously from the infected cells. The whole process is non-lytic, therefore the infected cells continue to grow and replicate though at a reduced rate.

Functionalization of nanoparticles and M13 phage

Original applications of Ff (M13, f1 and fd) bacteriophages were dedicated molecular biology techniques. Phages were used as cloning vectors for sequencing and *in vitro* oligonucleotide-directed mutagenesis [71]. Besides direct use Ff phages as cloning vectors, plasmids, called phagemids, have been in wide use [75]. The most technological contribution that was so far of a great importance is phage display, but most recent applications of phage display technology cross into nanotechnology[76]. All virion proteins have been used as a platform for display, but most commonly minor p3 and major p8 protein. Moreover, examples of display of two or more proteins have been reported [77]. The group of A. Belcher has isolated peptides that can nucleate nanocrystal assembly of a number of inorganics, such as paramagnetic (FePt, CoPt) [78] or semiconductor materials [13]. The fibrous nature of phages have been utilized for production on phage-templated nanomaterials for applications in microelectronics [79], as biosensors [14], as well as tissue engineering [80].

The first part of this study describes how phage filaments were used in order to provide a scaffold for magnetic nanoparticle assembly. The electrostatic interactions between magnetite nanoparticles and p8 protein of the phage (see Figure 2.6) were studied in order to deposit nanoparticles on the filaments. In order to determine the surface charge of utilized molecules, zeta potential measurements were performed on phages and three kinds of magnetic nanoparticles: magnetosomes isolated from magnetotactic bacterium *M.magneticum* AMB-1 strain, magnetite nanoparticles formed in the presence of poly-L-arginine [81] and magnetite nanoparticles coated with polyethylene imine [82].

The second part of the project was dedicated to designing flagellum - like construct based on the head – magnetic nanoparticle and tail composed of a phage filament. The head was constructed from MamC- RBP magnetosome. MamC-RBP magnetosomes were isolated from magnetotactic bacterium - *M. gryphiswaldense* strain MSR-1. The immobilization of a red fluorescent protein - binding naobody (RBP) on magnetosomes, by fusion of the RBP to the magnetosome membrane (MM) protein MamC, resulted in the expressing of MamC-RBP

[83]. MamC-RBP can recognize their antigen, the mCherry protein. In order to enable stable binding between phage filaments and MamC-RBP magnetosomes, mCherry protein was directly fused to a g3p, p3 protein of M13 phage [84]. Phage particles were then purified, which is described in section 2.2.1.

Actuation of magnetic phages in external magnetic fields

Both of the assemblies, chain of nanoparticles attached along the phage filament and flagellum like phage with Mam-C RBP magnetosome attached could be activated in the magnetic fields. An external magnetic field can produce a torque on a magnetic nanostructure, in this study made from magnetite. The magnetic properties of magnetite nanocrystals are largely controlled by their domain states, by increasing size, are superparamagnetic (SP), single domain (SD), and multidomain (MD) [22]. Crystals with lengths less than 100 nm belong to the SD particle group, particles smaller than 35 nm are SP. Crystals larger exhibit several uniformly magnetized domains. Within multi-domain magnets the domains exhibit magnetic dipoles with different orientation lowering the total dipole of the particles [85]. The nanostructures used in this study can be named as being in a multi-domain state, because they consist of several particles which might be in the stable single domain (SSD) or the MD states.

Several mechanisms for magnetic actuation have been suggested [86] [87]. For example, gradient fields have been used successfully to move microscopic objects [88] [89]. Magnetic propellers are chiral magnetic structures, which are actuated by rotating magnetic fields [90]. Swimmers are objects that change shape during one period of the actuating field, in a way that leads to a net displacement of the structure [91]. One way to actuate a structure is a non-reciprocal way, for example by applying a rotating magnetic field [90].

The micropropeller smaller than 100 μm, was firstly created by Zhang et al. using self-scrolling thin films [92]. Ghosh and Fisher fabricated propellers smaller than Zhang (0.25 × 1.5 μm) [93]. Dreyfus reported a swimmer, built from a chain of superparamagnetic beads linked by DNA attached on one end to a red blood cell [91]. Gao et al. designed a swimmer, by connecting a magnetic nickel nanorod to a gold nanorod via a thin silver filament [94]. Pak et al. constructed with similar design nickel nanorod with a silver tail [95].

Constructing micro and nanopropellers is a great interest due to their high potential for applications; such as noninvasive medicine [2] [96] as well as environmental remediation [97]. Rotating magnetic particles could be used to trap and transport microorganisms [98]. Molecular imaging allows visualization the progression of tumors. The optical, electrical and magnetic properties of nanoparticles make them promising tool for patient diagnosis. Nanoparticles templated on M13 – phage such as shown in Figure 2.7 could be used as well for *in vivo* cell imaging [99].

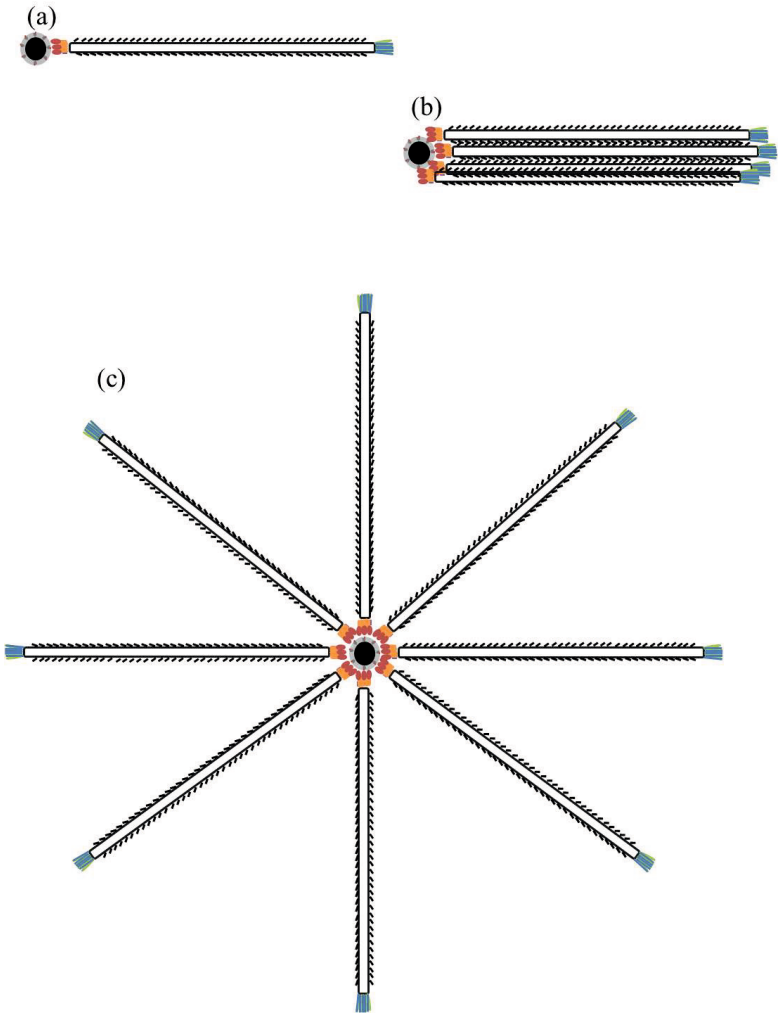

Figure 2.7 A schematic presentation of the M13 phage displaying mCherry protein and MamC-RBP magnetosome. Three variants of possible assemblies are shown: (a) phage and magnetosomes form flagellum like structure; (b) Phages and magnetosomes form multi-flagellum construct; (c) Phages surround the magnetosome forming star – shape assembly.

Important characteristic of the chains made of magnetic particles is their ability to change conformation when an external magnetic field is applied or changes direction. To this end, the flexibility of the magnetic chains was studied both theoretically and experimentally [100] [101] [102]. Goubault at al. reported that long flexible filaments, made of superparamagnetic submicron particles linked by polymer chains, can adopt under magnetic field in hairpin configuration [7].

2.2.1. Experimental

Bacteriophage amplification

In order to purify both WT phage filaments and phages displaying mCherry protein, the work was divided to two parts: WT bacteriophage amplification and mCherry phage amplification. The sources of bacterial and viral strains presented in this manuscript are shown in the table below (Table 2-1).

Table 2-1 Overview of strains and mutants used for work presented in this manuscript

Name of the strain	Provided by/Purchased from	Reference
E.coli K12 ER2738	NEW ENGLAND BioLabs Inc.	[103]
M13 KE Phage	NEW ENGLAND BioLabs Inc.	[104]
E.coli XL1 - Blue	K.Arndt group	[84]
Tor A M13 mutant	K.Arndt group	[84]
VCSM13 Helper Phage	Agilent Technologies	[105]

WT Phage amplification

M13KE phage was purchased from New England Biolabs (Ipwich, Massachusetts, USA). Phages were grown and purified, following standard biochemical protocols [106]. *E.coli* K12 ER2738 cells were used for phage amplification. 20 mL of LB medium was inoculated with 200µL overnight *E.Coli* culture and 1 µL phage suspension. The ER2738 cells were incubated at 37°C with vigorous shaking (250rpm) for 4 hours and 30 min. After cells removal by two

centrifugations (4500 x g, 10 min, and 4°C) top 16mL supernatant was transferred to a new tube and mixed with 2.5M NaCl/20% PEG-8000 (w/v) solution to concentrate phage solution. After overnight precipitation at 4°C, phage pellet was collected by centrifugation at 12 000 g, 15 min and suspended in 1 mL Tris-buffered saline (TBS) (25 mM Tris/HCl, 150 mM NaCl, pH 7.5). After second precipitation step with 2.5 M NaCl/20% PEG-8000 (w/v) solution, final phage pellet was collected and suspended in 100µL milli-Q water. Phage content was determined by absorption measurement according to [107]:

phage concentration (phages / ml) = $((A_{269} - A_{320}) * 6 * 10^{16})$/ (phage genome in nt) * dilution factor

where:

A_{269} – The absorbance, which reflects proteins and DNA content in the solution at the wavelength $\lambda = 269$ nm

A_{320} – The absorbance, which corrects for the naturally high baseline value of the solution, measured at the wavelength $\lambda = 320$ nm

$6 * 10^{16}$ – the molar extinction coefficient of the phage and the average size of DNA base were collected into the constant

Larger phage yield was necessary in order to perform zeta potentials measurements. Therefore standard amplification protocol, described above, was scaled up to the final volume phage suspension of 1 mL.

mCherry phage amplification

The phage production protocol was kindly provided by Prof Katja Arndt's group. Five milliliters of 2xYT medium containing 25 µg/ml chloramphenicol, 20 µg / ml tetracycline and 1% glucose (2xYT/Cm/Tet/Glc) were inoculated with cells from a glycerol stock of E.coli XL1-Blue containing the respective phagemid. Cells were grown overnight at 37 °C on an orbital shaker (rpm). Sixty milliliters of 2xYT/Cm/Tet were inoculated with the pre-culture to an OD_{600} of 0.07 and grown at 37 °C with shaking. Cultures were infected with 10^{11} particles of helper phage VCS M13 at an OD_{600} of 0.3–0.4. After 15 min incubation without agitation, expression of the g3p-fusion protein was induced with 0.8 mM isopropyl b-

hiogalactopyranoside (IPTG) and shaking was continued at 28 °C (if not stated otherwise). After 1 h, kanamycin was added to a final concentration of 70 µg / ml. After 5 h, bacterial cells were removed by two successive centrifugation steps (5000 x g, 15 min, 4 °C) and the upper 80% of the supernatant were taken and mixed with one-sixth volume of polyethylene glycol (PEG) /NaCl solution (20% PEG 8000, 2.5 M NaCl). After overnight incubation on ice, the sample was centrifuged (5000 x g, 45 min, 4 °C) and the pellet was dissolved in 1 ml Tris-buffered saline (TBS) (25 mM Tris/HCl, 150 mM NaCl, pH 7.5). Impurities were removed by centrifugation (16 060 g, 10 min, and 4 °C) and phage particles were precipitated by mixing the supernatant with 200 ml PEG/NaCl solution and 1 h incubation on ice. Phage particles were again collected by centrifugation (16 060 g, 10min, 4 °C) and dissolved in TBS. After another centrifugation step (16 060 x g, 10min, 4C), the upper 90% of the supernatant were taken and the phage content was determined by absorption measurement according to [107].

2.3. Iron measurements

Inductively Coupled Plasma – Optical Emission Spectrometry (ICP-OES) is standard technique for the determination of trace elements in a myriad of sample types.

ICP-OES is employed for the quantification of elements in liquid or solid samples after acid digestion. The technique is based on the spontaneous emission of photons from atoms and ions that have been excited in a radio-frequency (RF) discharge. Liquid and gas samples can be injected directly into the instrument, whereas extraction and acid digestion is necessary for solid samples, so that the analytes will be present in the solution [108]. Samples are injected into an argon plasma, vaporized and energized due to collisional excitation at high temperature. The excited atoms emit photons and get ionized. These photons have characteristic energies that are determined by the quantized energy level structure for the atoms or ions. The emitted radiations are then measured by detectors. Therefore, it is possible to select specific wavelengths of analysis through the use of a grating device. The total number of photons is proportional to the concentration of the originating element in the sample [108].

2.3.1. Experimental

The data were collected with a commercially available spectrometer (Optima 8000, PerkinElmer Inc., USA). Samples containing bacterial pellets were dissolved in 500 µL aqua regia solution (65% w/v HNO_3 and 35 % w/v HCl, in a ratio 1:2 (v/v)). Samples were incubated overnight in glass vials at 40°C in order to dissolve all of the iron content. Due to the measurement requirements, the sample had to be diluted to the final volume of 5 mL.

Samples containing *M.*magneticum *ΔmamAB*, mutants of AMB-1 were utilized to determine how much iron is being adsorbed on the cell wall in order to distinguish between iron transported inside the cell and iron nucleating on its surface. Due to the fact that *ΔmamAB* AMB-1 mutant lacks of *mamAB* operon and therefore is not able to produce magnetosomes, this feature enables to estimate the actual iron amount that is being adsorbed on the cell surface. Iron content in pellets was measured in the same manner as in AMB-1.

2.4. Microscopy observations and image analysis

Electron microscopy enables to study object in the nanoscopic and even Ångström size range due to the use of electrons with very short wavelength. In this work, transmission electron microscopy (TEM) was used as a tool for the characterization of nanoparticle size and bacterial length. Moreover, this technique was necessary in order to visualize nan-sized bacteriophages. Virus samples were additionally stained with uranyl acetate, the substrate that possesses high density and improves the contrast due to absorption of electrons in the material. Additionally, high resolution transmission electron microscopy (HR-TEM) was used to determine the crystalline phase of nanoparticles.

2.4.1. Experimental

Transmission Electron Microscopy

20µL of bacterial solution were dropped onto parafilm and carbon coated TEM grid was placed on the top of the drop for 15 minutes. In the case of low cell density samples (OD_{565} < 0.200) centrifugation (5000 rpm, 5 min, and 4°C) was necessary in order to achieve sufficient concentration of the bacteria. After the incubation time, grids were dried with a paper and rinsed with washing buffer (10 mM Hepes, 5 mM EDTA) and the rest of the

solution was wicked off. Imaging was performed with a Zeiss 912 Omega at 120 kV acceleration voltage.

Imaging via high resolution transmission microscopy was performed with FEI Tecnai G2 F20 X-Twin at 200 kV acceleration voltage.

Properties of bacterial cells and magnetosomes

The TEM images were analyzed with the ImageJ program [109]. The size of magnetosomes and their number per cell were analyzed. Moreover the cell length was measured. Data were exported from ImageJ and analyzed with Excel and Origin, what is shown in the scheme in Figure 2.8 below.

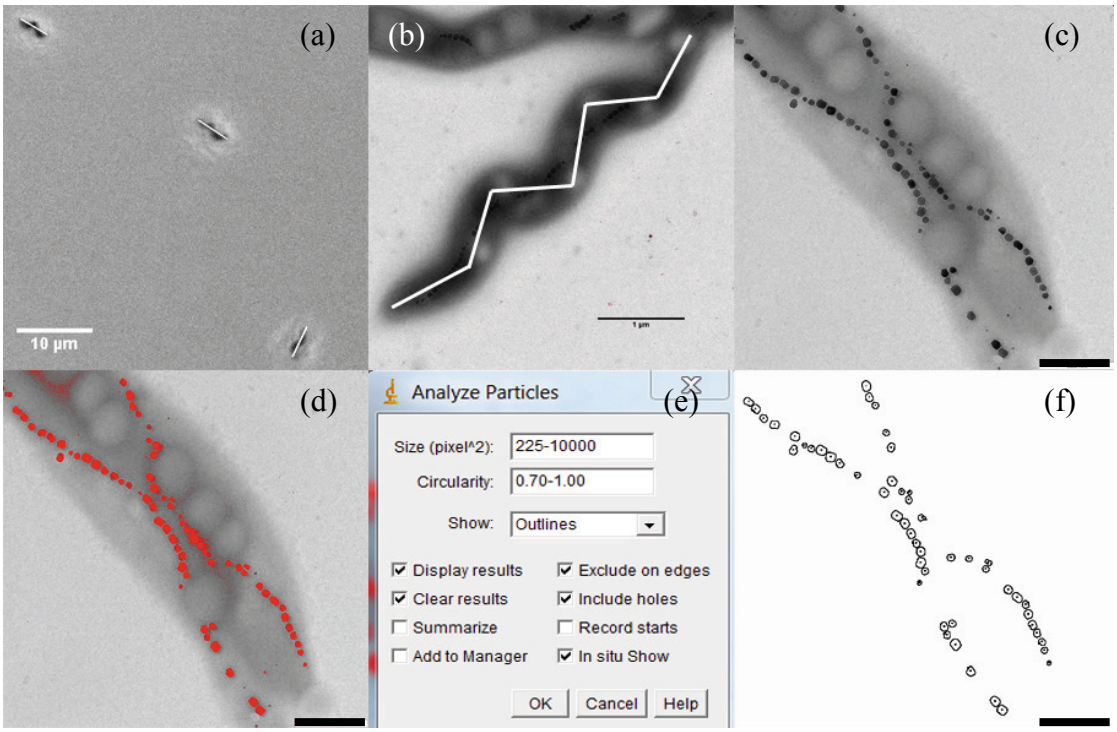

Figure 2.8 Size measurements. Panel "a" represents the method utilized for length measurements with the optical microscope. The length of the line drawn between the two poles of a bacterium was measured. Panel "b" (scale bar 1 µm) shows how the length of a bacterium was measured in TEM images. The length of the white line drawn in the middle of the bacterium was taken as the measurement. In panels "c, d, e, f" measurements of particles size using the software "imageJ" are shown: panel "c" represents one of the picture analyzed, in panel "d" the threshold was set, in panel "e" the settings for the measurements were inserted, while panel "f" shows the outlines of the particles selected for measurements (panel c, d, f, scale bar =500nm).

Phages – nanoparticles assembly

20 µL of the phage – nanoparticle mixture was adsorbed to carbon film Cu TEM grids for 10 min. Before TEM analysis, samples were stained with 2 % uranyl acetate solution. The excess staining solution was wicked off and the grid was dried on air.

The TEM images of phages-nanoparticles assembly were analyzed with Image J program. The number of nanoparticles attached to the phage filaments was counted. As shown in Figure 2.9, two lines were drawn along the phages-nanoparticles assembly, describing the longitudinal and lateral axis. The number of nanoparticles attached to the phage filaments was standardized per length of the filament [µm] as well as per surface area [μm^2]. Surface area was calculated by multiplying the longitudinal and the lateral axis, giving a surface area of a rectangle.

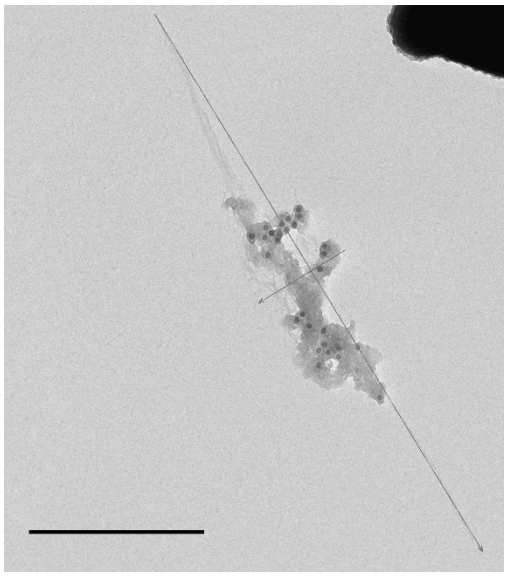

Figure 2.9 An example of transmission electron microscopy image of phages-nanoparticles assembly. The amount of nanoparticles attached to phage filaments was counted. Two lines describing longitudinal and lateral axis were drawn, indicated by this lines in the image. Lengths of both lines were used to calculate the surface area of phages-nanoparticles assembly. Scale bar is 1000 nm.

2.4.2. Energy dispersive X-ray Spectroscopy

The elemental composition of RBP magnetosomes was investigated using energy dispersive x-ray spectroscopy (EDX) in the TEM in collaboration with Victoria Reichel (Department of Biomaterials, MPIKG) and Dr. Richard Wirth (Deutsches Geoforschungs Zentrum, Potsdam).

2.5. X-Ray Diffraction

To complement the magnetosomes size evaluation by TEM, X-ray diffraction analyses were performed. X-ray measurements were taken at the μ-Spot beam line, BESSY II, Berlin [110]. Special custom made sample holder equipped with Kapton foil (Breitlander GmbH, Hamm, Germany, Cat. No. CH-440) was used [111].

2.5.1. Experimental

For each sample a volume of 5 μL non-diluted suspension was dried on the Kapton foil and measured in transmission with a 100 μm beam of the wavelength λ = 0.82656 nm. 2D - diffraction patterns were recorded with 3072 x 3072 pixel MarMosaic 225 CCD camera with 37.242 μm pixel size (Mar USA, Evanston, USA). Sample to detector distance was usually around 150 – 170 mm and exposure to the beam was 5 – 60 s per sample and measurement. Fit2D [112] and AutoFit [113] were used to calculate the exact sample-to-detector distance, the instrumental peak broadening and the full width at half maximum. All the three parameters were determined by fitting (311)-peak with a pseudo-Voigt function and the crystalline size was determined with the Scherrer equation [114] .

2.6. Dynamic Light Scattering

Light scattering has been used for a number of years to understand the structure and dynamics of the colloidal suspensions. Dynamic light scattering belongs to subcategory of techniques using scattered light and as the name suggests, is used to describe the dynamic properties of the sample. Dynamic Light Scattering (DLS) is a method to characterize the size of molecules in solution [115]. DLS detects the temporal fluctuation of the intensity of the backscattered radiation due to the Brownian motion effect in order to obtain the dynamic information of different length scales [115]. Smaller particles move faster than the larger once and their speed is determined by the Brownian motion. As the colloidal particles move, the pattern created by the scattered light is fluctuating in time and space. These fluctuations can be monitored by a photon correlator and a time-dependent intensity correlation function is obtained[115]:

$$d(H) = \frac{kT}{3\pi\eta D} \qquad \textbf{eq 2.2}$$

where:

d(H)=hydrodynamic diameter, D = diffusion coefficient, k = Boltzmann's constant, T = temperature, and η = viscosity of the solvent.

D can be determined from the equation of the time constant:

$$time\ constant = \frac{16\pi^2 n^2}{\lambda^2} sin^2 \frac{\theta}{2} D \qquad \textbf{eq 2.3}$$

where:

λ = laser wavelength (532 nm), n = refractive index of the solvent, θ = scattering angle (173°).

Zeta Potential

Zeta Potential is a physical property of any particle that describes its electrokinetic potential in colloidal dispersions. A charged particle in a suspension would affect the distribution of ions in the surrounding interfacial region. It results in the increased concentration of counterions close to the surface and thus double layer around each particle starts to be formed [115].

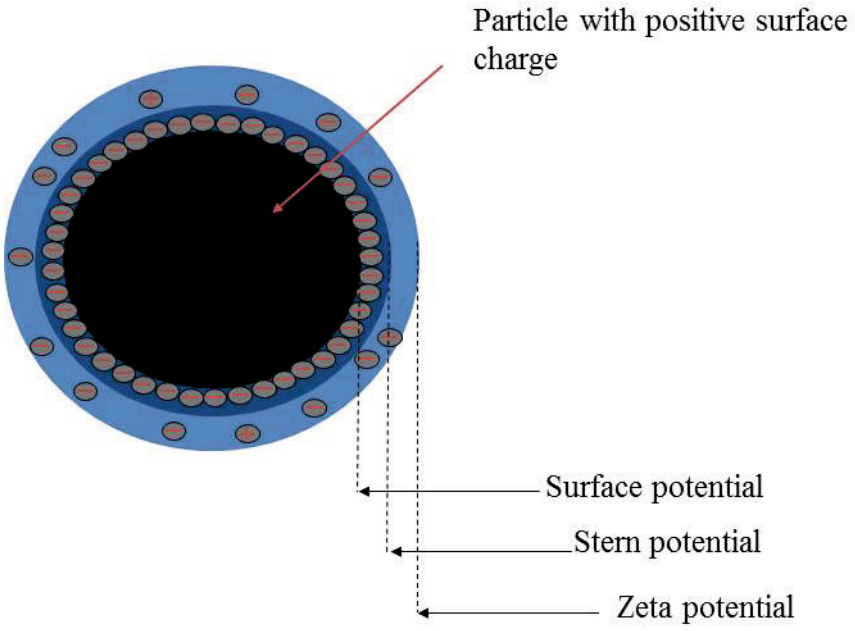

Figure 2.10 Schematic representation of the double layer and distribution of positive and negative ions around the molecule.

The liquid layer surrounding the molecule exist as two parts (see Figure 2.10); so called Stern layer, where the ions are strongly bound, and the outer region, where the attachment is not as strong as in the inner area. Within the diffuse layer there is a boundary inside which the ions and molecules form a stable entity. The potential that exist at this boundary is known as the Zeta potential. If the molecules have a large negative or positive zeta potential, then they will tend to repel each other without resulting in flocculating. However, when the zeta potentials are low, particles will start coming together and flocculating. Generally suspensions are considered stable when particles have zeta potentials more positive than +30 mV or more negative than – 30 mV [116]. One of the most important factors that affect zeta potentials is pH.

2.6.1. Experimental

Dynamic Light Scattering of M13 phage, PEI NPs and a mixture of both phage and nanoparticles was analyzed with a Zetasizer ZEN ZS 3500 (Malvern Instruments). The measurements were done by setting a Standard Operating Procedure (SOP), which enables the use of pre-defined parameters (i.e. viscosity, temperature, refractive index of the molecule and the dispersant) and ensures the reproducibility of further measurements on different samples Samples were measured for their hydrodynamic diameter and zeta potential. The suspension of M13, PEI NPs and mixture of both was poured into a clean cuvette designed for Zeta Potential Measurements. 1mL the solution was applied for each run. Three runs were performed at 25°C and each run was measured 20 times and averaged.

The setup of the ZetaSizer Nano (Malvern Instruments) used for DLS measurements consists of: a laser source in order to illuminate the sample in the sample cell and an attenuator that keeps the intensity of the scattered light within the desired range. By decreasing or increasing the intensity of the laser, it allows more or less light to pass through the sample depending on the sample's concentration. A detector is necessary to measure the intensity of the scattered light, which is then passed to a digital signal processing board. The information is transferred to a computer where the software Nano analyzes the data. The scheme of the setup is shown in Figure 2.11.

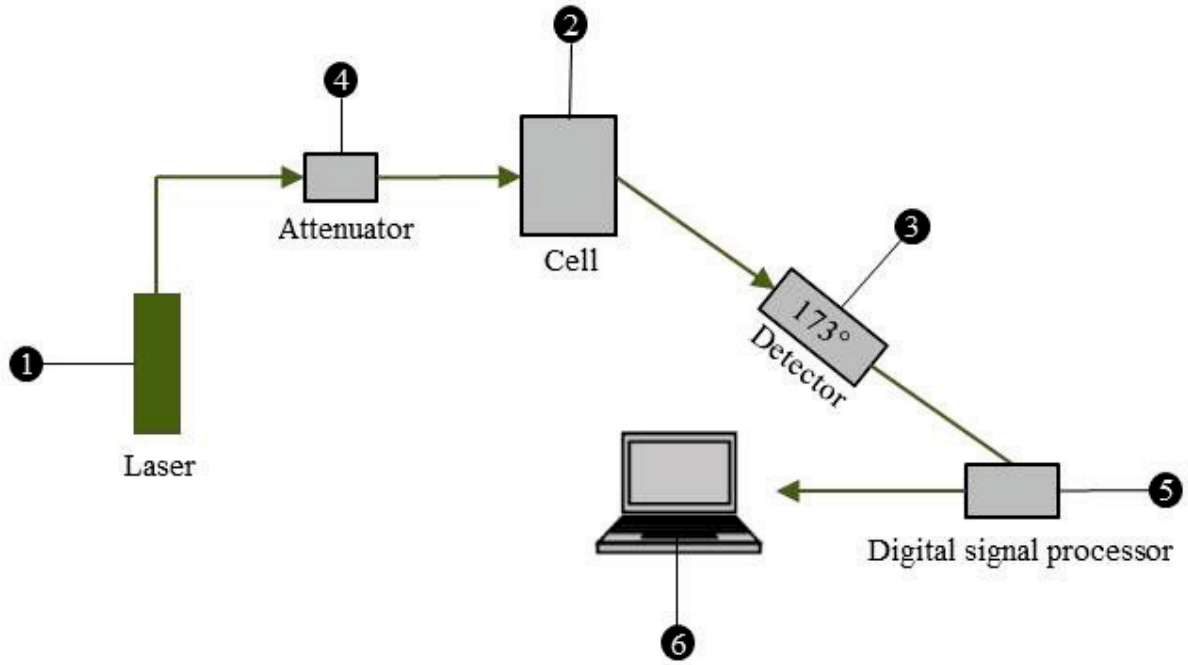

Figure 2.11Configuration setup for Dynamic Light Scattering in Zetasizer ZS Nano series (Malvern Instrument).

2.7. Atomic Force Microscopy

Atomic Force Microscopy (AFM) is a technique that enables to image surface characteristics of a sample with nm resolution in ambient and liquid condition. In principle, a sharp probe tip – attached to the cantilever is scanned over a surface detecting the local forces interacting between the sample and the probe. Atomic Force Microscopy (AFM) is a technique that provides topographic information with high resolution. Another main advantage of AFM is the possibility to image in liquids. The deflection of the cantilever, caused by the forces acting on the tip, is measured by the laser beam that is focused on the backside of the cantilever and reflected into an array of photodiodes (see Figure 2.12).

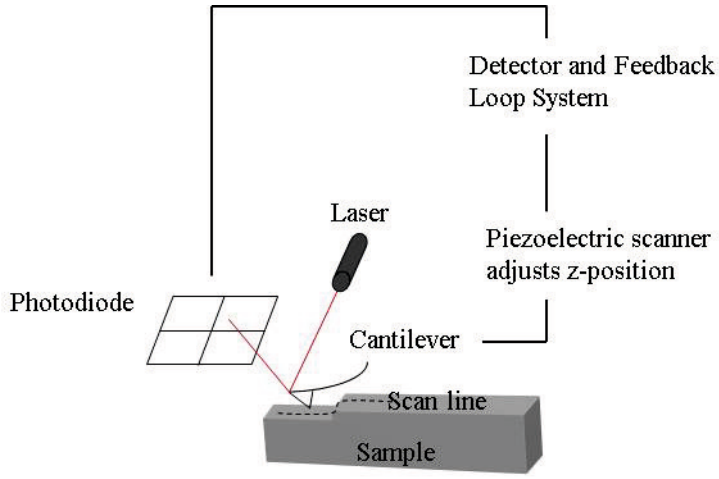

Figure 2.12 Scheme illustrating the scheme of Atomic Force Microscope setup. Detection of the deflection of the cantilever by laser and photodiode. The z-position of the cantilever is adjusted with a feedback loop system.

The AFM sample is connected to a three-dimensional the x,y,z piezoelectric scanner. In the case of static imaging mode, the forces are detected directly by the deflection of the cantilever. The sample can be imaged in three different methods. The topography of the sample is represented by the height (z) of the tip combined with its x-y position. The tip is in hard contact with the surface what could harm soft samples due to high friction between the tip and the sample. Due to that fact, for many biological samples the 'tapping' or intermittent mode is used. After driving the cantilever to its resonance frequency, the tip is brought in the proximity of the sample and the interacting forces between the tip and the surface will cause a shift of the resonance curve and following a change of the amplitude of the oscillation. The contact between the tip and the surface is very short what provides a high resolution of soft samples. Additionally, the tapping mode provides information in the phase image.

2.7.1. Experimental

Topography measurements of phage and nanoparticles were carried out on a commercially available AFM, the Brukers Dimension AFM (Bruker, Billerica, MA; USA). The experiments were performed with silicon cantilever (Olympus AC160). 10 µL of the phages, particles solution and phages mixed with nanoparticles were spread on fresh SiO_2 substrate and allowed to dry for imaging at ambient condition. The AFM images were analyzed with an open source program Gwyddion [117]. The AFM images were leveled by flattering and

adjusting the height to obtain the zero height in the plane level. Profiles were exported and analyzed with Excel.

2.8. Optical microscopy with magnetic set up

Magnetic set up

The sample to be analyzed is held a non-magnetic aluminum sample holder, which is surrounded by a triaxial Helmholtz coils with controller (C-SpinCoil-XYZ, Micro Magnetics Inc.). The sample holder is placed on a xyz motorized translation stage (PT3/M-Z8, Thorlabs) and controlled by supplier software (apt user application, Thorlabs). In order to generate DC magnetic fields 3D-axis Helmholtz coils are used. In both the AC and the DC mode the Earth magnetic field can be cancelled. Using this setup, AC and DC magnetic fields can be applied within the range starting from 0.1 to 2 mT, 0 to 100 Hz. The magnetic field can be applied with the help of the Labview program [118].

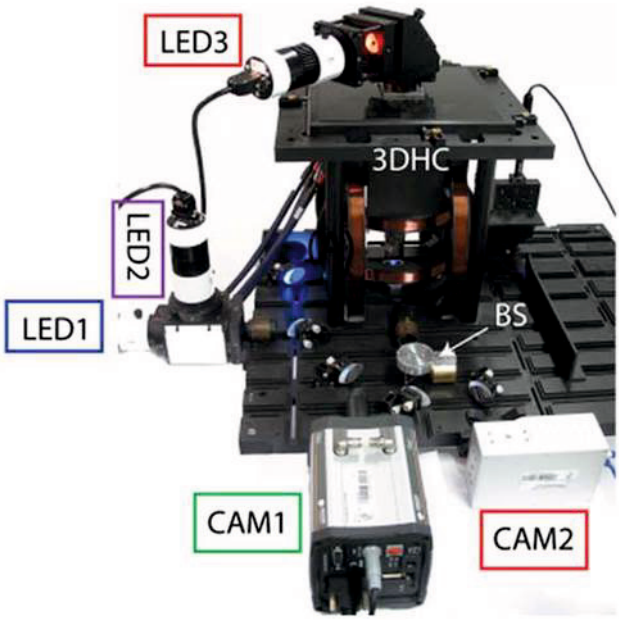

Figure 2.13 An annotated photograph of the optical setup of the microscope platform showing the two fluorescence excitation sources (LED1 and LED2), the 3-dimentional Helmholtz coils (3DHC) in which the sample is placed for examination, the transmission light (LED3), the beam splitter (BS), the fluorescence camera (CAM1) and the high-speed camera (CAM2). Adapted with permission from Bennet et al. 2014 [119]**.**

2.8.1. Experimental

Fluorescence Imaging

The microscope setup also enables fluorescent imaging. Two excitation sources are combined using a dichroic mirror and the sample is illuminated through an objective (60X, NA1.2, WI, Planapochromat, Nikon Gmbh). In order to enable the simultaneous use of the two cameras (high speed and fluorescence) a beam splitter (Thorlabs) is located after the imaging lens. The fluorescent camera (Neo sCMOS, Andor) is controlled using the Andor iQ software (Andor technology).

In order to label filamentous phages with a fluorescent dye, M13 bacteriophage filaments were incubated for one hour, at 4°C with carboxyfluorescein succinimidyl ester (CFSE, Life Technologies) in dimethyl sulfoxide (DMSO, Merck). Probably the dye attaches to the carboxylic groups present on the pVIII protein of the phage. After triple washing with phosphate buffer (0.01 M KH_2PO_4; 0.067 M NaCl; 0.1 mM EDTA; pH 7.4), the phage solution was mixed with unstained PEI NPs and observed in water inside a glass capillary (0.2x2x50 mm, Vitrotubes, Vitrocom) using fluorescent imaging.

Fluorescence imaging using fluorescence confocal microscopy

Fluorescence imaging experiments were performed on a commercial confocal microscope (SP 5, Leica). The laser beam was scanned over the sample using the confocal setup through a microscope objective (60X, 1.2 NA, WI, Leica). The laser scanning and intensity settings were controlled by LASAF (Leica) software.

Phage solution was centrifuged in order to collect the phage pellet and washed by re-suspension buffer in a TBS buffer. This step was performed 3 times and the pellet was finally re-suspended in an aqueous solution containing 1 % low-melt agarose (Sigma-Aldrich) at 30 °C). 30 µl of the suspension was placed between a microscope slide and a coverslip. Agarose formed a gel after cooling the sample down to room temperature. The phages were alive and immobilized while imaged.

High Speed Imaging

For high speed imaging experiments a high speed camera (CR3000x2, Optronics) was used. The illumination for transmission imaging (LED3, see Figure 2.13) is located on top of the microscope, attached to a custom – made holder. The high-speed camera (CAM2) is controlled with the software developed by the supplier (Timebench, Optronics).

Swimmers and propellers selection

20 μL of a mixture of NPs and phage solution were deposited at the bottom of a glass vial containing 600 μL MilliQ - water. The vial was placed in a turning magnetic field in order to select and collect actuated nanostructures. The magnetic field was created using Helmholtz coils of a custom built microscope. In order to check whether the actuated propellers moved to the top of the surface due to other mechanism than magnetic actuation, control experiments were performed. Firstly, the capillary was filled with MilliQ – water, as during the experiment. Samples either with phages or with nanoparticles were placed between coils and magnetic field was applied. In the first case, phages were not detectable whereas nanoparticles were collected forming aggregates without specified shape. Another control experiment was performed. Samples with either phages or nanoparticles were prepared where the magnetic field was not applied. In both cases, no structure was detected.

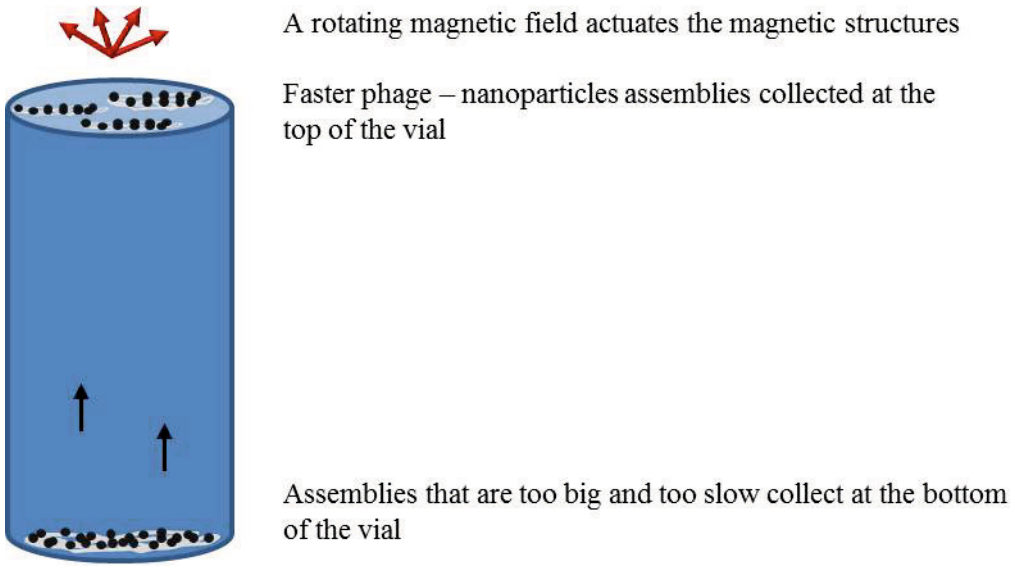

Figure 2.14 Schematic that illustrates the selection process described above. The assembly moves to the top of the vial due to the forces that arise from the rotational and translatory movement.

Speed measurements for random phage-nanoparticles assemblies

Measurements were performed in sealed glass capillaries (0.2×2×50 mm, Vitrotubes, Vitrocom). The mixture of phages and nanoparticles was filled into the capillary, which was subsequently placed in the microscope sample holder with the actuating magnetic field off. After all the structures had settled to the lower capillary surface, the actuating field was switched on and a video of the lower capillary surface was recorded in the center of the capillary. The propeller was firstly moved to the upper surface of the capillary. Afterwards the magnetic field was changed, so that the propeller was moving parallel to the capillary surface. The concentration of the structures was adjusted to a range to avoid hydrodynamic or magnetic interactions between structures. The recorded videos were analyzed by manually searching for start and end positions, in between the structures moved and were not disturbed by the other assemblies.

3. Results and Discussion

3.1. Physicochemistry of the formation of magnetosomes in *M. magneticum*

3.1.1. Preliminary tests on preculture growth

The composition of the growth medium used for the flask cultivation (FSM instead of the typical MSGM) required preliminary tests in order to understand the growth behavior of the AMB-1 strain in these conditions [57] [120]. First of all, the cells were grown under microaerobic conditions, in 500 mL flasks filled with 100 mL growth medium. After 40 h of growth, the cell culture reached an OD_{565} of 0.277. Cell count in Neubauer chamber (BRAND, Wertheim, Germany) was performed in order to relate the OD with the total cell numbers in the conditions typically used in this thesis following the manufacturer instructions. An average of 23 cells per counting square was detected. The cell density was then calculated to be 9.07×10^7 cells / mL. A linear correlation of cell count with the an optical density was assumed, as done in other studies on *Magnetospirillum* [57] such that cell density of 3.27×10^8 cells / mL corresponded to an OD_{565} of 1. This cell density value was used for further normalization of iron content in cells.

Moreover, I investigated the optimal culture time of a preculture and its influence on further growth after inoculation. The OD_{565} and the C_{mag} of the preculture were measured at different time points, directly after inoculation, after 24, 48 and 72 hours. The OD_{565} values of precultures grown until 72 hours are shown in Table 3-1. The growth of the cells is observed until 48 hours of incubation.

Table 3-1 Average OD_{565} and C_{mag} of the tested precultures

Time since inoculation	OD_{565}	C_{mag}
0 hours	0.126 (±0.003)	0.05 (±0.009)
24 hours	0.733 (±0.04)	0.09 (±0.009)
48 hours	1.113 (±0.051)	0.03 (±0.01)
72 hours	1.092 (±0.081)	0.01 (±0.007)

The results shown in Figure 3.1do not show significant differences between 1, 2, or 3-day old inoculum. After 24 hours of the cell growth, all the cells reached an OD_{565} of around 0.4. 48 hours old precultures were used as an inoculum for the bioreactor cultivation.

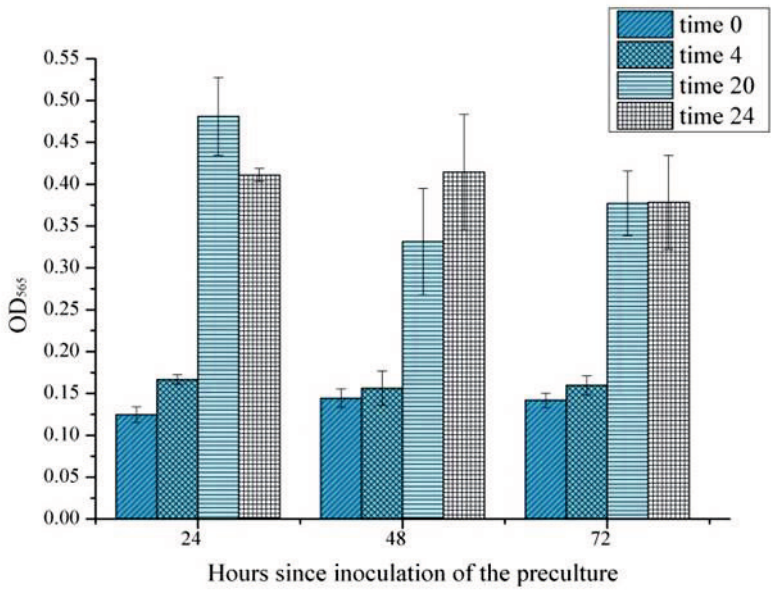

Figure 3.1 Results of the preculture measurements. A preculture was inoculated after 24, 48 and 72 hours and the OD of the culture was observed after 0, 4, 20 and 24 hours.

3.1.2. Toxicity tests of the chemicals used to control the redox state

Titanium (III) citrate has already been utilized as a reductive compound for microorganism growth [59]. No major toxicity was reported for an anaerobic bacterium such as *Clostridium formicoaceticum* or for *Pseudomonas denitrificans* as a representative of a facultative anaerobic bacterium [121]. The chemical is therefore putatively a compound of choice to control the ORP during the cultivation of AMB-1. I tested the effect of different concentration of the cellular growth. Increasing the concentration in the medium from of 0.22 mM to 15 mM, the growth was still observed, but inhibited (see Figure 3.2.).

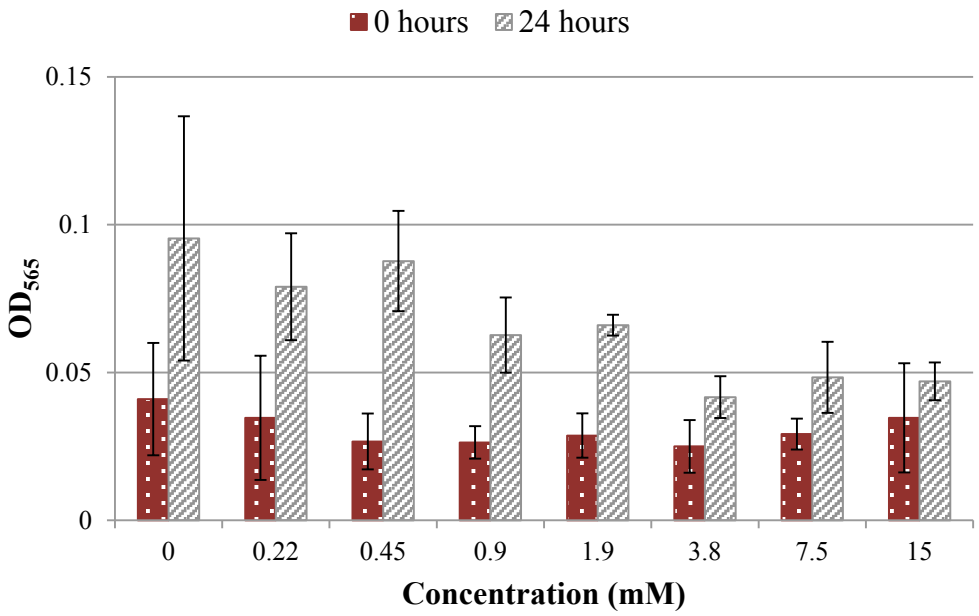

Figure 3.2 Toxicity test for a range of Titanium (III) citrate concentrations used during *M. magneticum* strain AMB-1 cultivation. The AMB-1 cultures were grown in 500 mL flasks bubbled with N_2 in order to sustain anaerobic conditions. 10 mL of the preculture was used as an inoculum for each flask. Culture without Titanium (III) citrate served a control. Optical density (OD_{565}) was measured for each concentration immediately after the inoculation (t0, brown bars) and after 24 hours of cell cultivation (t24, grey bars). Error bars represent the standard deviation of the three repetitions.

In particular, the growth of the control culture, without the addition of titanium (III) citrate, gave after 24 hours of growth an average OD_{565} of 0.095 (±0.041). This optical density was comparable to the OD_{565} of the culture grown with 15 mM titanium (III) citrate. The concentration of 15 mM of titanium (III) citrate was much higher than one used during further experiment in the bioreactor, but cells were still able to growth. The final concentration of

titanium (III) citrate used during bioreactor cultivations was 5 mM. Therefore, there were no objections to use this component for further experiments.

The second chemical, potassium ferricyanide, used as an oxidizer, was tested as well for its toxicity. The growth of cells, grown in flasks containing different concentrations of potassium ferricyanide, was measured directly after inoculation, and after 24 hours. The results (shown in Figure 3.3) indicate that at the concentrations of 3.6 mM of potassium ferricyanide, cell growth is strongly inhibited. The final concentration used during fermentation was however only 0.3 mM, for which no clear inhibition was observed.

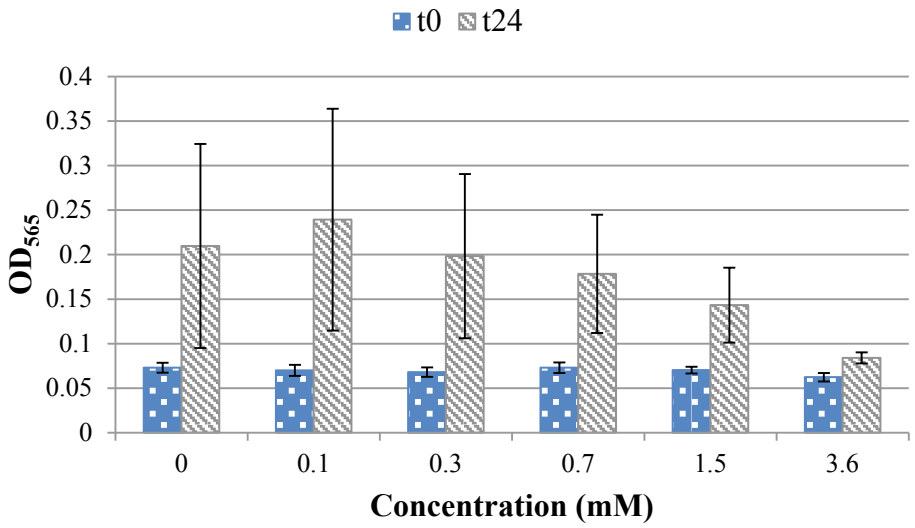

Figure 3.3 Toxicity test for a range of Potassium ferricyanide used during *M. magneticum* strain AMB-1 cultivation. The AMB-1 cell were grown in 500 mL flasks bubbled with N_2 in order to sustain anaerobic conditions. 10 mL preculture was used as an inoculum for each flask. Culture without Potassium ferricyanide served a control. Optical density (OD_{565}) was measured for each concentration immediately after the inoculation (t0, blue bars) and after 24 hours of cell cultivation (t24, grey bars). Error bars represent the standard deviation of the three repetitions.

Both tests confirmed that the concentration of either titanium (III) citrate or potassium ferricyanide decreases the cell growth at high concentration. However, at moderate concentrations as such used for fermentation, only a moderate impact was recorded in term of growth. After 24 hours of incubation, the cells grown with potassium ferricyanide (Figure 3.4 a) and with titanium (III) citrate (Figure 3.4 c) respectively did not exhibit any change in

cellular morphology. In both cases, the cells of *M. magneticum* exhibit a short spiral shape, typical for this strain (Figure 3.4 b).

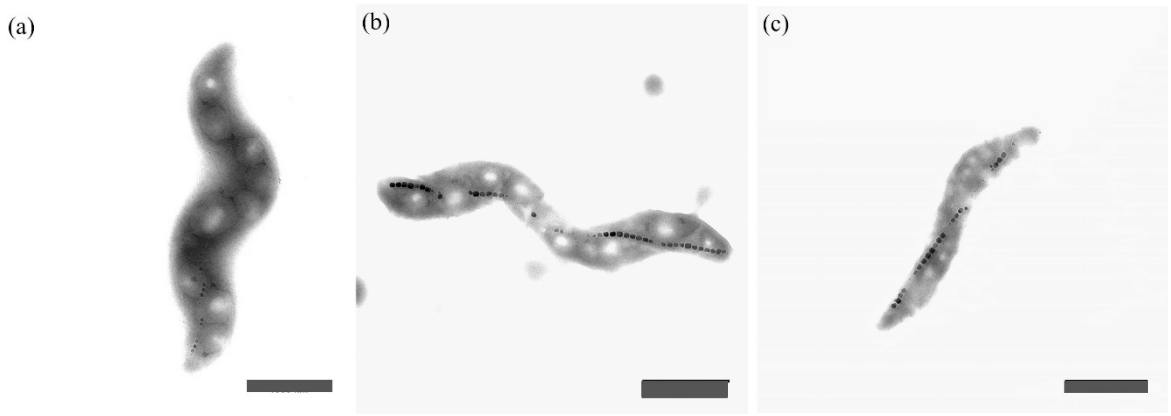

Figure 3.4 Transmission Electron Images of *M. magneticum* cells after 24 hours of cultivation: (a) with potassium ferricyanide, at ORP 0 mV; (b) without any additions of chemicals regulating ORP - Control experiments; (c) with Titanium (III) citrate, at ORP – 500 mV; Scale bars 1 µm.

3.1.3. Effect of ORP on cell growth and properties

The bioreactor system enables precise control of temperature, pH, steering speed, and N_2 flow in order to maintain constant conditions. The only parameter I changed during this work was the ORP. The experiments were accordingly performed at constant and controlled: temperature, pH, anaerobic conditions, and stirring speed whereas the ORP was changed by setting the reduced conditions with titanium (III) citrate and the oxidized conditions with potassium ferricyanide.

Observation of ORP and pH change in the bioreactor

I first conducted control experiments in order to understand the behavior of the AMB-1 cells in the bioreactor. As shown in Figure 3.5, even if the pH is buffered, the cells tend to increase it. Therefore, pH was controlled by the feedback system of the bioreactor while cell growth. 0.5 M H_2SO_4 was added systematically when pH was overcoming the value of 7.20. pH of the test fermentation (without cells) remained stable during the whole process (see Figure 3.5).

No pH increase in the control fermentation indicates that cells tend to increase the pH of the medium, which indicates that during growth bacteria secrete metabolites, which alter the pH of the media.

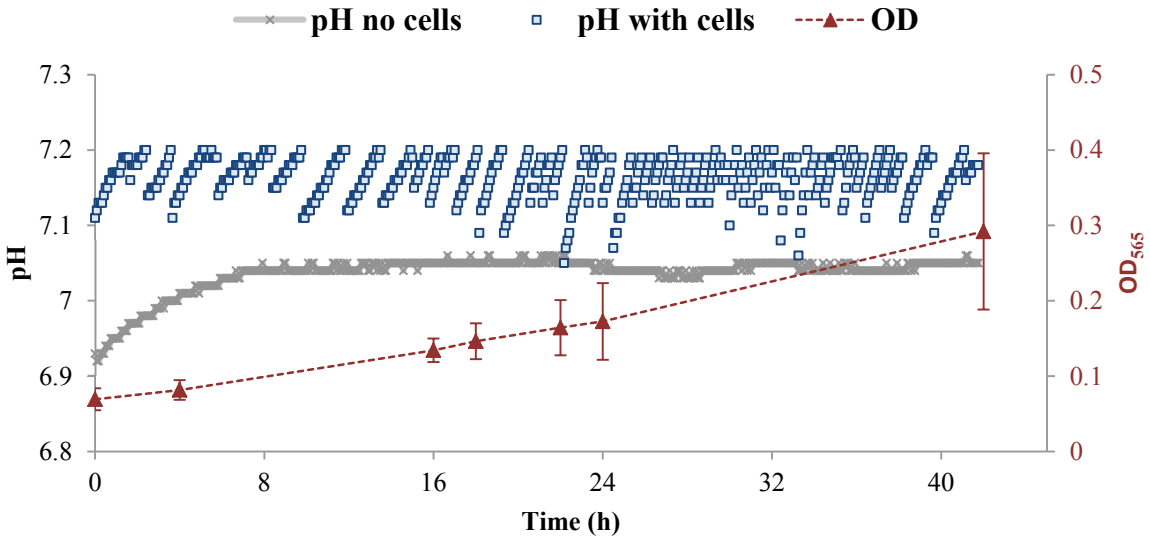

Figure 3.5 pH continuous measurements of two controls. One was performed with cells (pH – blue squares) while the second one was done without cells (pH – grey crosses). Growth of cells is shown as optical density measurement at the wavelength 565 nm (OD_{565}). OD_{565} is shown as red triangles connected with dashed red line.

The same procedure was repeated with the ORP. The values reported in Figure 3.6 are increasing over time during control cultivation with cells (indicated by dark blue circles). ORP measurement showed that the medium without cells settles around – 300 mV (grey crosses in Figure 3.6). I found that the ORP in blank medium is influenced by the daily light cycle with an increase of around 20 mV for daylight conditions with respect to darkness (i.e. night). This timeframe matched with the daily hours when light was present in the laboratory room. It could be possible that some photochemical reaction takes place in the medium.

In turn, during cell growth, the ORP values rapidly decrease during the first hours to reach a minimum value of - 209 mV. After ca. 10 hours, the ORP values start to increase and finally stabilize around - 200 mV. Investigated bacteria generated E_h leaps not connected with pH and pO_2 changes. The AMB-1 growth indicated by OD_{565} (Figure 3.5 and Figure 3.6) does not show the typical growth curve with sharp differences between logarithmic and stationary

growth phase, potentially because the frequency of sampling was not sufficient enough to monitor it, but E_h indeed increases during the cell growth (see Figure 3.6). Other studies connect trends in ORP with a metabolism of bacteria in anaerobic cultivations.

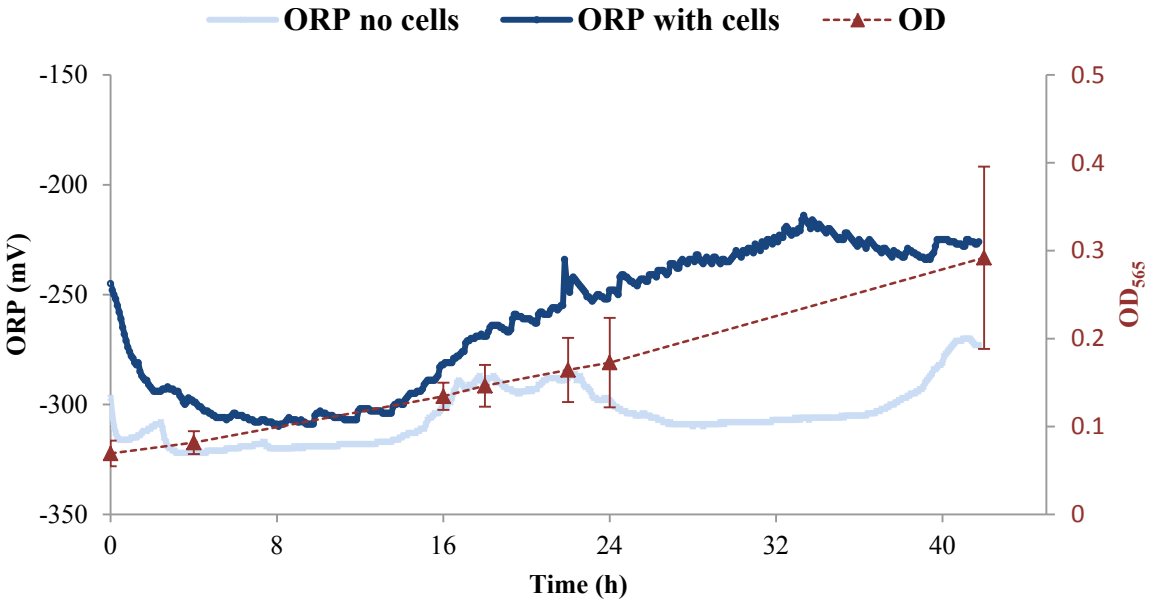

Figure 3.6 ORP continuous measurements of two controls. One was performed with cells (ORP – dark blue) while the second one was done without cells (ORP – light blue crosses)). Growth of cells is shown as optical density measurement at the wavelength 565 nm (OD_{565}). OD_{565} is shown as red triangles connected with dashed red line.

Cell growth as a function of ORP

The optical density (OD_{565}) as a measurement of cell density and thus of cell growth was measured for every experiment i.e. 0, 4, 16, 18, 22, 24 and 42 hours after inoculation. The measured OD_{565} values are presented in Figure 3.7. Due to the practical limitations, it was not possible to measure the OD_{565} continuously. The reported division time of *M.magneticum* grown under microaerobic conditions is around 10 hours [122]. *M.magneticum* were grown in this study under anaerobic conditions, which did not represent the most favorable conditions so that I recorded an increased division time of 20 hours.

The final OD_{565} of cells after 42 hours of cultivation was higher for ORP -500 mV in comparison with ORP 0 mV. At ORP – 500 mV cell yields reached OD_{565} of 0.324, while at ORP 0 mV the OD_{565} was 0.230. One of the control fermentations, at the time of 42 hours

showed lower values. OD_{565} after 42 hours came to 0.173, which shows that cells grew less than during ORP control. This could be explained by the low initial cell density at the beginning of the experiment (OD_{565} = 0.053) as the experiments usually started with OD_{565} around 0.070. At ORP 0 mV, the OD_{565} values were much lower, but the growth was not inhibited. It was shown that on the *E.coli* fermentative growth was inhibited by $K_3[Fe(CN)_6]$. $K_3[Fe(CN)_6]$ affected H^+ and K^+ fluxes through the membrane, decreased K^+ accumulation and delayed a decrease in E_h by bacteria [59]. This is first study describing growth of *M.magneticum* under the influence of $K_3[Fe(CN)_6]$ as an oxidant.

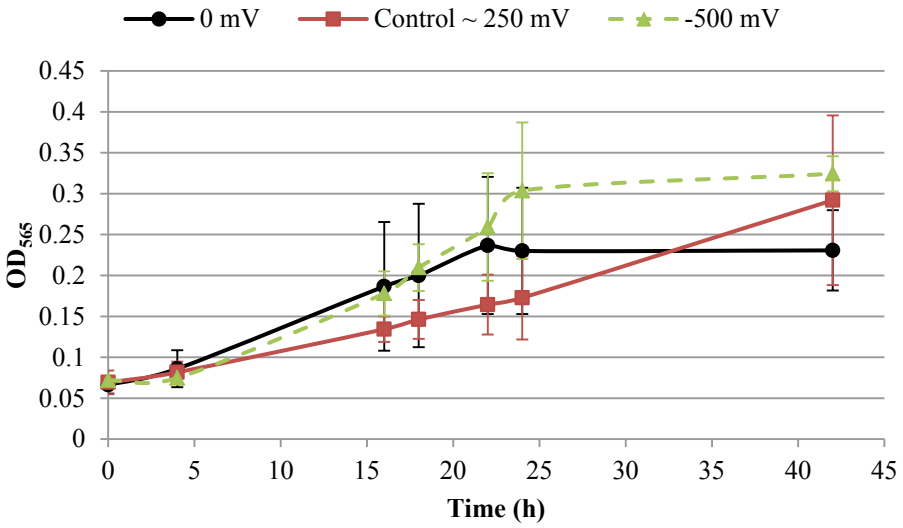

Figure 3.7 Results of measurements of *M. magneticum* AMB-1 strain growth rate measured as optical density (OD_{565}) for experiments performed in the bioreactor.

Cellular iron concentration as a function of ORP

Pellets of cells were collected by centrifugation and iron content was measured via ICP-OES in order to understand how much iron is accumulated in the AMB-1 cells during the fermentation process. The remaining medium was investigated as well in order to monitor the iron loss during the cultivation process. The results of the iron content in pellets indicate that the iron concentration in the cells (mg/L) increases during bacterial growth (Figure 3.8). The increase of iron in pellet is primarily related to the increased cell yield. Cells take up more iron under reduced conditions (ORP -500 mV in Figure 3.8); in comparison with oxidized medium.

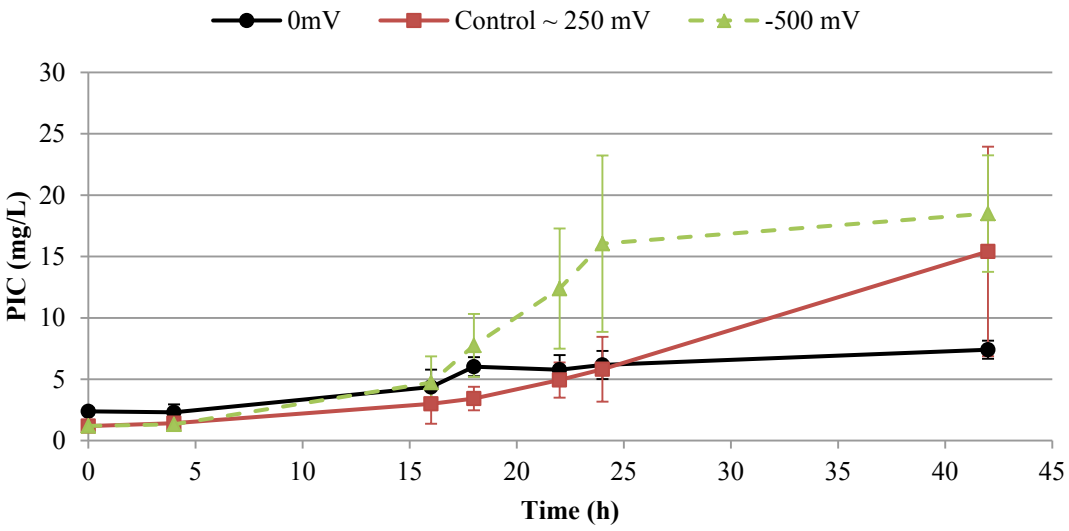

Figure 3.8 Pellet iron content (PIC). The graphs represent raw data as delivered from ICP-OES measurements. ORP 0 mV is shown as the black line with circles; Control – red line with squares; ORP – 500 mV – green line with triangles.

The results of iron content in medium show a trend in the decrease of iron during cell cultivation (Figure 3.9). Octahedrally coordinated iron, $[Fe(CN)_6]^{3-}$, enclosed within the complex, is not available for cell to be taken up and efficiently stabilizes the ORP of the whole bioreactor system. But due to its presence in the medium, the iron content at 0 mV, measured via ICP-OES will be inaccurate. Therefore, only the results from the pellets measurements are used for further analysis. The results were compared to the cell dry mass using the value provided by [57], which reported a culture density at OD_{565} = 1, a dry weight of 0.28 g. The value is however only a rough indicator of the iron uptake, since it can be strongly influenced by the differences in cell morphology and cell density.

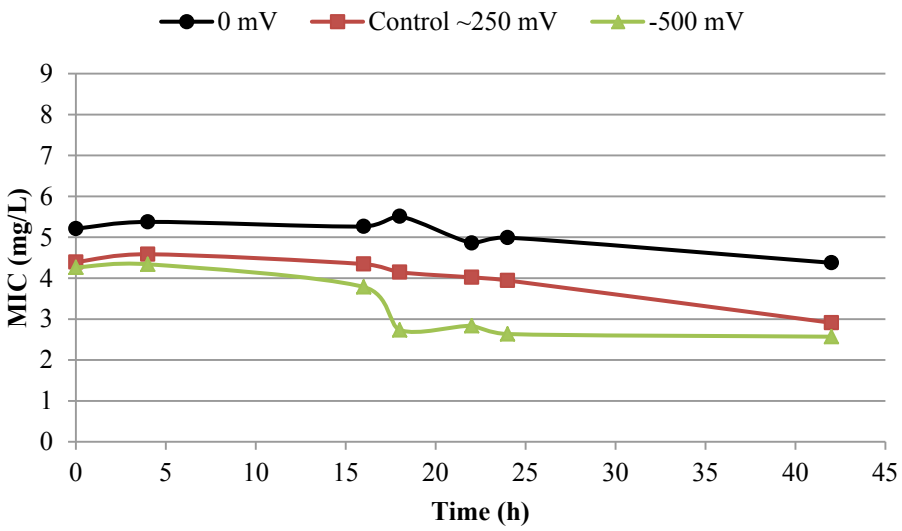

Figure 3.9 Medium iron content (MIC). The graphs represent raw data as delivered from ICP-OES measurement. ORP 0 mV is shown as the black line with circles; Control – red line with squares; ORP – 500 mV – green line with triangles. In the case of ORP 0 mV, from the measurement in medium, the amount of potassium ferricyanide added to regulate the ORP is subtracted.

In order to better compare the differences obtained for optical density, cell magnetism and iron content per dry weight under the different tested conditions (control, reduced (ORP -500 mV), and oxidized (ORP 0 mV) conditions) the different parameters are summarized in Table 3-2. The data are shown for 42 hours of fermentation. The OD_{565} reached the highest values (0.324 ± 0.021) at ORP – 500 mV while cells grew the least at ORP 0 mV (OD_{565} 0.238 ± 0.069). The magnetic response of cells (C_{mag}) also indicates that cells grown under reduced conditions (ORP – 500 mV) responded stronger (C_{mag} 0.75) than cell grown under oxidized conditions (C_{mag} 0.46). The influence of redox change on iron content in cells is even more evident by comparing iron content per dry weight. At ORP – 500 mV the iron content was much higher (12.76 mg/g dry weight) than at ORP 0 mV (7.36 mg/g dry weight).

Table 3-2 Averaged results of the cell growth experiments in the bioreactor at ORP – 500 mV, 0 mV and controlled conditions without ORP control; after 42 hours of cultivation. Optical density (OD_{565}), cell magnetism (C_{mag}) and iron content per dry weight are reported.

	ORP -500 mV	Controls	ORP 0 mV
OD_{565} (42 hours)	0.324 (±0.021)	0.292 (±0.104)	0.238 (±0.069)
C_{mag}	0.75 (±0.255)	0.66 (±0.326)	0.46 (±0.072)
Iron (mg/g dry weight)	12.76 (±3.42)	11.36 (±2.93)	7.36 (±1.98)

The calculations of iron content per cell were performed including the measurements of cell density, and subsequent cell count experiment (see section 3). Iron uptake increases with a decreasing redox potential in the medium (see Figure 3.10). At ORP of - 500 mV, after 42 hours of growth, the cells took up an average of 1.56×10^{-9} µmol Fe / cell. During the control experiments the average amount of iron decreased to 1.37×10^{-9} µmol Fe / cell. Finally 9.09×10^{-10} µmol Fe / cell was recorder at an ORP of 0 mV. The lowest iron content per cell, which occurred under the oxidized conditions, was one order of magnitude lower when compared to Control and ORP – 500 mV.

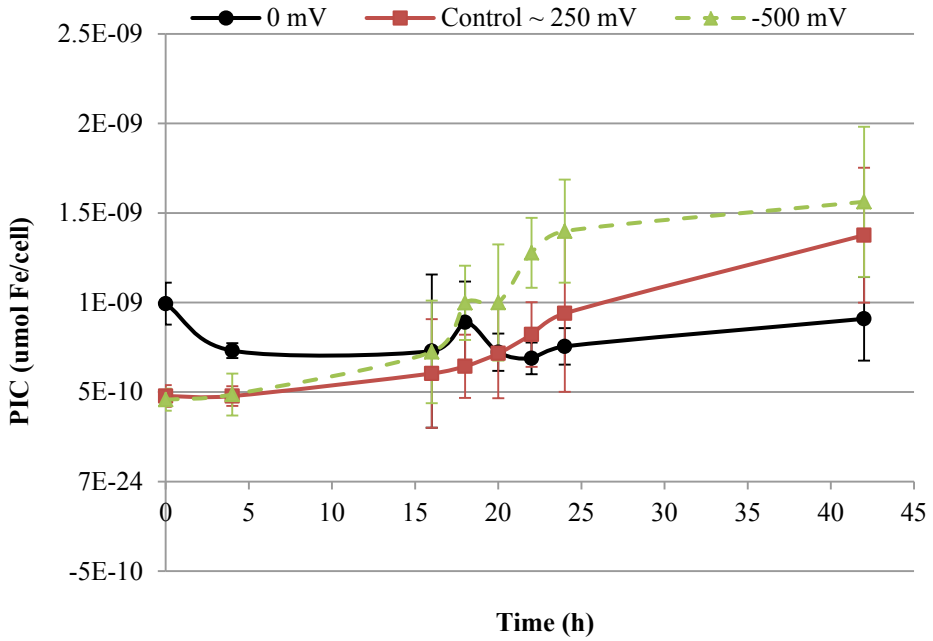

Figure 3.10 Pellet iron content (PIC) normalized for cell number. The iron content is presented as iron concentration µmol Fe per cell. Iron concentration was calculated from data delivered from ICP_OES. The calculations of iron content included cell density measurements, and subsequent cell count experiment. ORP 0 mV is shown as the black line with circles; Control – red line with squares; ORP – 500 mV – green dashed line with triangles.

Even if the effect of ORP on the uptake of iron is evident and iron amount decreases with ORP increase, iron content in pellets, measured via ICP-OES does not give precise information about the intracellular iron; precisely how much iron is really considered as intracellular. Therefore additional negative control experiments were performed with the mutant *Δmam AB* of *M.magneticum*. *Δmam AB* cells are not able to biomineralize magnetosomes due to *mamAB* operon deletion, which causes the loss of magnetosome formation [123]. Owing to this fact, it was possible to calculate the amount of iron that accumulates on the surface of the cells.

The results of optical density as well as iron content in pellets obtained for this strain are shown in Figure 3.11. The cells that were grown under reduced conditions accumulated lower amount of iron, in comparison to cells grown under oxidized conditions. The iron measurements of cells grown under ORP 0 mV showed large fluctuations, even though OD_{565} remains stable. The control experiments show that it is more likely that the iron uptake measurements could be overestimated for ORP 0 mV, compared to ORP – 500 mV, changing the results reported. The amount of iron per cell, after 42 hours, at ORP 0 mV was 1.56×10^{-9} µmol Fe/cell. The cells didn't exhibit significant growth (OD_{565} 0.054) compared with the growth of cells at ORP – 500 mV (OD_{565} 0.098). The iron nucleating on the cell surface, grown at ORP – 500 mV, after 42 hours reached 4.5 µmol Fe/cell what is one magnitude lower than iron nucleated on cell at ORP 0 mV. Control experiments performed on *ΔmamAB* mutant indicate that the accumulation of iron on the cell surface depends on ORP and in consequence inhibition of iron uptake in AMB-1 under ORP 0 mV is even stronger. In order to confirm the hypothesis, it is necessary to repeat the experiment with increased yield of mutant cells to better see the effect of iron accumulating on the cell surface.

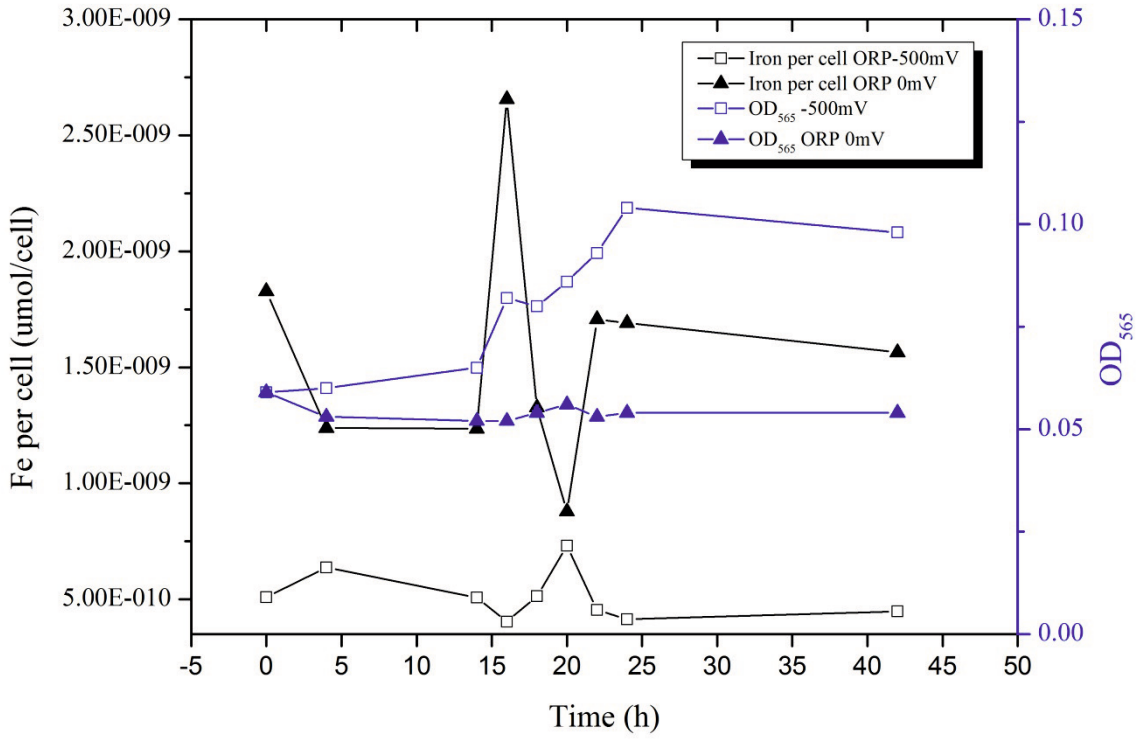

Figure 3.11 Results of the negative controls performed with *M. Magneticum* ΔmamAB mutant. OD_{565} at ORP – 500 mV is represented as blue, empty squares; OD_{565} at ORP 0 mV is represented as blue, triangles; Pellet iron content (PIC) in cells grown at ORP – 500 mV is shown as black, empty squares; Pellet iron content (PIC) in cells grown at ORP 0 mV is presented as black, filled triangles.

Effect of ORP on cell length

The cells were investigated using an optical microscope (imager A2 AXIO-microscope, Zeiss, Gemany) at 39.69 x magnification. Images at different stages of bacterial growth were taken, but for further analysis only images at time 0 and 42 hours were analyzed. The length of 100 cells was analyzed for each tested condition. The length of bacteria was determined using the ImageJ software [109].

The measurements of the bacterial lengths showed that they differ depending on the experimental conditions. During controlled fermentations, the average length of the cells was 3.96 µm (± 2.73), with a maximum of 17.23 µm. At ORP – 500 mV, the cells had an average length of 6.25 µm (± 5.13), with the longest cell measured being 35.27 µm long. Cells grown under oxidized conditions, at ORP 0 mV, were the longest measured, having an average of 8.68 µm (±5.65) and the maximum of 29.01 µm.

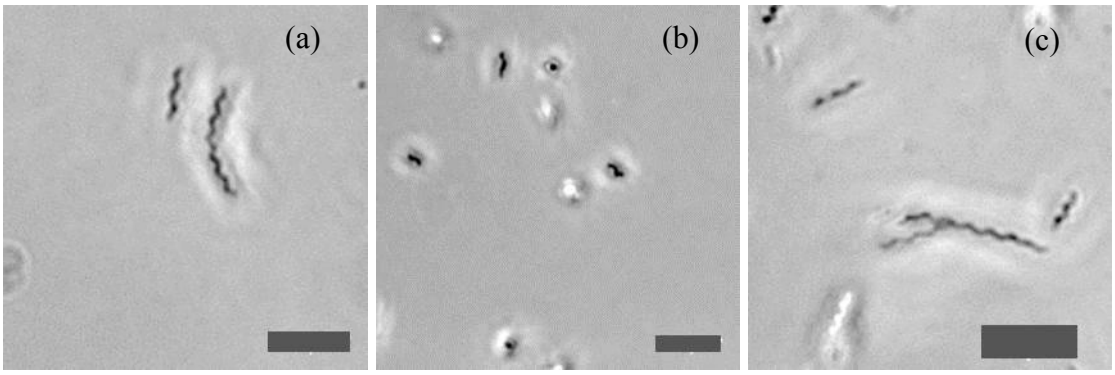

Figure 3.12 Exaples of the optical microscope images of *M. magneticum* cells. Image (a) Cells grown at ORP 0 mV; Image (b) Control - cells grown without ORP control; Image (c) Cells grown at ORP -500 mV. Scale bars 10 µm

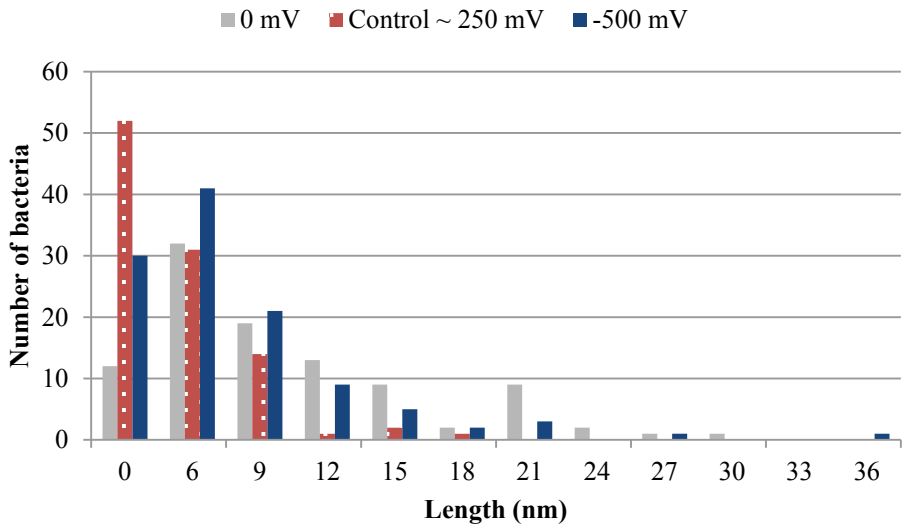

Figure 3.13 Overview of the length distributions of AMB-1 cells grown at different redox conditions. ORP 0 mV (grey columns); Control ORP –250 mV (red columns); ORP-500 mV (blue columns).

Effect of ORP on the number of magnetosomes per cell

The average values of the amount of magnetosomes per cell are shown in Table 3-3. Due to the fact that cell showed different length as a function of the conditions in which they were cultivated, the number of magnetosomes per cell was also normalized to the length of the cell, providing an average value of magnetosomes per micrometer to assess for their biomineralizing capacities. In this case, the cells grown under reduced conditions (ORP - 500

mV) possess more magnetosomes per cell (63.4 ± 27.7) in total. In turn, similar number was achieved during control experiments (34.6 ± 2.8) as well as at ORP 0 mV (28.3 ± 8.5). At ORP - 500 mV, the number of magnetosomes per micrometer equals 9.1 ± 1.9, at ORP Control 8.6 ± 1.5, while only 5.5 ± 1.3 are reached at ORP 0 mV.

Table 3-3 Quantitative measurements of magnetosomes and particle size measurements obtained via analysis of transmission electron microscope images.

Growth condition	**Number of magnetosome per cell**	**Number of magnetosome per micrometer**
Control	34.6 (± 12.8)	8.6 (± 1.5)
ORP 0 mV	28.3 (± 8.5)	5.5 (± 1.3)
ORP -500 mV	63.4 (± 27.7)	9.1 (± 1.9)

Transmission electron microscopy images shown in Figure 3.14 represent examples of cells grown under different ORP conditions. What can be seen is that magnetosomes synthesized at ORP 0 mV (Figure 3.14 b) look dwarfed and smaller than magnetosomes synthesized at ORP – 500 mV (Figure 3.14 c) and at ORP control (Figure 3.14 a).

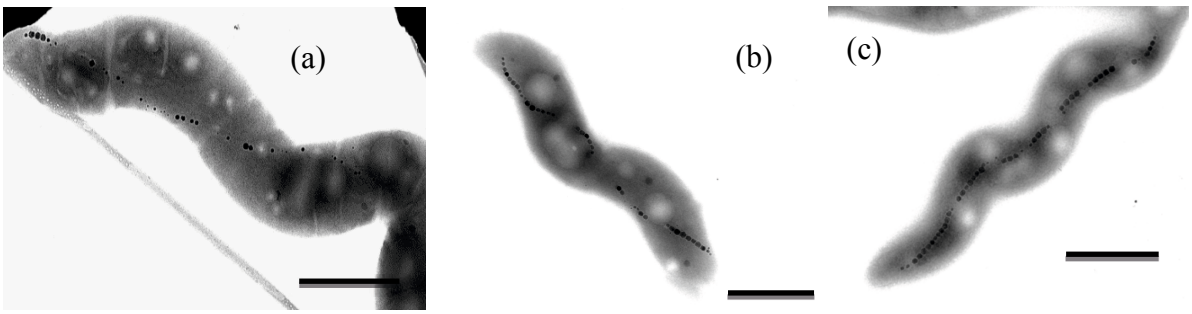

Figure 3.14Examples of the images taken with TEM microscope. ORP 0 mV (a); Control culture (b); ORO - 500 mV (c). Scale bar 1µm

The quantification analyses of particles from *M. magneticum* AMB-1 strain shown in Figure 3.15 represent the overview of the distribution of magnetosomes per cell. The amount of magnetosomes was counted from TEM images for 100 cells per conditions applied. Under

controlled conditions, the sizes of magnetosomes are distributed between 10 and 90 nm. The distribution of number of magnetosomes at ORP 0 mV is asymmetric with cut-off towards smaller amounts, < 50 nm. The number of magnetosomes in cells grown at ORP – 500 mV is shifted towards bigger amounts, reaching almost 140 magnetosomes per single cell.

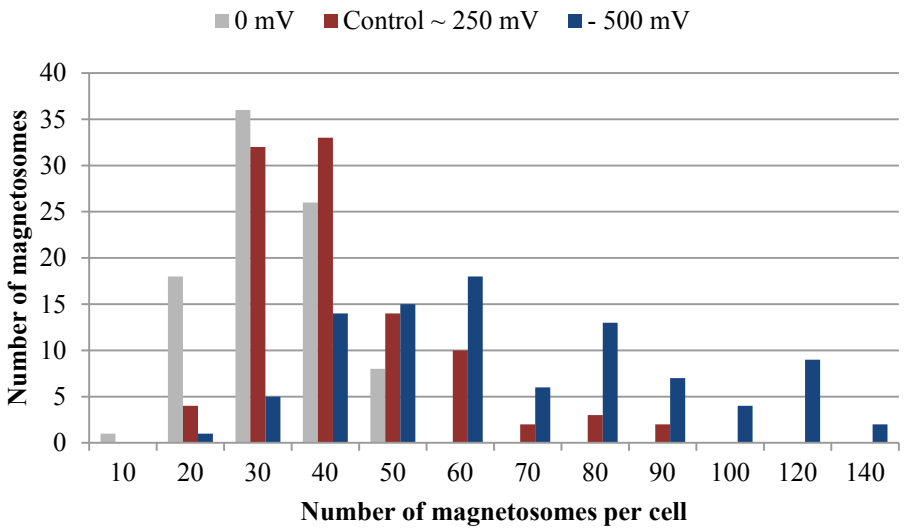

Figure 3.15 Overview of the distribution of the number of magnetosomes per cell, counted by analyzing transmission electron images. Control (red column); 0 mV (grey column); - 500 mV (blue column).

Size of magnetosomes

The analyses of particles from *M. magneticum* AMB-1 were performed to quantify the size distributions of magnetosomes. Crystal borders were digitized from TEM images and their dimensions estimated by calculating the best fit of ellipse to the contours [124]. The major and minor axes of the crystals were analyzed and the surface of the ellipse was calculated. The sizes reported in Figure 3.17 are the dimensions reported for the diameter of the surface of the circle that has the same surface as the surface of an ellipse with known major and minor dimensions. As mentioned in the previous paragraph, a trend in magnetosomes amount and size is visible among tested conditions, what can be seen as well in Figure 3.16, showing examples of transmission electron microscopy images of AMB-1 cells. ORP – 500 mV showed the highest magnetosome size, controls exhibited similar values, while ORP 0 mV showed the lowest size of particles.

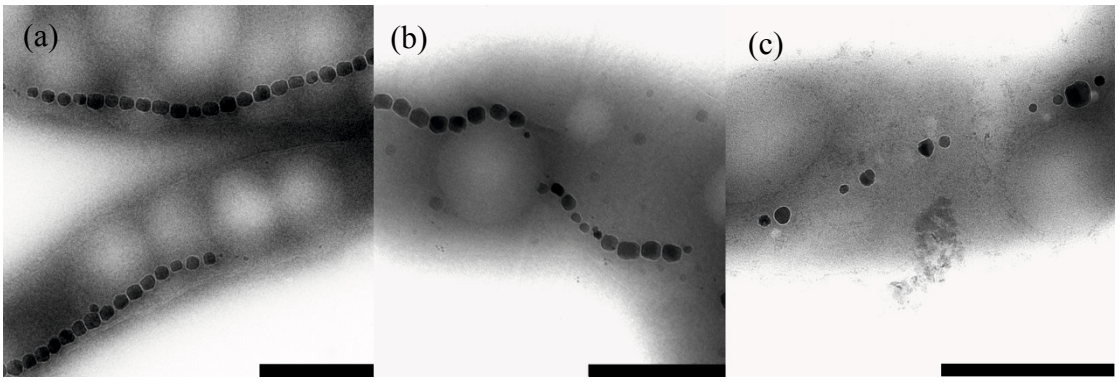

Figure 3.16 Close up images of the magnetosome chains. In panel "a" ORP -500 mV, in panel "b" control, and in panel "c" (scale bar 500 nm).

Li & Pan showed that the average magnetosome size in AMB-1 cells grown under anaerobic conditions was 41.5 ± 15.0 nm with the average shape factor, determined from TEM images, of 0.78 [56]. The magnetosome sizes obtained at ORP – 500 mV and controls are 50.8 ± 13.6 and 46.7 ± 15.7 nm respectively, in agreement with previous study [56], but it is important to mention that many small particles might have been excluded from the measurements due to the filtering the particle area, at 225 nm^2 particle area and at a roundness of 0.7. This issue had a strong influence, especially at ORP 0 mV, where the average size of magnetosomes was 34.5 ± 12.3 and where in particular many magnetosomes were underdeveloped and certainly have not reached mature size. The roundness filter was indeed necessary in order to select magnetosomes from other dark points occurring in TEM images.

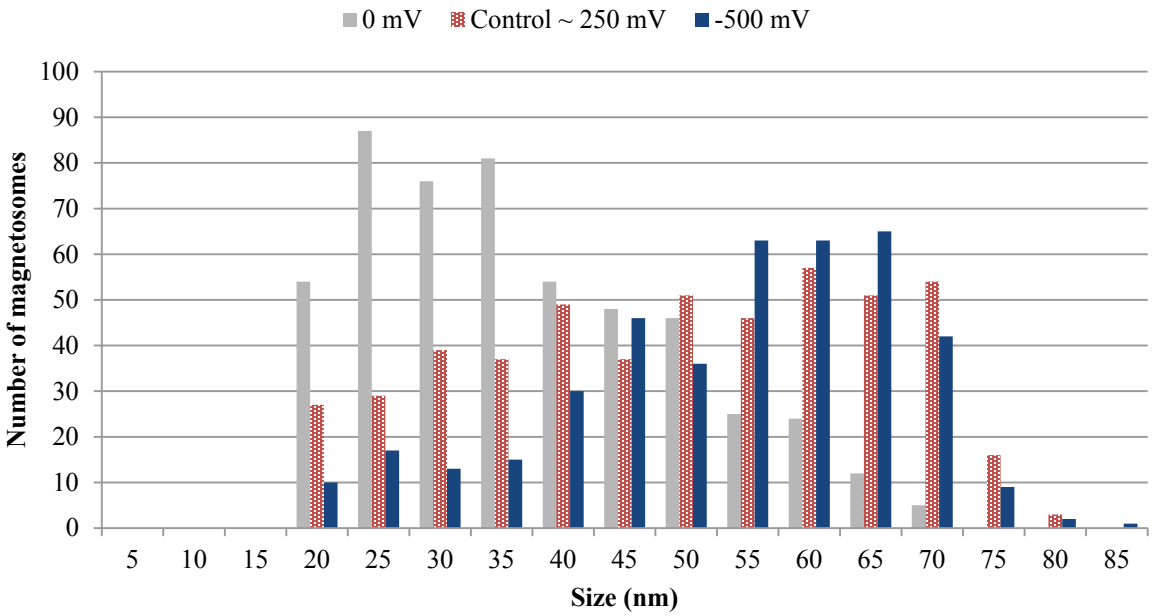

Figure 3.17 Distribution histograms particle diameters for magnetosomes delivered from transmission electron images analyzed with ImageJ program. Distribution of magnetosome sizes synthesized at ORP 0 mV is shown in grey, dashed; size distribution at ORP – 500 mV is shown as blue columns; size distribution for control experiment is shown as red, dashed columns.

In the Table 3.4., the nanoparticle diameter measured via X-ray diffraction is compared with the sizes calculated via photomicrographs analysis to confirm the hypothesis that ORP 0 mV cause the decrease in the size of magnetosomes. What can be seen is that the trend in the decrease of particles size obtained by both methods for ORP 0 mV is similar. Nanoparticle diameter of nanoparticles measured via X-rays equals 31.5 nm ± 1.3 while size of nanoparticles measured via image analysis is 34.5 nm ± 12.3. The size of nanoparticles synthesized at ORP – 500 mV (50.8 nm ± 13.6) and control experiments (46.7 nm ± 15.7) showed higher crystals sizes than the sizes obtained via x-ray diffraction; ORP – 500 mV – 37.2 nm± 0.6, ORP Control – 37.2nm ± 0.8.

Table 3-4 Mean magnetosome size measurements analyzed with X-ray diffraction method, compared with maximum and minimum magnetosome diameter obtained by transmission electron images analysis via ImageJ.

Growth conditions	Nanoparticles diameter (x-ray diffraction)	Magnetosome diameter (ImageJ analysis)
Control	37.2 (± 0.8)	46.7 (±15.7)
ORP – 500 mV	37.2 (± 0.6)	50.8 (±13.6)
ORP 0 mV	31.5 (± 1.3)	34.5(±12.3)

3.1.4. Discussion

In this work, the formation of magnetosomes was monitored during cultivation in the bioreactor. It was shown that ORP has a strong impact on the formation of these nanoparticles. In general, several factors have been found to influence the formation of magnetosomes, the most important being the concentration of oxygen and the presence and reduction of nitrogen oxides [125]. Blakemore et al. reported that microaerobic conditions are required for magnetite production in *Magnetospirillum magnetotacticum* [126]. Schüler and Bäuerlein showed that formation of magnetite in *Magnetospirillum gryphiswaldense* in non-magnetic cells occurs at the concentration of oxygen of about 2 to 7 µM at 30 °C [54]. Matsunaga et al. showed that the cells of *Magnetospirullum magneticum* AMB-1 strain produce magnetite microaerobically and anaerobically using nitrate as the terminal electron acceptor [63]. Nitrate is believed as well to strongly influence the formation of magnetite in MTB [125]. Jogler et al showed that *Magnetospirillum* species and MV-1 are capable of anaerobic growth with nitrate or N_2O as terminal electron acceptor respectively [127]. These studies imply that the formation of magnetite in MTB is indeed limited to chemical environment. Iron is a redox reactive, very efficient electron carrier, and because both forms Fe^{2+}/Fe^{3+} are present in magnetite, it is important to understand the role of enzymatic iron oxidation and reduction in magnetite synthesis. The studies on variations of ORP values due to the different oxygen concentrations [42, 44, 58] do not describe oxidizers other than oxygen; also in comparison with reducing agent, used to control the biomineralization process occurring in magnetotactic bacteria.

Redox state control

Chemicals with different degrees of reduction such as potassium ferricyanide or titanium (III) citrate are redox reagents, which can be supplemented into cultivation systems as electron carries affecting environmental ORP and intracellular metabolism. These two compounds: potassium ferricyanide and titanium (III) citrate were chosen due to their utilization in regulation of redox potential in bacterial growth. Titanium (III) citrate was used as a reducer by Jones & Pickard in the laboratory growth of rumen bacteria [128]. The effect of potassium ferricyanide has been tested in ORP regulation of fermentation process with *Escherichia coli* by Bagramyan et al. [59]. Oktyabrsky & Smirnova have proved that the jump in E_h can be measured in the transition from logarithmic growth to stationary growth phase in *E. coli* and *B. subtilis* and is caused by glucose and ammonium exhaustion in the growth medium [129]. For example the study done by Bagramyan et al describing the effect of $K_3[Fe(CN)_6]$ on bacteria growth showed that this impermeable oxidant under anaerobic conditions affects the growth of *E. coli* by influencing membrane transport mechanisms [59]. The toxicity of both titanium (III) citrate and potassium ferricyanide, used for the ORP control in AMB-1 cultivation was checked by monitoring the cell growth under different concentrations of these chemicals. Toxicity tests showed that the concentration of chemicals used for bioreactor cultivation does not influence the cell growth. The redox control during the cultivation of AMB-1 cells under reduced and oxidized conditions was successfully achieved by using either titanium (III) citrate or potassium ferricyanide. Perhaps chemicals used to control the redox state of the growth medium has an effect on the structural distortions of the AMB-1 cell surface and it should be considered but nevertheless redox change in this study is only focused on the formation of magnetosomes.

Effect of ORP on the number and the size of magnetosomes per cell

The quantitative analyses describing the number of magnetosomes per cell and their size showed that reduced conditions favor magnetosome formation whereas under oxidized conditions the formation of magnetosomes is inhibited. This can be confirmed by the size and amount of nanoparticles occurring as smaller and fewer at ORP 0 mV. The average number of magnetosomes per cell at ORP 0 mV was twice smaller than in cell grown at ORP – 500 mV, what suggests that strongly reducing conditions foster iron uptake mechanism and increase the yield of produced nanoparticles. The study described in this thesis showed that by

influencing the redox state of the growth medium, it is possible to increase the yield of magnetosomes produced by MTB. This would have strong impact on the potential usage of such particles in different applications [130]. The size of magnetosomes and the length of magnetosomes chains were investigated by Alphandery et al, who showed that the presence of iron-chelating agents within the bacterial growth medium increases the magnetosome size and the chain length [131]. The Ch – Rhodamine B at the concentration of 4 μM leads to longer chains and up to 90 nm of the magnetosome size. Despite the usage of iron chelating agent, the size of magnetosomes and the length of magnetosome chains, obtained by Alphandery, were still lower than the size of magnetosomes and their amount per cell shown in this study. The pH also has a great impact on the size, number and morphology of the synthesized crystals. Moisescu et al. showed that already at pH 6, the morphology of crystals synthesized differed from those produced at pH 7 [132]. The magnetosomes synthesized at pH 6 were poorly developed and immature. Popa et al. studied the O_2-stress treatment and its influence on the formation of magnetosomes in AMB-1 cells [58]. The size of magnetosomes formed under the concentration of 45 μM of oxygen and shaking conditions, exhibited ~ 25 ± 4 nm with some particles as small as 10 nm. The size of magnetosomes produced under oxidized conditions, at ORP 0 mV, was the smallest observed but still bigger than reported by Popa et al. and increased to 31.5 ± 1.3 nm.

ORP influence on the cells morphology

The reason for enormously long cells, with fully evolved magnetosomes, at ORP – 500 mV remains unknown and further analyses are necessary. Nonetheless cells were motile and were responding to the magnet, what could be seen via optical observations. It was shown that younger cells were shorter than cultures reaching stationary phase [66] and increase in size from an ‘s’ shape to a long spiral occurred with increasing incubation time [65]. Control experiments showed standard dimensions, whereas the reason for such abnormal development in the other two testing conditions is unclear. It is speculated that bacteria become longer when in conditions of stress [65]. This would guarantee them benefits, such as higher surface/volume ratio for a better exchange of gasses and nutrients with the surrounding environment, or a better adhesion to a surface in order to shift to a sessile lifestyle [133]. The phenomenon in *Magnetospirillum* however still remains unknown. Katzmann et al. treated the cells with cephalexin, an antibiotic that inhibits the septation of bacteria, obtaining also very elongated cells [134]. The function of chemicals having such inhibitory functions as

cephalexin is rather unknown and further research is therefore needed in order to better understand this phenomenon.

ORP influence on the increasing yield of magnetosomes

Potassium ferricyanide acts as an oxidant. Studies done on *Streptomyces coelicolor* showed that when bacterium is limited for oxygen or treated with respiratory inhibitors, for example cyanide, the rapid induction of the cytochrome bd terminal oxidase operon occurs [135]. Tamegai et al. reported a cytochrome a_1-like hemoprotein that was present in higher amounts in magnetic cells grown microaerobically than non-magnetic cells [136] .Another protein, Mam T, is thought to be a cytochrome c heme-binding protein and may play a role in possible redox reactions involved in the magnetosomes synthesis. Titanium (III) citrate is a strong reducer but citrate itself has the unique ability to bind ferric iron. In bacteria, citric acid has been reported to act as an exogenous siderophores [137]. The ability to bind ferric iron leads to the formation of citrate correlated siderophores such as rhizoferrin and staphyloferrin A, where the structure of the chelating unit preserves the citric acid structure [138]. *Escherichia coli* possesses a specific transport system for ferric citrate [139]. *M. magneticum* have been reported to secrete siderophore 3,4-dihydroxybenzoic acid for Fe (III) complexation [140].

In previous studies with AMB-1, growth with nitrate has been reported to result in higher yields of magnetosomes [141], which was then increased by lowering the nitrate level in chemostat cultures by pH-stat feeding [142]. Y. Liu et al. (2010) suggested that Fe^{3+} can function as an electron acceptor under conditions where oxygen is absent and was likely transferred into cells as an electron acceptor for magnetosome biosynthesis to compensate oxygen insufficiency but in order to increase magnetosomes yields, cells preferred to use NO_3^-/NO_2^- couple as an electron acceptor [143]. Yang et al. showed that iron feeding rates above 15.4 µg / min resulted in rapid accumulation of 7. mg / L of bacterial magnetic partixcles [145]. Blakemore (1992) showed that the growth of *Aquaspirillum magnetotacticum* strain MS-1 and iron reduction were sensitive to variations in both E_h and partial pressure of O_2. MS-1 cell yields increased and Fe (III) reduction was stimulated by providing small amounts of air or H_2O_2 to cultures with suboptimal E_h (<0 mV) [144]. While great care was taken to exclude O_2 from the cultures, no attempts were made to optimize ORP. It is well known that oxygen typically serves as a terminal electron acceptor to generate ATP for living organisms. In the couple ½ O_2/H_2O with a reduction potential (*E0'*) of

+ 0.82 V, H_2O donates electrons, while O_2 accepts them. In this study the yield of magnetosomes was increased by changing the redox potential of the surrounding medium by using chemical components. At ORP 0 mV the magnetosomes formation is inhibited. In order to exclude the influence of atmospheric oxygen serving as an electron acceptor and influencing the overall redox potential, cells were grown anaerobically and the role of the terminal acceptor was dedicated to nitrite. By simple modification of redox potential in the surrounding medium, it was possible to increase the yield of magnetosomes and this would have a significant impact on the usage of these nanoparticles. Moreover, it was shown that the cells in the presence of oxidative stress triggered by oxidant other than oxygen, are not capable to produce magnetite nanoparticles.

ORP and its influence on the cellular iron concentration

The values of iron uptake appear to be in the same range as previous studies on *M.magneticum* AMB-1. In Table 3-5, a comparison with results obtained by Heyen & Schüler (2003) is shown. It exemplifies that at lower oxygen concentration (0.25 mbar partial pressure), there is a clear decrease in iron accumulation; iron content is 9.8 mg * g^{-1}g dry weight. It was shown under anaerobic conditions; where the oxygen partial pressure is 20 mbar, that the cell growth is reduced and in consequence the iron content is lower – 4.9 mg * g^{-1}g dry weight. The experiments performed under anaerobic and ORP -500 mV conditions show higher iron contents (12.8 mg * g^{-1}g dry weight) in the cell as expected only from anaerobic cultivation. At ORP 0 mV, what imitates oxidized conditions, results showed 7.4 mg * g^{-1}g dry weight what is lower compared to ORP – 500 mV, but still higher than was observed under aerobic conditions by Heyen & Schüler (2003). Looking at this comparison, the question of understanding the relationship between ORP and biomineralization arises. Is the decrease in iron accumulation connected to an increase of ORP?

Table 3-5 Iron content measurements reported for ORP conditions, normalized according to dry weight (left column). Iron content measurements reported by Heyen and Schüler (2003) for AMB-1 strain (right column) reported for different oxygen partial pressure.

ORP experiments		Heyen & Schüler (2003)	
ORP condition	**Iron content ($mg*g^{-1}$ dry weight)**	**Oxygen partial pressure (mbar)**	**Iron content ($mg*g^{-1}$ dry weight)**
-500 mV	12.8 (± 3.4)	0.25	9.8
Controls	11.4 (± 2.9)	2	7.9
0 mV	7.4 (± 1.9)	10	5.7

The iron content in the pellets at ORP 0 mV does not give the precise information due to the fact that iron residues, after centrifugation, remained on the cell surface. When the supernatant was discarded from the pellet, an amount of liquid was inevitably left in the tube (around 0.1 mL). This liquid, iron rich medium had a strong influence on the result of the experiment. At low cell densities, this variation in iron concentration may significantly influence the final result. However, when the cell density increases, this iron is divided among the cells and the effect becomes less visible. This fact does not change the general result that at ORP 0 mV the formation of magnetosomes is inhibited. Nevertheless, the chemical change of redox potential, especially at ORP 0 mV, needs to be complemented by comparing the effect of oxygen in the same bioreactor system on the formation of magnetosomes.

3.2. Phage biotemplated assembly of nanoparticles

The use of magnetic nanoparticles to activate hybrid structures is investigated in the second part of this thesis. Phages are used as a templating structure whereas magnetic nanoparticles are employed as functional carrier of the external magnetic field utilized for actuation. Four types of nanoparticles were tested for their binding properties to the template. Zeta potential measurements were respectively performed on particles and phages in order to find suitable conditions for an electrostatic binding.

3.2.1. Characterization of the individual components used as basis for the assembly

I envisioned different type of magnetic nanoparticles as a basis of the assembly. The particles were selected because of their expected differing surface properties. The nanoparticles were initially investigated using electron microscopy. The list encompasses magnetosomes isolated from *M. magneticum* AMB-1 strain, synthesized magnetite nanoparticles without additives, magnetite nanoparticles synthesized in the presence of poly-L-arginine and magnetite nanoparticles coated with positively charged polyethylenimine. As shown in SEM image (Figure 3.18 a) magnetosomes have a strong tendency to aggregate and form clusters. The magnetosomes aggregation is also shown in TEM image (Figure 3.18 b); the magnetosomes membrane surrounding magnetite crystal is also visible.

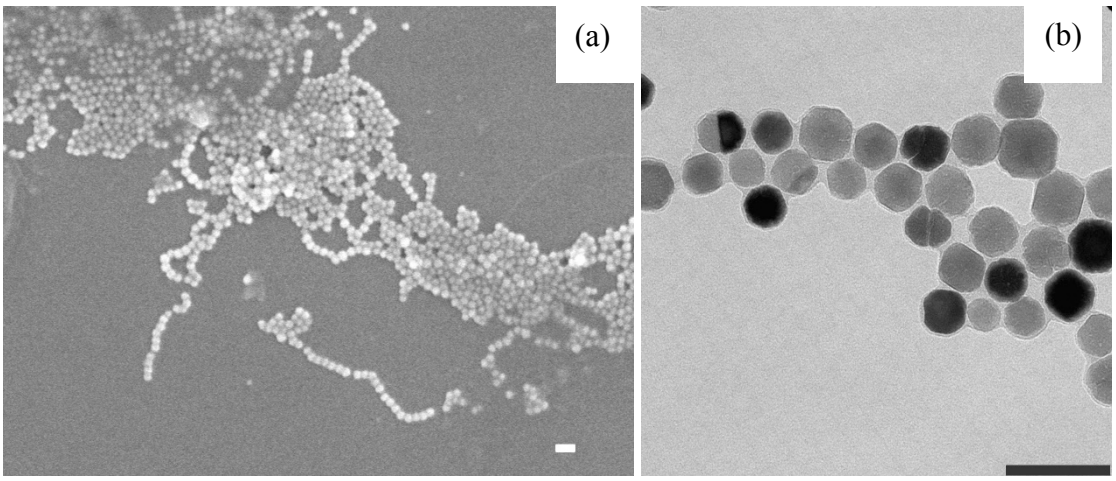

Figure 3.18 Characterization of magnetosomes by scanning (a) and transmission electron microscopy (b). The magnetosomes do not agglomerate thanks to the presence of the magnetosome membrane. Still, the particles interact magnetically so that they are in close proximity. Scale bars are 100nm.

Magnetite nanoparticles synthesized without any additives are shown in Figure 3.19 a. The pure magnetite nanoparticles tend to aggregate probably due to their magnetic attraction as well as the lack of organic (lipidic) membrane that ensure some steric hindrance. Magnetite nanoparticles synthesized in the presence of poly-L-arginine (PolyR) can be seen in Figure 3.19b. The typical behavior of PolyR nanoparticles is chain formation.

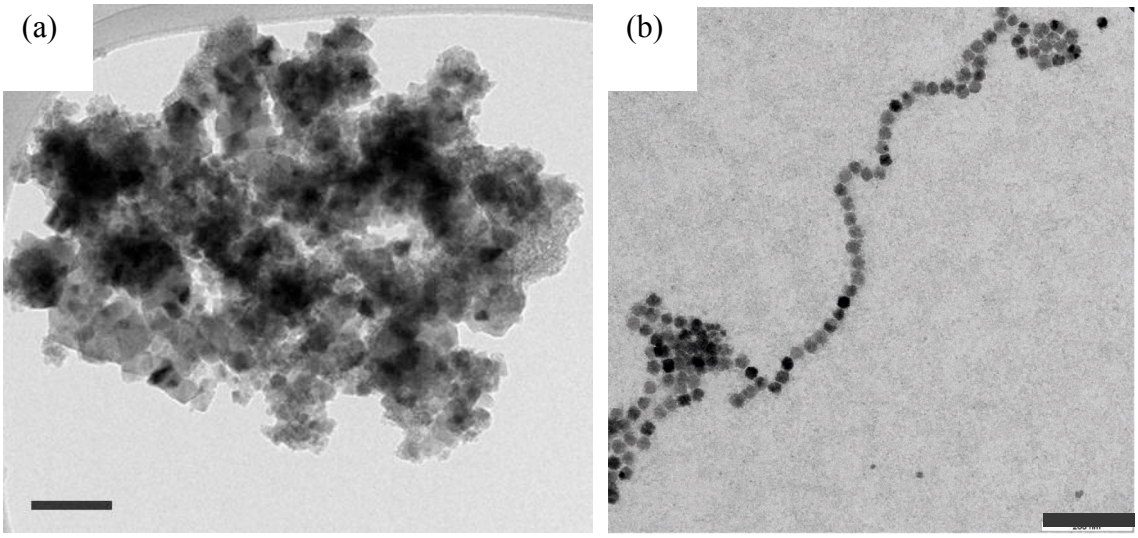

Figure 3.19 Transmission electron microscope images of magnetite (a) and polyR nanoparticles (b). Scale bars are 200 nm.

PEI nanoparticles (PEI NPs), tested for their zeta potential, are the best candidate to fulfill the requirements necessary for the deposition of nanoparticles on the phage filament. They remain positively charged within the pH of interest, which is neutral. They are dispersed, which can be observed in Figure 3.20 a. PEI NPs do not aggregate in comparison with tested magnetosomes or magnetite nanoparticles. They do not form chains either, which was observed in the case of PolyR nanoparticles. They provide the sufficient material in order to be deposited on the phage filaments. Therefore, the polyethylenimine was chosen as a linker between magnetite nanoparticles and phage filaments. The membrane formed by polyethylenimine can be seen in high resolution image shown in Figure 3.20 (see inset). Magnetic nanoparticles were prepared using iron oxide powder as the iron precursor, oleic acid as a ligand, and octadecene as the solvent which resulted in particles coated with amphiphilic polymers [146]. Positively charged polyethylenimine nanoparticles are stable within the range of pH from 5 to 10 of different buffer solutions as well as in water [147].

M13 phage has a filamentous structure what is shown in Figure 3.20 b. The phage solution was deposited onto the cooper grid and left to dry. Afterward the phages were stained with 2 % uranyl acetate in order to better see very thin phage filaments.

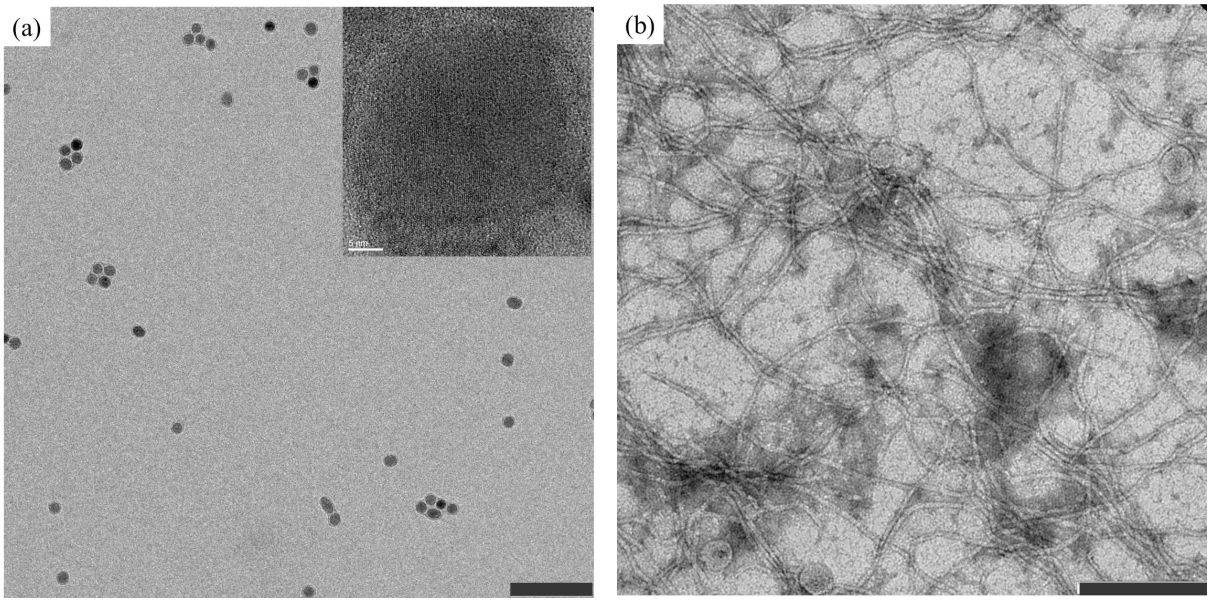

Figure 3.20 Transmission electron microscopy images of PEI nanoparticles (a), phages (b) Scale bars are 200nm (a, b). High resolution image of PEI nanoparticle (inlet) Scale bar is 5 nm.

3.2.2. Zeta potential properties of magnetic particles

The need of controlled organization of nanoparticles requires establishing basic principles of their properties in solution. In order to determine the surface charges of the nanoparticles and phages, zeta potential measurements were performed. The zeta potential measurements showed that the point of zero charge of magnetosomes is already passed at pH 5. In none of the tested conditions, from pH 5 to pH 10, the charge of magnetosomes was positive (see Figure 3.21). The zeta potential value of magnetosomes in solution at pH 5 was indeed -1.4 mV. With the pH increase up to pH 10, the charge decreases to -15 mV.

The second type of particles tested was magnetite nanoparticles synthesized without any additives. The zeta potential measurements showed that magnetite nanoparticles remain negatively charged within the whole range of tested pH, from pH 5 to pH 10. The charge of nanoparticles is even lower than measured for magnetosomes. At pH 5 the charge is -36 mV and slightly increases to -26 mV at pH 10.

The zeta potential measurements of magnetite nanoparticles synthesized in the presence of poly-L-arginine (PolyR) [81]showed that from pH 5 to 9, the particles are positively charged (see Figure 3.21). At pH 5, the overall charge of particles is 24 mV and it gradually decreases to 0 mV around pH 10.

The zeta potential measurements of the forth type of iron oxide nanoparticles surrounded by the layer of polyethyleneimine (PEI NPs) showed that in all of the tested conditions, from pH 5 to pH 10, the charge of the particles was positive. At pH 5, the charge was 20 mV, whereas at pH 10, it decreased to 2 mV. Moreover the zeta potential of PEI NPs was additionally measured when nanoparticles were dispersed in MilliQ-water and not only in the H_3BO_3 buffer. In this case the charge increased to 45 mV (see Figure 3.21).

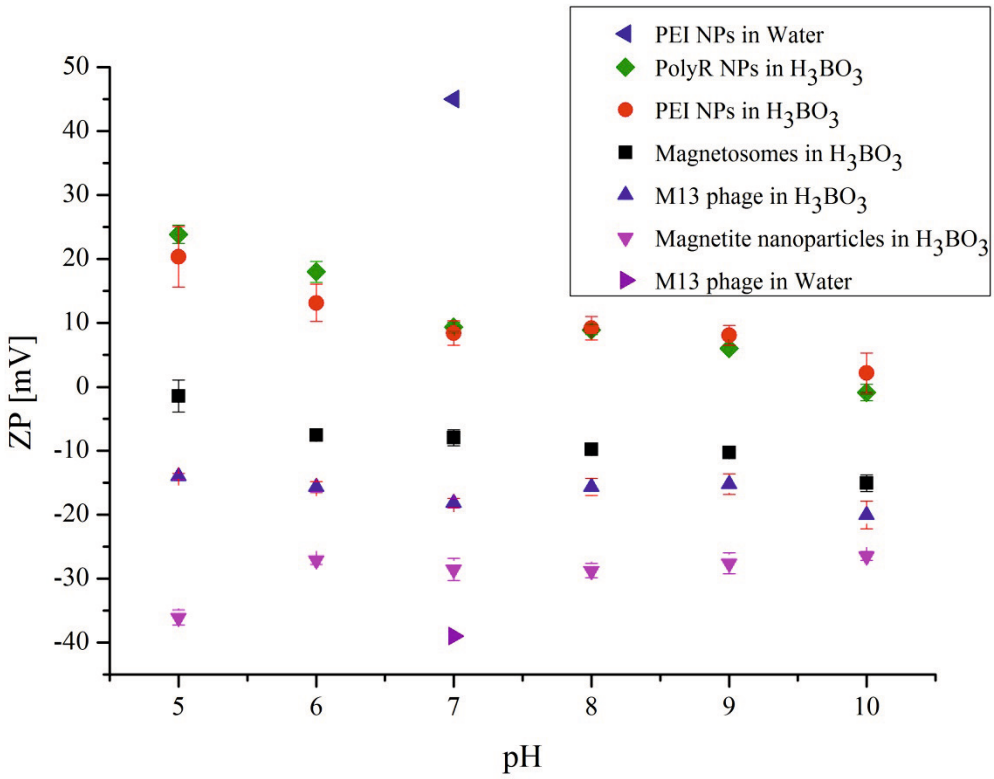

Figure 3.21 Zeta potential as a function of pH for PolyR, magnetosomes, and magnetie and PEI NPs and M13 phage filaments dispersed in borate buffer. PEI nanoparticles and phage filaments were additionally dispersed in MilliQ-water and the zeta potential measurements were performed.

The zeta potential measurements were performed on phage filaments as well to test the other end of the structure. The results showed that in the borate buffer, the phages were negatively charged from pH 5 to pH 10. The zeta potential remained similar within the whole pH range tested and was ca. -15 mV. The zeta potential decreased even more, to the value of - 39 mV, when phage particles were dispersed in MilliQ-water.

The zeta-potential measurements performed above open up the possibility of using electrostatic interactions to bind magnetic nanoparticles on filamentous phages. The highest difference recorded was obtained for phages and PEI NPs suspended in MilliQ-water. This result highlights the importance of the ionic strength and its influence on the behavior of particles in solution. The measured values are not surprising due on the one end to the properties of PEI (a highly positive polymer [82]) and to the other end to the most abundant phage coat protein, pVIII, which is very rich in acidic residues [148]. I therefore chose these constituents and these conditions to form the magnetic nanostructures.

Dynamic light scattering was performed on phage samples before and after binding to PEI NPs. The Z-average (hydrodynamic diameter) that was obtained for molecules is given in the Table 3-6. The hydrodynamic diameter of PEI NPs in MilliQ-water was 88.7 nm. Phage filaments had the hydrodynamic diameter of 469.3 nm. When PEI NPs mixed with phage nanoparticles, the hydrodynamic diameter increased to 1888.0 nm.

Table 3-6 Hydrodynamic diameter (Z-average) of PEI NPs, M13 molecules determined by DLS.

Samples	Z-average (d/nm)
Pure PEI NPs	88.7 (± 13.9)
Pure M13	469.3 (± 48.0)
NPs and M13	1888.0 (± 453.0)

3.2.3. Towards magnetic string

Knowing what type of particle was positively charged, I subsequently incubated the PEI-magnetite nanoparticles with the phage filament. The solution containing PEI nanoparticles was mixed with phage solution at a ratio of 2:1. The mixture was incubated for 5 min and then 20 µl was placed onto a cooper grid and investigated via TEM. In order to better see phage filament, the sample was stained with 2 % uranyl acetate. In Figure 3.22 a and b, examples of phage nanoparticle assembly are shown. It can be observed that PEI nanoparticles tend to assemble along phage filament.

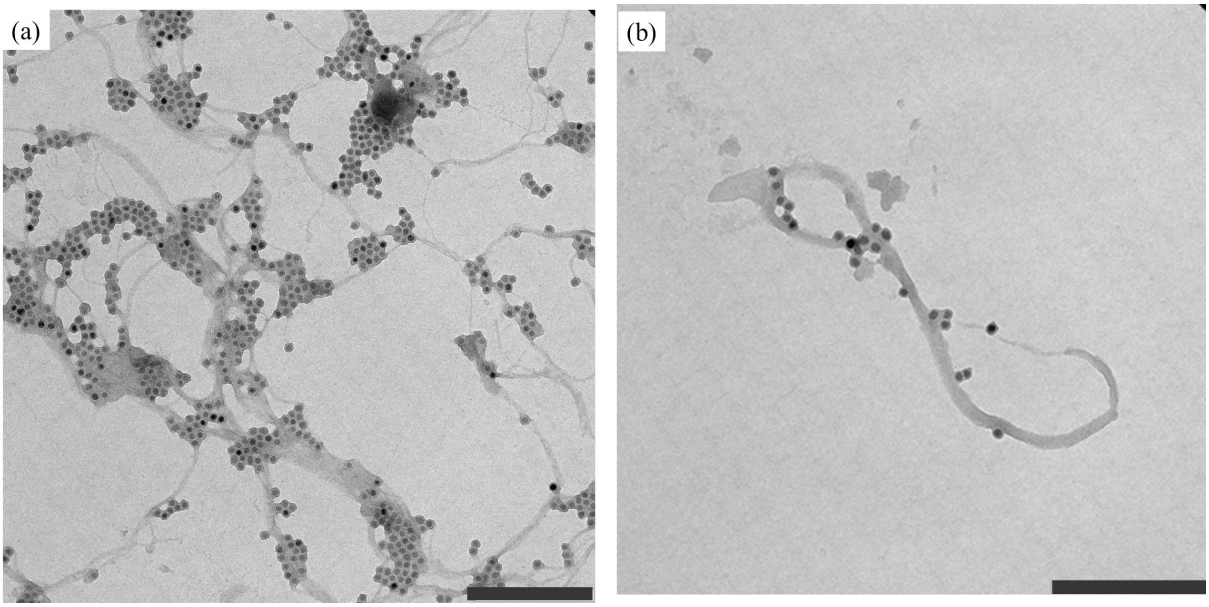

Figure 3.22 Transmission electron images of PEI nanoparticles – phage assembly. Nanoparticles and phages were mixed in the ratio 2:1 and incubated 5 min in water. The mixture was placed onto the cooper grid and stained with 2 % uranyl acetate. Scale bars: 500 nm

Topography measurements of phage – nanoparticle assembly

Isolated phages were as well as nanoparticles adsorbed to a negative substrate – a silicone oxide substrate and imaged by AFM. Phage filaments deposited on the substrate are shown in Figure 3.23 (panel a), PEI NPs in Figure 3.23 (panel b), and multivalent assembly of PEI NPs on single phage filament in Figure 3.23 (panel c). Since the size of both particles (30 nm) and phages (6 nm in diameter) is known, it is possible to fit height of the profiles with appropriated values. In Figure 3.23 (panel d), the height profiles of both particles and phages are presented. As shown in Figure 3.23 b, the PEI NPs, when adsorbed on the silicon oxide

surface but in the absence of any phage template, exhibit high density aggregates without any defined pattern. Due to electrostatic interactions between positively charged PEI nanoparticles and negatively charged phage filaments, PEI nanoparticles bind to the phage filaments forming a chain like organized structure, as shown in Figure 3.23 c. The phage filament is only 6 nm wide, which is hardly seen in Figure 3.23 c. Therefore, in order to confirm that the particles are attached to the phage filament, the height profiles of phage filament and PEI nanoparticles are shown in Figure 3.23 d. Profile 1 and Profile 3, shown in Figure 3.25 c, correspond to height profiles of two PEI nanoparticles, shown as solid grey line (Profile 1) and dashed line (Profile 3) (Figure 3.23 d). The height of PEI nanoparticles is around 35 nm, which fits the size of particles. Consequently, height profiles of phage filament were analyzed. Profile 2 and profile 4, shown in Figure 3.23 a, have their equivalent values in Figure 3.23 d; dotted line corresponds to Profile 2 and black solid line to Profile 4 respectively. The heights of filaments are 6 nm, what also confirms the size of phage filament. Thus, it can be confirmed that PEI nanoparticles are attached to phage filament and organized in chain like structures.

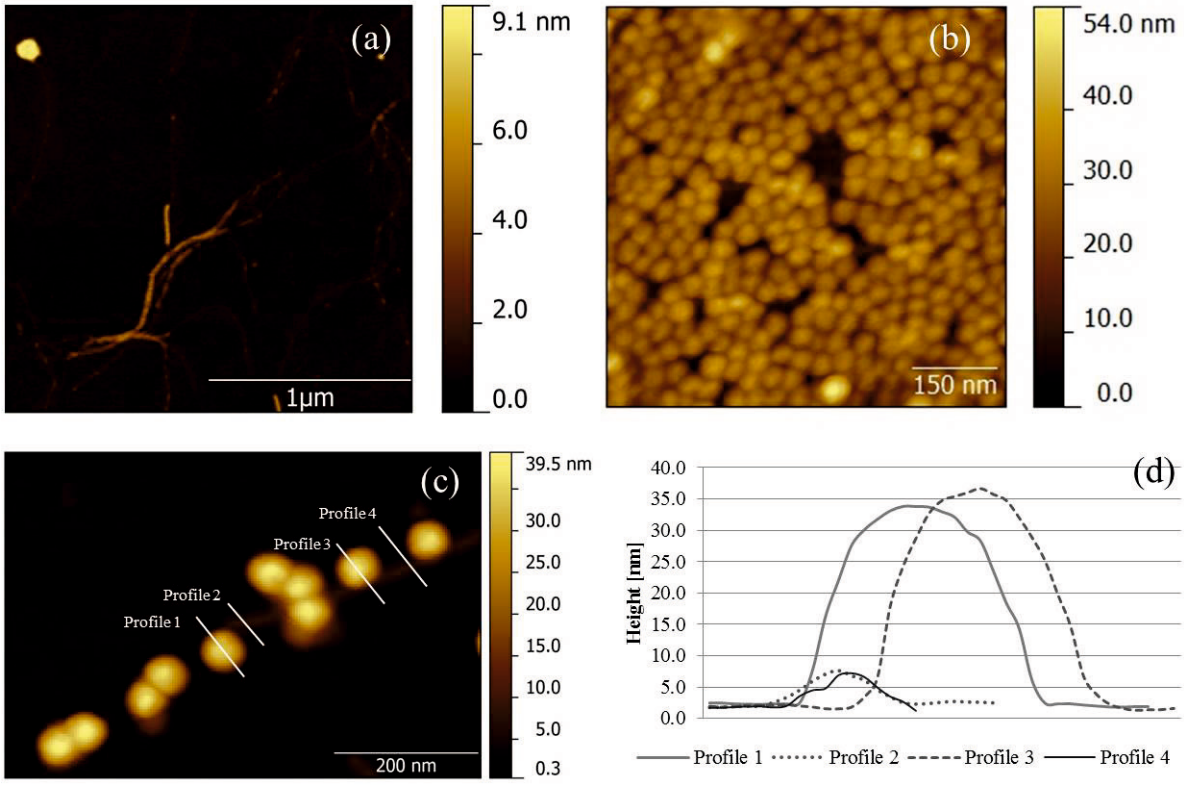

Figure 3.23 AFM images of phages (a), PEI NPs (b) and PEI NPs attached to the phage filament (c) are shown. Panel (d) shows height profiles of phage filament and PEI NPs presented in image (c). Scale bars are: Panel (a) 1 µm, Panel (b) 150 nm, Panel (c) 200 nm.

3.2.4. Magnetic actuation of phage – nanoparticles assembly

In order to evaluate the potential use of phage – nanoparticles assemblies as magnetically actuated flexible nanoparticle chains, experiments with nanoparticle - phage assemblies were performed, by actuating the assembly with rotating magnetic fields. The example of such an assembly is shown in Figure 3.24.

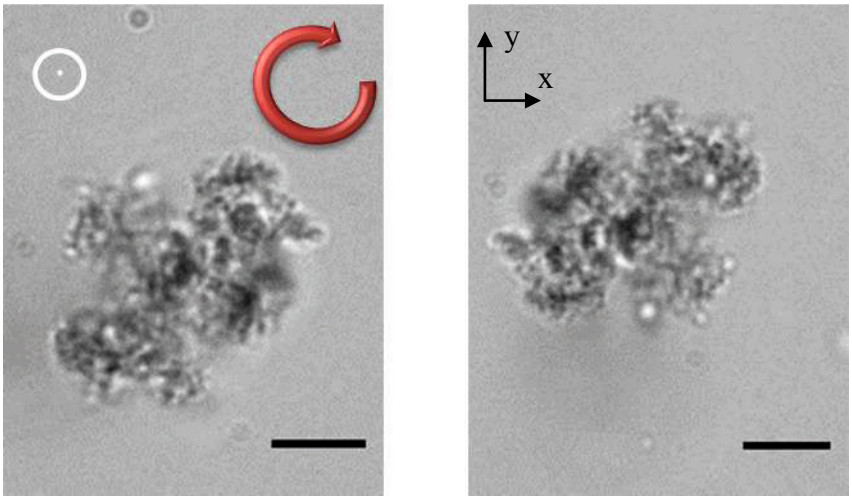

Figure 3.24 Image of the phage – nanoparticle assembly rotating in the magnetic field. The red arrow indicates rotating movement of the assembly in the plane. White sign indicates the vector of the magnetic field (right hand rule). The experiments were performed at 1 mT, frequency 20 Hz. Scale bar 10 µm.

The swimming motion can be achieved by actuating flexible structures with a magnetic field that would be induced by applying both alternating and direct current [149]. Then the propeller would move approximately parallel to the vector of z direction, in this case swimming upwards.

Propelling behavior of random phage-nanoparticle assemblies

It is possible to use the assembly of phage and PEI NPs as propellers, by actuating the aggregates with rotating magnetic field as shown above. The propellers move approximately parallel to the vector of rotation of the magnetic field. It was observed as well that the phage – nanoparticle assembly is flexible; therefore, deviations from a straight line are apparent not only due to the diffusion but also due to the change in shape of the assembly. The average speed was measured as in the range between 0.5 - 1 µm × s^{-1}, when actuating structures at

20 Hz. The structures had an average size around 15 μm (see Figure 3.24) and were used without size selection.

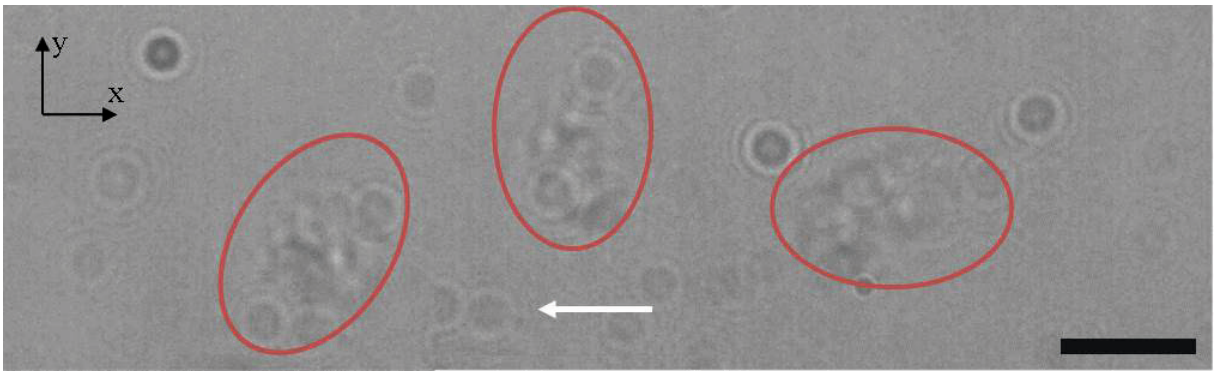

Figure 3.25 Time-lapse image of the propulsion movement. The phage-nanoparticle assembly is rotating in the bulk liquid by a rotating magnetic field. The images are overlaid in 0.28 s intervals. Images are extracted from a video recorded at 50 fps. The white arrows indicate the direction of the motion of the phage-nanoparticle assembly Scale bar is 10 μm.

Time lapse experiment

The mixture of phage filaments and PEI nanoparticles was placed at the bottom of a vial, filled with 600 μL of MilliQ-water. In order to perform the time lapse experiment, it was necessary to collect samples from more than one vial. Therefore 15 vials were placed at the same time between the Helmholtz coils of the magnetic setup described in section 1.1. The coils were producing alternating and direct currents simultaneously. The magnetic field strength produced at the frequency of 20 Hz was 1.4 mT. The samples were collected immediately after placing the vials in the magnetic fields and every two subsequent hours. Phage-nanoparticles assemblies were collected from the top of the capillary. Since the height of the capillary is 1.5 cm and the time when the first structures were collected is 10 hours, it was possible to calculate the propelling speed, which is 0.4 μm sec^{-1}.

Then samples were analyzed by TEM in order to characterize the phage-nanoparticle assembly. TEM images of phage-nanoparticles assemblies collected after 10 hours are shown in Figure 3.26a, b. Figure 3.26 c, d represents the phage-nanoparticle assemblies observed after 20 hours of the experiment.

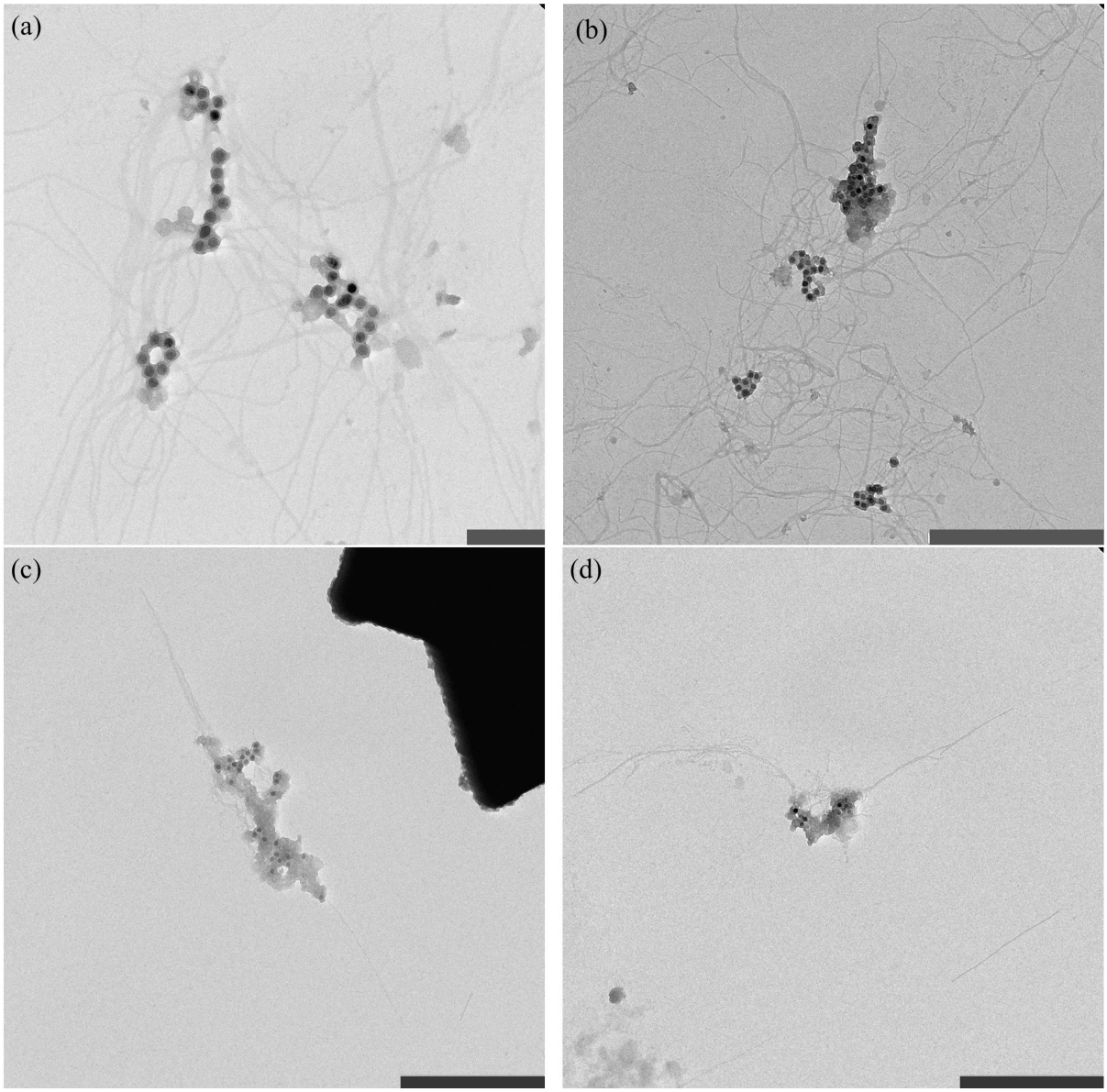

Figure 3.26 Transmission electron microscopy images of collected phage-nanoparticles assemblies. Image (a) and (b) represent phage-nanoparticles assemblies collected after 10 hours of the experiment. Figure (c) and (d) show the phage-nanoparticle assemblies collected after 20 hours of the experiment.

In general, the amount of nanoparticles attached to phages is broadly distributed and is ranging from 2 to more than 500 nanoparticles (see Figure 3.27). The size of the selected assemblies depends on the time when the assembly was collected (Figure 3.27). After 10 hours, the total amount of particles observed per assembly differed from 18 to more than 500 (see Figure 3.27). After 20 hours of the experiment the total amount of nanoparticles decreased. As shown in Figure 3.27, the phage – nanoparticles assemblies possessed from 1 to 18 nanoparticles.

The graphs shown in Figure 3.27 demonstrate the amount of particles in total, in the whole observed assembly, and the amount of particles normalized per µm and surface area of µm^2. The results are shown and as the minimum and the maximum values, described by error bars and the median is included.

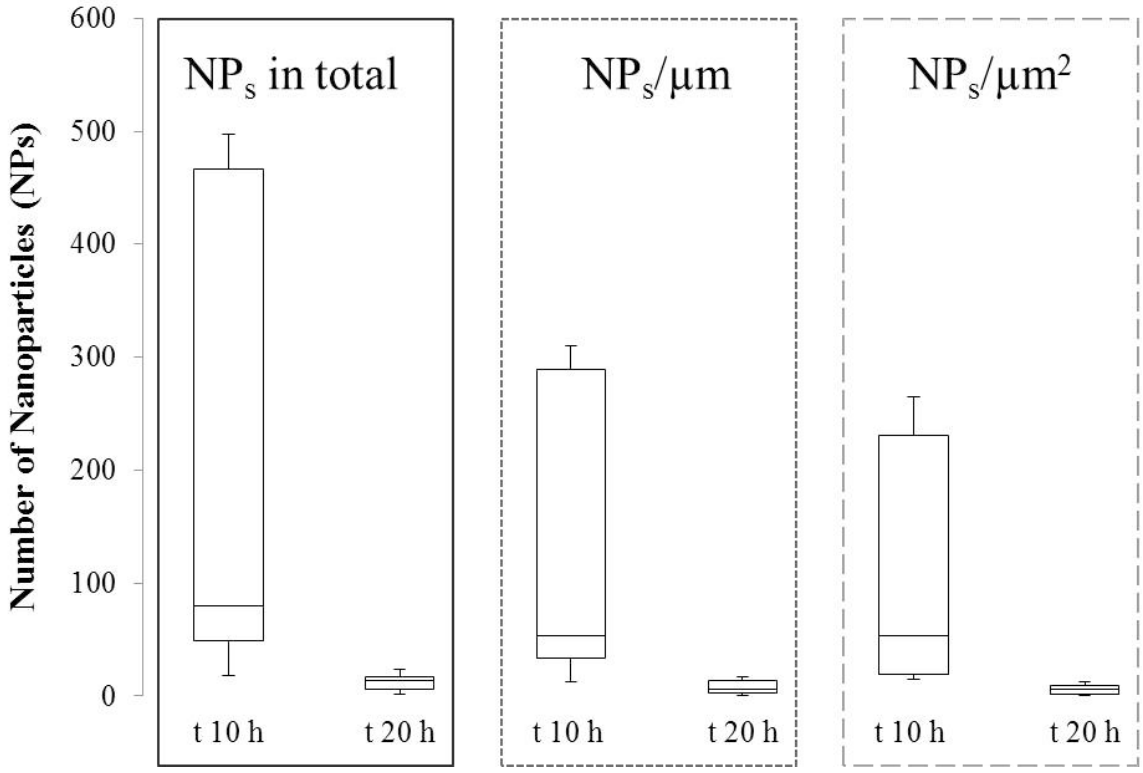

Figure 3.27 Number of PEI nanoparticles attached to the phage filaments shown as a total number of nanoparticles per observed assembly (left box), the amount of nanoparticles per length (middle box) and the amount of particles per surface area of µm^2 (right box). The results are presented for two time points: after 10 hours (t 10) and after 20 hours (t 20).

In Figure 3.26 a, the assembly is formed by 46 nanoparticles and the surface area of the whole assembly is 8.2 µm^2. Images (c) and (d) represent the 20-hour time point. The amount of nanoparticles in image (c) is 28 and they occur at the surface of ca. 6 µm^2. In comparison the amount of nanoparticles in image (d) is only 9 and the square area of the phage-nanoparticles assembly is 2.5 µm^2.

3.2.5. Functionalization of phage filaments

The small size of the phage requires the improvement of the techniques necessary to detect them especially when the filaments are actuated and tracked in the external magnetic field. The surface of the phage filament could be exploited by fluorescently labeling p8 protein of the phage. This most abundant protein of the phage capsid is representing 99 % of total virus surface. In the wild type phage, amino groups in N-terminal alanine and in lysine (Lys8) and carboxylic acid groups in glutamic acid (Glu2) and aspartic acid (Asp4 and Asp5) on pVIII protein are viable targets for selective chemical functionalization [148]. In Figure 3.28 it is possible to see the phage filaments, labeled via fluorescent staining, being rotated in the magnetic field. The rotation occurs thanks to PEI NPs, attached to the filaments and their response to magnetic fields. When the magnetic field is switched of, the assembly falls out of focus and the fluorescence disappears. The labeling of the phage filaments expands the type of techniques that enable tracking these nanostructures.

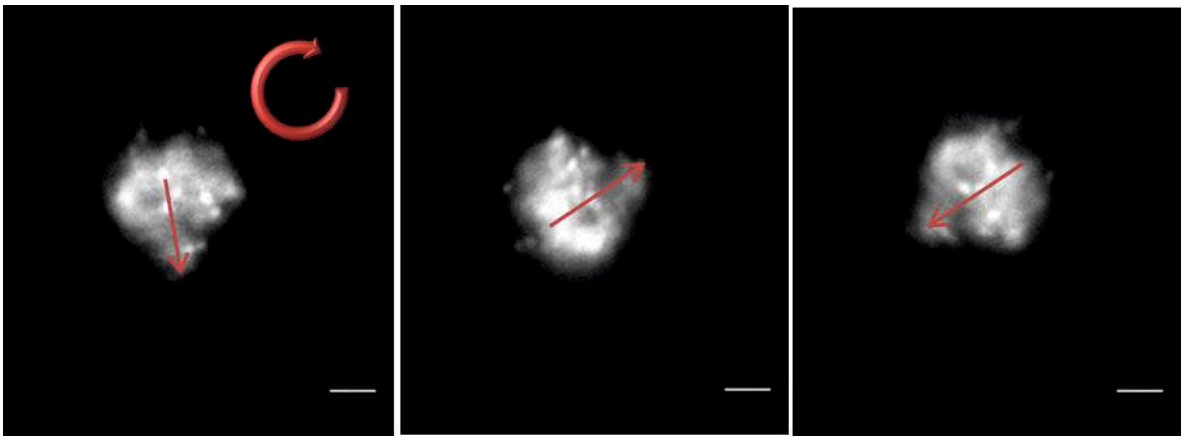

Figure 3.28 Fluorescence image of labeled phage filaments actuated in the magnetic field due to PEI NPs binding to their surface. Assembly is actuated by a magnetic field of 1.4 mT rotating at 30 Hz. Scale bar: 5 µm

3.2.6. Towards sperm-like assemblies

The phage-nanoparticle assembly was studied from a second perspective. Here, I tried to design a flagellum-like construct able to swim in an external magnetic field. In order to fulfill this task, genetic modifications of phage filaments and magnetosomes were performed in

order to covalently bind nanoparticles and phages. The as-such designed hybrids consist of two parts: a tail – a phage, displaying mCherry protein on pIII protein of the phage capsid and a magnetic head – a magnetosome, isolated from a genetically modified strain of the magnetotactic bacterium *M. gryphiswaldense*. The magnetosome membrane protein, MamC, has a fusion of RFP binding nanobody, and comprises a linker to the magnetosome and mCherry phage.

The nanoassemblies of RBP-magnetosomes and mCherry phages were investigated using electron microscopy. A magnetosome, magnetite core surrounded by a protein shell as well as filamentous phage is visible on the TEM images (Figure 3.29). Some of the magnetosomes are still organized in chain like structures. In order to avoid their aggregation, the solution containing magnetosomes was sonicated before they it was used for experiments. Chain like-structures appear only on the level of a few nanoparticles, most probably due to their magnetic interactions between nanoparticles.

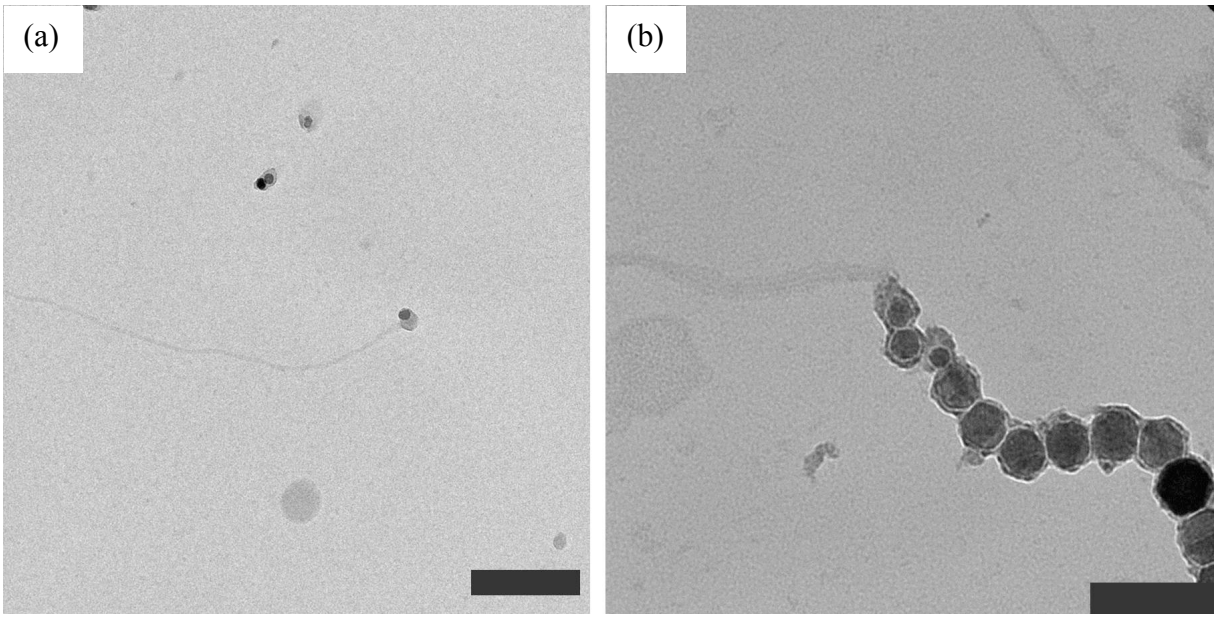

Figure 3.29 Transmission electron microscopy images of mCherry phages attached to RBP magnetosomes. Scale bars: image (a) 200nm, image (b) 100 nm.

Energy-dispersive X-ray Spectroscopy

The elemental composition of RBP magnetosomes was investigated using energy-dispersive x-ray spectroscopy (EDX). The results are displayed in Figure 3.30. As expected, the RBP–magnetosomes contain iron and oxygen. This is consistent with biomineralized

magnetosomes, containing magnetite crystals. The intense copper peak observed in the EDX spectra originate from the cooper grid which is used as substrate to deposit the sample for analysis.

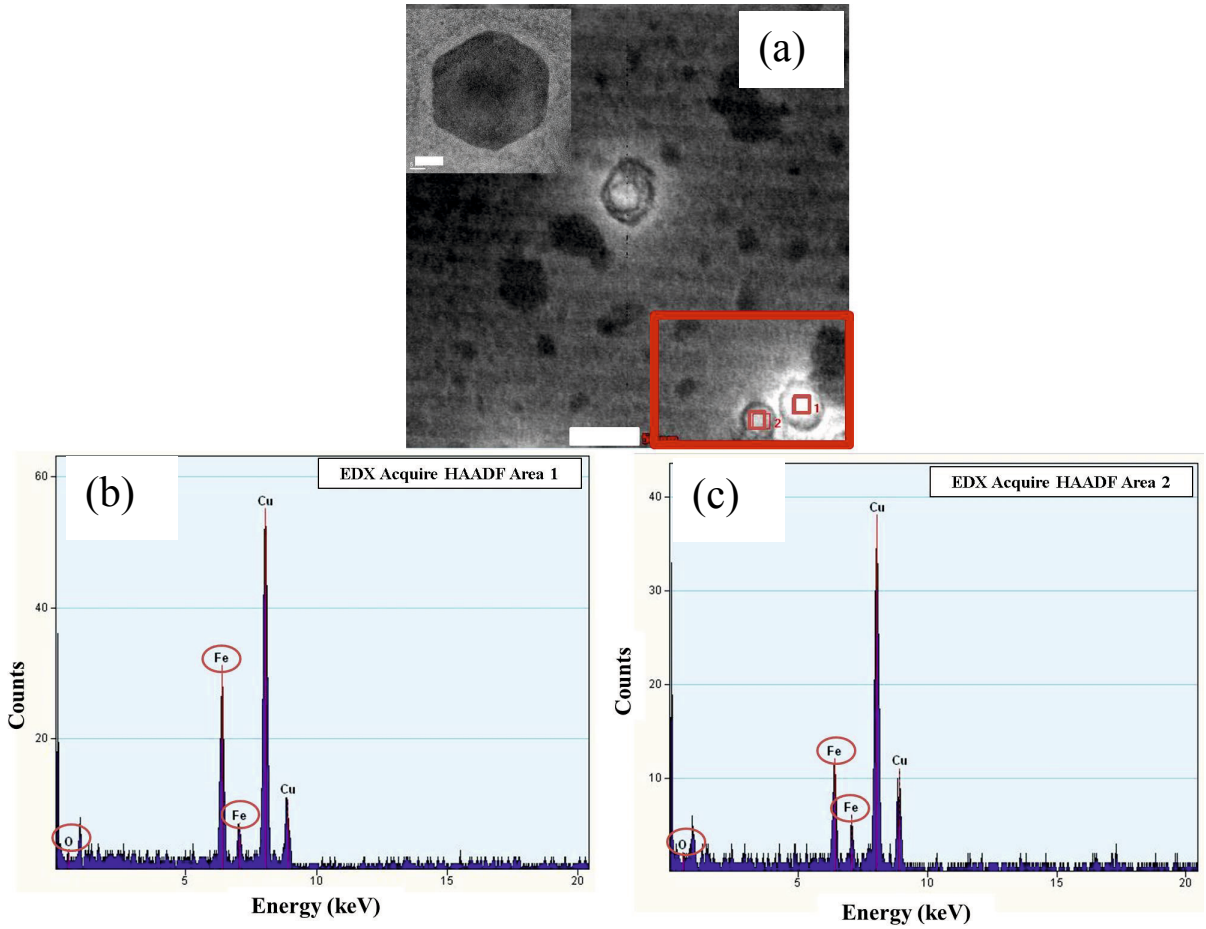

Figure 3.30 Transmission electron micrograph of RBP magnetosomes. The red big square represents the scanned area and the two small numbered squares represent the ares where the EDX was performed on the RBP magnetosomes. The scale bar is 50 nm. (b and c) EDX spectrum of the marked areas. Inset represents HRTEM image of the RBP magnetosome signed with the square nr 1, located on the right sight. Scale bar is 5 nm.

Magnetic actuation of fluorescent RBP-magnetosomes – mCherry phage assembly

The size of the single sperm-like structure obtained by attaching the mCherry phage to the MamC-RBP magnetosomes does not allow imaging its movement in the magnetic field by available optical techniques (see Figure 2.13). Fluorescence microscopy would constitute an alternative method to track the swimmers. mCherry protein comprises a link between phage

tail and RBP-magnetosome. The mCherry protein is excited at 561 nm and emitted between 570 nm and 640 nm. However, it may undergo quenching, due to the presence of oxygen in RBP-magnetosome magnetite; and in the consequence lose its signal. It was possible to detect the mCherry phages using confocal microscope but additionally the phages were stained with carboxyfluorescein succinimidyl ester and imaged in a confocal microscope and two fluorescence intensity images, a transmission image and a fluorescence lifetime image were recorded. In order to stain mCherry phages with another dye, the solution with the concentration of phages of 2.9 x 10^{12} was incubated with the carboxyfluorescein succinimidyl ester, which resulted in having mCherry phage particles being able to be detected with the help of another, a green fluorophore. Figure 3.31 shows images of mCherry phages (Figure 3.31 a) and mCherry phages stained with green fluorophore (Figure 3.31 b). The images present different imaging parameters. The first image (red channel) is recorded with excitation at 561 nm and emission between 570 nm and 640 nm corresponding to the fluorescence emission of mCherry protein; the second image (green channel) is recorded with excitation at 488 nm and emission between 500 and 550 nm corresponding to the fluorescence emission of green fluorophore.

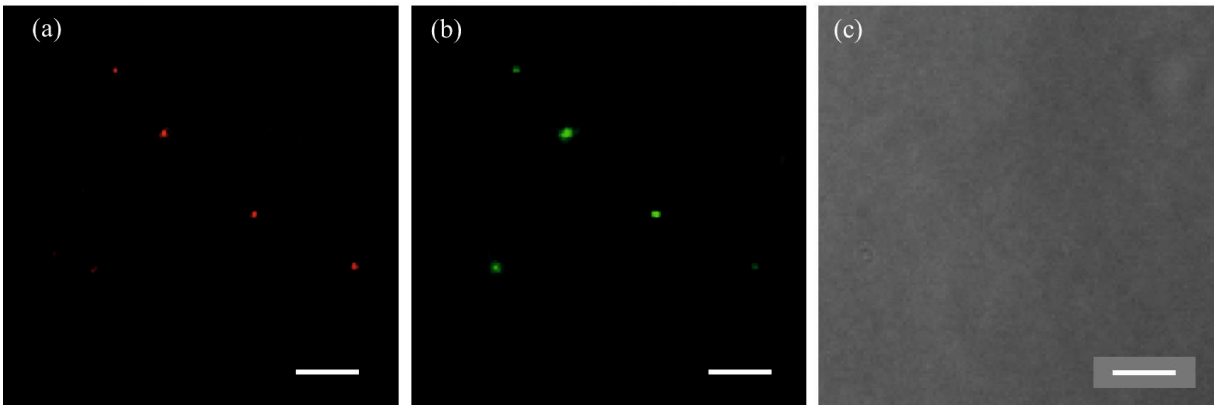

Figure 3.31 Fluorescence images of mCherry phages. Fluorescence intensity images were recorded at a confocal microscope with excitation wavelength at 561 nm and emission wavelength between 570 nm to 640 nm, corresponding to the fluorescence emission of the mCherry protein. Image (a) shows the mCherry phages. Image (b) shows mCherry phage stained with carboxyfluorescein succinimidyl ester. Image (c) is the transmission image. Scale bars are 5 µm.

The sample was embedded in 1 % agarose in order to immobilize the phages during the measurement; the third image is the transmission image of the sample. mCherry phage aggregates can be observed in Figure 3.31 a. The same aggregates but stained with a green

dye can be seen in Figure 3.31 b. The transmission image shown in Figure 3.31 c does not show any aggregates. The phages can be only detected by using fluorescence microscopy.

The assembly of mCherry phages and RBP-magnetosomes makes studying the magnetic actuation of this hybrid material very promising. It is possible to use these nanostructures as potential swimmers, by actuating the aggregates with magnetic fields. In Figure 3.32, the images: (a), (b) are examples of the assemlbly of phages and RBP-MamC magnetosomes being actuated in the magnetic field of 1 mT with the orientation indicated by white arrows, at the frequency of 20 Hz. When the magnetic field is switched off, the elongated structure collapses (shown in image c).

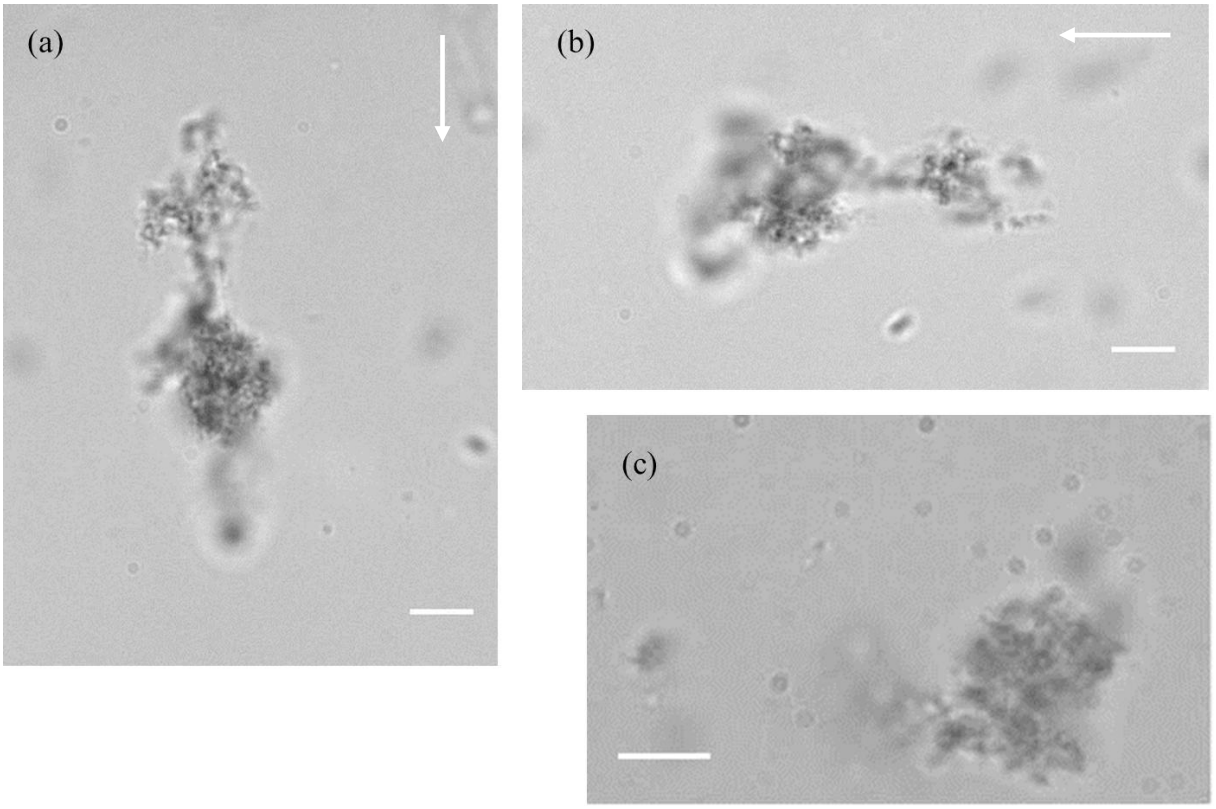

Figure 3.32 Chain of magnetosomes expressing MamC-RBP. An alterating magnetic field of 1 mT was applied, at the frequency of 20 Hz. Image (a) shows vertical position of the chain and image (b) is indicating its horizontal alignment in the magnetic field. Image (c) shows the collapse of the alignment due to the switch off of the magnetic field. The white arrows indicate the field direction. Scale bars are 10 µm.

3.2.7. Discussion

Phage-nanoparticles assembly and their chain-like structure

The chain-like assemblies are very flexible due to the phage filament used as a scaffold. Besides for magnetic actuation, phage – nanoparticle assembly is of bigger interest in many aspects. C. Mao et al. constructed a virus base toolkit for the directed synthesis of magnetic and semiconducting nanowires[150]. Gosh et al. used M13 – templated magnetic nanoparticles in targeted *in vivo* imaging by assembling iron oxide magnetic nanoparticles along M13 coat protein, which its distal end displays a peptide overexpressed in cancer cells [1]. Dreyfus et al. showed that it is possible to construct chain of magnetic nanoparticles linked by DNA and attached to a red blood cell, which can act as an artificial flagellum [91]. The method of constructing chain of PEI magnetite nanoparticles attached to the phage filament proposed in this thesis is simple and shows that by utilizing electrostatic interaction between nanoparticle and phage tail, it is still possible to actuate phage – nanoparticle assemblies in external magnetic fields. Potentially it could be used as a drag carrier as well. The electrostatic binding between nanoparticles and phage filaments was based on the charge differences of these molecules. By optimizing the conditions, in particular the pH of the suspension buffer, it was possible to create suitable conditions for stable electrostatic attraction. Magnetosomes isolated from *M. magneticum*, PolyR nanoparticles magnetite nanoparticles could not be utilized due to their negative charges at physiological conditions and the tendency to aggregate. Working at lower pH values would lead though to molecule dissolve, reducing the stability of the assembly. Charges of PolyR nanoparticles remain positive at the physiological conditions, but their aggregation and chain like formation disabled further experiments. The aggregate structure of magnetite nanoparticles has been described as spherical or chain like [151]. Chain like structure is attributed to magnetic interactions between iron oxide nanoparticles. Townsend et al. showed that the behavior of chains formed by ferromagnetic Ni nanoparticles was related to an increase in the magnetic field strength that facilitates the kinetics of chain like formation [100]. PEI NPs were dispersed; they did not show the tendency to aggregate. The difference in zeta potential values between PEI NPs and phages at pH 7 was higher than 30 mV, which is high enough to form stable electrostatic interaction between molecules. The ability to functionalize the phage – nanoparticle assembly by fluorescent labeling is important for detection of these structure, their control and potential applications and can be used for example to package and organize

large functional molecules [152]. Due to the magnetic properties of PEI nanoparticles it was possible to actuate phage – nanoparticle assemblies by using external magnetic fields. This would allow the assembly into organized superstructures of highly controlled movement, which makes studying the actuation of such a material even more promising. The movement of phage-nanoparticle assembly was studied in two ways. Firstly, the mixture of nanoparticles and phages was placed in a small capillary. By applying the alternating and direct currents simultaneously, the assembly was rotating and at the same time propelling in to the desired direction. The observed assemblies were relatively slow, when compared to the propellers so far reported. For example, the speed of the assembly of PEI nanoparticles and phages shown in Figure 3.25, moving along x axis, was 0.3 μm × sec^{-1}. The assembly was around 25 μm long. When compared to other propellers reported, it was much slower. For instance the faster random shaped propeller reported by Vach et al. was 1.22 μm long and was moving with the speed of 2.7 μm s^{-1} [153]. In order to improve the propelling speed, the size of phage – nanoparticles assemblies was selected by inserting the phage-nanoparticle solution into the cylinder and forced to swim against gravity. This allowed the selection of smaller and therefore faster phage – nanoparticle assemblies. Moreover, it is necessary to systematize the amount of particles attached to the phage filament. Preliminary quantitative methods have been presented but it still requires further analysis.

Phage-nanoparticle assembly into sperm-like structures

The second type of phage – nanoparticle assembly let to constructing potential sperm – like swimmer. It was indeed challenging to control the movement of this hybrid in the magnetic field due to its size. But it was shown (see Figure 3.29) that it is possible to select these hybrids by magnetic actuation. So far it is challenging to predict the speeds of such an assembly, therefore the techniques, which could improve the tracking nanometer size structures, are necessary. Potentially it would be necessary to improve the yield of phages displaying mCherry protein, since compared to WT phage amplification, it is still very low. This could improve the visualization techniques and enable phage-nanoparticle tracking. Roper et al. studied the improvement of micro-swimmer by modeling the movement of magnetic filament [6]. He focused though on the stiffness of the tail. MamC-RBP phage comprises new model to study with flexible chain and the magnetic head. But not only the motion is important is designing such structures. Potentially it is possible to use other coat

proteins in order to display peptides for biomedical applications. For example Hagen et al. successfully studied virus directed enzyme prodrug therapy [154].

Transition to sub-micrometer dimensions creates the challenges associated with fabrication and control of autonomous systems. Biological mobile nanoscale systems use similar operation modes as their engineered analogues. Viruses are perhaps the most commonly occurring untethered mobile biological nanosystems [19]. Therefore, the ongoing research in small-scale robotics gives them a big chance to rise. For the most part, biology is still far ahead of small-scale robotics in terms of autonomy and task capabilities [19]. It is not evident that this propulsion speed is equivalent to the propulsion speed in the bulk liquid, far from the surface. It is not clear either how fast are the propellers collected via their selection due to their very small size and consequently difficulties in visualization. Nevertheless, they start the new area of nano - science.

4. Conclusions and Outlook

Biologically controlled mineralization in MTB was mostly focused on the influence of pH and pO_2 on the formation of magnetosomes. Besides the genetic control, it was shown that the morphology of magnetosomes is strongly related to the chemical and physical conditions; apart from pH and pO_2, iron supply, temperature, chemical impurities were investigated. Although it is well known that MTB live in a redox active environment, the redox conditions were usually ignored. But this factor indeed has a strong influence on the process of the magnetite synthesis in *M. magneticum* AMB-1 strain. Generally, ORP is determined by a ratio of oxidative to reductive substances within fermentation systems [60]. Intracellular ORP homeostasis is fundamental for intracellular metabolism; many biological functions of cells are affected by ORP levels through gene expression [155] and enzyme synthesis, which consequently affect signal sensing and transduction, and metabolic profiles [156]. In this work a controlled cultivation in the bioreactor of AMB-1 strain was developed and the formation of magnetosomes characterized, which allows the study of redox potential influence on the biomineralization process occurring in one of MTB species.

By comparison of iron uptake rates, the morphology of bacteria, size and amount of magnetosomes per cell at different ORP, the potential ORP conditions within the growth of bacteria were inferred (ORP – 500 mV). At low Eh, the inorganic synthesis of magnetite at neutral pH is known to be thermodynamically favored [157]. Hence, it appears likely that the development of ORP conditions directly affects the physiochemical conditions in the interior of magnetosome vehicles. Magnetite formation was coupled to an increase in iron uptake under reduced conditions, whereas the iron content of cells grown under ORP 0 mV was similar to that reported for cells grown under aerobic conditions [57]. It was shown that ORP change in the bioreactor is not limiting for cell growth but it is crucial for magnetite formation; the formation of nanoparticles was inhibited at 0 mV. Not surprisingly, temperature and pH conditions are affecting the viability and the physiology of MTB and in consequence the ability to control the magnetite biomineralization [39]. However, this is the first study describing the influence of extracellular ORP and its influence on the formation of magnetosomes. Chemicals with different degrees of reduction such as, methyl viologen and neutral red are redox reagents, which can be supplemented into fermentation systems as electron carries, affect environmental ORP and intracellular metabolism [158][159]. On the other hand, cysteine/cysteine, oxidized/reduced glutathione and $NADH/NAD^+$ are major biological redox pairs that affect ORP. Special bioreactor configurations require to high

biochemical reagents concentrations and it is too costly to be used. Considering the required quantities of the chemicals used in this study, there were no objections to the usage of titanium (III) citrate as the reducer and potassium ferricyanide as an oxidant.

The work described in this dissertation aimed to gain a deeper understanding of the influence in the formation of magnetosomes in magnetotactic bacteria. The work was in particular focused on the study of magnetosome formation in *M.*magneticum AMB-1 strain. Magnetotactic bacteria, including AMB-1 were already known to be sensitive to variations of redox potential. All the previous studies were performed with oxygen as an oxidizer. This is the first study that analyzes the effect of oxidation stress on MTB utilizing chemical species other than oxygen. In addition, the effect of lowering the redox potential through the addition of a reducer to the growth medium was observed. The experiments proved that the formation of magnetosomes is inhibited at ORP 0 mV, whereas reduced conditions, ORP – 500 mV facilitate biomineralization process. The occurring trend can be confirmed by iron uptake measurements as well as via microscope observations. The results of iron uptake appear to be in line with previous experiments [57], nevertheless those analyzed the formation of magnetosomes at different concentrations of oxygen in the medium. It would be interesting to grow cell in our system, at stable ORP using oxygen as an oxidizer, what would allow more precise comparison with previous studies, since it is not clear which ORP level represents desired concentration of oxygen. The behavior of *M.magneticum* in relationship to ORP in its natural environment is also not clear. While magnetotactic bacteria are known to occur at the OATZ, they seem to reach higher cell densities at oxidized conditions.

Besides the results obtained, showing the effect of the ORP on the process of magnetosome formation, a need of deepen the effects of these compounds at a molecular level is necessary. The toxicity tests and the abnormal cell elongation suggest that those chemical could have effects on the cellular metabolism. Therefore, the differences in biomineralization rates and those effects might be strongly related. Interesting would be to investigate the molecular mechanisms of inhibition of magnetite synthesis and the reason that might propel it at lower redox. The mechanisms of action could be different and act at different levels. Either the gene expression could be modified, blocking the process because disturbing protein synthesis or other reasons could be connected with the change in the chemical affinity between the iron dissolved in the medium and the mechanisms of iron uptake.

The results presented in this thesis show a relationship between ORP and formation of magnetosome in *M.magneticum* AMB-1 strain; providing a base for further analysis on the

relationship between ORP and magnetotactic bacteria. AMB-1 cell under reduced conditions produce longer chains of magnetosomes and magnetosomes itself exhibit bigger sizes. The chains formed under oxidized conditions are shorter and crystals formed possess dwarfed forms, what implies that indeed the redox state of the surrounding medium has a strong impact on the formation of magnetosome chains in AMB-1 strain.

The controlled assembly of magnetite nanoparticles on the phage baseplate was the second aim of work presented. The assembly of PEI nanoparticles on WT phage was possible due to the electrostatic interactions between the positively charged PEI nanoparticles and negatively charged phage filaments. Even though zeta potential measurements showed that the stable interaction between molecules differs when depend on the ionic strength, it was still possible to achieve stable assembly. As shown by replacing water by borate buffer, the charge difference at neutral pH slightly decreased but still enabled stable binding. The particles appear to be randomly bound to the filament. Therefore, it would be necessary to systematize the amount of nanoparticles attaching to the phage. It was demonstrated as well that it is possible to effectively actuate random phages - nanoparticles assemblies by applying external magnetic fields. The structures were flexible, changing the shape while propelling, but relatively slow, comparing to other propellers described [153]. It is necessary though to perform time lapse experiments showing that the smaller the assemblies are, the faster they swim or propel. The same rule applies to flagellum like swimmer. Even if the phage particles were detected by fluorescence techniques, due to their small size, it was not possible to determine the swimming speeds. Several open questions and challenges remain. It is interesting to develop the technique that enables the visualization of such a small nanoobjects and their behavior in the external magnetic fields. Exploring the relationship between the geometry and propulsion properties would be another task to fulfil. Although it is a preliminary result, phage based assemblies are a promising tool for its usage in especially medical applications as drug carriers or delivering systems [160]. These potential swimmers could carry drugs or other small molecules at specific locations. Even if the smallest collected swimmers were difficult to control, it was shown that bigger, visible aggregates can be controlled in the magnetic field, which implies the possibility of controlled manipulation of their swimming directions. On the other hand increasing the amount of magnetite nanoparticles delivered could strengthen the localized heating and improve hyperthermia treatment [161].

5. Bibliography

[1] D. Ghosh, Y. Lee, S. Thomas, A. G. Kohli, D. S. Yun, A. M. Belcher, and K. a Kelly, "M13-templated magnetic nanoparticles for targeted in vivo imaging of prostate cancer.," *Nat. Nanotechnol.*, vol. 7, no. 10, pp. 677–82, Oct. 2012.

[2] S. Dey and T. K. Maiti, "Superparamagnetic Nanoparticles and RNAi-Mediated Gene Silencing: Evolving Class of Cancer Diagnostics and Therapeutics," *J. Nanomater.*, vol. 2012, pp. 1–15, 2012.

[3] J. Baumgartner, A. Dey, P. H. H. Bomans, C. Le Coadou, P. Fratzl, N. a J. M. Sommerdijk, and D. Faivre, "Nucleation and growth of magnetite from solution.," *Nat. Mater.*, vol. 12, no. 4, pp. 310–4, Apr. 2013.

[4] P. Y. Keng, I. Shim, B. D. Korth, J. F. Douglas, and J. Pyun, "Synthesis and Self-Assembly of Polymer-Coated Ferromagnetic Nanoparticles," *ACS Nano*, vol. 1, no. 4, pp. 279–292, Nov. 2007.

[5] X. Batlle and A. Labarta, "Finite-size effects in fine particles: magnetic and transport properties," *J. Phys. D. Appl. Phys.*, vol. 35, p. R–15_R42, 2002.

[6] M. Roper, R. Dreyfus, J. Baudry, M. Fermigier, J. Bibette, and H. a Stone, "Do magnetic micro-swimmers move like eukaryotic cells?," *Proc. R. Soc. A Math. Phys. Eng. Sci.*, vol. 464, no. 2092, pp. 877–904, Apr. 2008.

[7] C. Goubault, P. Jop, M. Fermigier, J. Baudry, E. Bertrand, and J. Bibette, "Flexible Magnetic Filaments as Micromechanical Sensors," *Phys. Rev. Lett.*, no. 91, pp. 260802/1–260802/4, 2003.

[8] S. Weiner, "An Overview of Biomineralization Processes and the Problem of the Vital Effect," *Rev. Mineral. Geochemistry*, vol. 54, pp. 1–29, 2001.

[9] S. Weiner, R. Israel, P. M. Dove, V. Tech, and U. S. A. Virginia, "An Overview of Biomineralization Processes and the Problem of the Vital Effect," pp. 1–29, 2001.

[10] R. B. Frankel, "Iron biominerals: an overview," *Springer US*, no. fable 2, pp. 1–6, 1991.

[11] D. a. Bazylinski, "Biologically Controlled Mineralization in Prokaryotes," *Rev. Mineral. Geochemistry*, vol. 54, no. 1, pp. 217–247, Jan. 2003.

[12] Y. A. Gorby, T. J. Beveridge, and R. P. Blakemore, "Characterization of the bacterial magnetosome membrane.," *J. Bacteriol.*, vol. 170, no. 2, pp. 834–841, Feb. 1988.

[13] S. R. Whaley, D. S. English, E. L. Hu, P. F. Barbara, and A. M. Belcher, "Selection of peptides with semiconductor binding speci ® city for directed nanocrystal assembly," *Nature*, no. 100, pp. 665–668, 2000.

[14] J.-W. Oh, W.-J. Chung, K. Heo, H.-E. Jin, B. Y. Lee, E. Wang, C. Zueger, W. Wong, J. Meyer, C. Kim, S.-Y. Lee, W.-G. Kim, M. Zemla, M. Auer, A. Hexemer, and S.-W. Lee, "Biomimetic virus-based colourimetric sensors," *Nat. Commun.*, vol. 5, pp. 1–8, Jan. 2014.

[15] T. Wang, G. D'Souza, D. Bedi, Q. Faqbohun, L. Potturi, B. Papahadjopoulos-Sternberg, V. Petrenko, and V. Torchilin, "Enhanced binding and killing of target tumor cells by drug-loaded liposomes modified with tumor-specific phage fusion coat protein," *Nanomedicine*, pp. 563–74, 2010.

[16] G. P. Smith and V. a. Petrenko, "Phage Display.," *Chem. Rev.*, vol. 97, no. 2, pp. 391–410, Apr. 1997.

[17] R. R. Riddle, R. C. Willson, and M. J. Benedik, "Temperature- and solvent-tolerant mutants of filamentous bacteriophage helper M13 KO7," *Biotechnol. Lett.*, vol. 21, no. 1, pp. 87–90, 1999.

[18] A. Servant, F. Qiu, M. Mazza, K. Kostarelos, and B. J. Nelson, "Controlled In Vivo Swimming of a Swarm of Bacteria-Like Microrobotic Flagella," *Adv. Mater.*, vol. 27, no. 19, pp. 2981–2988, May 2015.

[19] I. Paprotny and R. Goebel, *Small-Scale Robotics*. 2013.

[20] B. R. Donald, C. G. Levey, C. D. Mcgray, I. Paprotny, and D. Rus, "An Untethered , Electrostatic , Globally Controllable," vol. 15, no. 1, pp. 1–15, 2006.

[21] P. Wagler, "Dynamical multiphase structures in the microsystem approach to artificial cells," in *MicroTas*, 2005.

[22] D. Faivre and D. Schüler, "Magnetotactic bacteria and magnetosomes.," *Chem. Rev.*, vol. 108, no. 11, pp. 4875–98, Nov. 2008.

[23] R. B. Frankel and D. A. Bazylinski, "Biologically Induced Mineralization by Bacteria," 2003.

[24] Y. A. Gorby, T. J. Beveridge, and R. P. Blakemore, "Characterization of the Bacterial Magnetosome Membrane," vol. 170, no. 2, pp. 834–841, 1988.

[25] S. Bellini, "Further studies on 'magnetosensitive bacteria'.," *Chinese J. Oceanol. Limnol.*, 2009.

[26] S. Bellini, "On a unique behavior of freshwater bacteria," *Chinese J. Oceanol. Limnol.*, 2009.

[27] R. Blakemore, "Magnetotactic Bacteria," *Science (80-.).*, no. October, pp. 1–3, 1975.

[28] Keim et al., "Cell organization and ultrastructure of a magnetotactic multicellular organism.," *J. Struct. Biol.*, vol. 145, no. 3, pp. 254–62, Mar. 2004.

[29] Bazylinski et al, *Nanomicrobiology*. 2014.

[30] D. A. Bazylinski and T. Williams, "Ecophysiology of Magnetotactic Bacteria," in *Magnetoreception and Magnetosomes in Bacteria*, no. September, 2007.

[31] B. H. Lower and D. a Bazylinski, "The bacterial magnetosome: a unique prokaryotic organelle.," *J. Mol. Microbiol. Biotechnol.*, vol. 23, no. 1–2, pp. 63–80, Jan. 2013.

[32] L. Rahn-Lee and A. Komeili, "The magnetosome model: insights into the mechanisms of bacterial biomineralization.," *Front. Microbiol.*, vol. 4, no. November, p. 352, Jan. 2013.

[33] D. Schüler, "Genetics and cell biology of magnetosome formation in magnetotactic bacteria.," *FEMS Microbiol. Rev.*, vol. 32, no. 4, pp. 654–72, Jul. 2008.

[34] M. Amor, V. Busigny, M. Durand-Dubief, M. Tharaud, G. Ona-Nguema, A. Gélabert, E. Alphandéry, N. Menguy, M. F. Benedetti, I. Chebbi, and F. Guyot, "Chemical signature of magnetotactic bacteria.," *Proc. Natl. Acad. Sci. U. S. A.*, vol. 112, no. 6, pp. 1699–703, Feb. 2015.

[35] A. et al. Komeili, "Magnetosomes are cell membrane invaginations organized by the actin-like protein MamK," *Science (80-.).*, vol. 311, no. January, pp. 242–246, 2006.

[36] M. Winklhofer and N. Petersen, "Magnetoreception and magnetosomes in bacteria," *Springer US*, vol. 3, p. 255, 2007.

[37] D. Schüler and R. B. Frankel, "Bacterial magnetosomes : microbiology , biomineralization and biotechnological applications," 1999.

[38] X. I. N. H. Ua, D. E. A. B. Azylinski, B. E. D. Evouard, M. Iha, R. I. B. F. Rankel, and P. E. R. B. Useck, "Magnetite from magnetotactic bacteria : Size distributions and twinning," vol. 83, pp. 1387–1398, 1998.

[39] C. et al. Moisescu, "The effect and role of environmental conditions on magnetosome synthesis.," *Front. Microbiol.*, vol. 5, no. February, p. 49, Jan. 2014.

[40] B. Kiani, D. Faivre, and S. Klumpp, "Elastic properties of magnetosome chains," *New J. Phys.*, vol. 17, no. 4, p. 043007, Apr. 2015.

[41] A. P. Philipse and D. Maas, "Magnetic Colloids from Magnetotactic Bacteria : Chain Formation and Colloidal Stability," no. 11, pp. 9977–9984, 2002.

[42] A. Scheffel, M. Gruska, D. Faivre, A. Linaroudis, J. M. Plitzko, and D. Schüler, "An acidic protein aligns magnetosomes along a filamentous structure in magnetotactic bacteria.," *Nature*, vol. 440, no. 7080, pp. 110–4, Mar. 2006.

[43] A. Derman, E. Becker, B. Truong, A. Fujioka, T. Tucey, M. Erb, P. Patterson, and J. Pogliano, "Phylogenetic analysis identifies many uncharacterized actin-like proteins (Alps) in bacteria: regulated polymerization, dynamic instability and treadmilling in Alp7A.," *Mol. Microbiol.*, vol. 73, pp. 534–552, 2009.

[44] A. Komeili, Z. Li, D. K. Newman, and G. J. Jensen, "Magnetosomes are cell membrane invaginations organized by the actin-like protein MamK.," *Science*, vol. 311, pp. 242–245, 2006.

[45] E. Katzmann, A. Scheffel, M. Gruska, J. M. Plitzko, and D. Schüler, "Loss of the actin-like protein MamK has pleiotropic effects on magnetosome formation and chain assembly in Magnetospirillum gryphiswaldense," *Mol. Microbiol.*, vol. 77, no. 1, pp. 208–224, Jul. 2010.

[46] S. Klumpp and D. Faivre, "Interplay of magnetic interactions and active movements in the formation of magnetosome chains.," *PLoS One*, vol. 7, no. 3, p. e33562, Jan. 2012.

[47] T. Matsunaga, T. Suzuki, M. Tanaka, and A. Arakaki, "Molecular analysis of magnetotactic bacteria and development of functional bacterial magnetic particles for nano-biotechnology.," *Trends Biotechnol.*, vol. 25, no. 4, pp. 182–8, Apr. 2007.

[48] T. Suzuki, Y. Okamura, R. J. Calugay, H. Takeyama, and T. Matsunaga, "Global gene expression analysis of iron-inducible genes in Magnetospirillum magneticum AMB-1.," *J. Bacteriol.*, vol. 188, no. 6, pp. 2275–9, Mar. 2006.

[49] D. Faivre, L. H. Böttger, B. F. Matzanke, and D. Schüler, “Intracellular magnetite biomineralization in bacteria proceeds by a distinct pathway involving membrane-bound ferritin and an iron(II) species.,” *Angew. Chem. Int. Ed. Engl.*, vol. 46, no. 44, pp. 8495–9, Jan. 2007.

[50] D. A. Bazylinski, C. T. Lefèvre, and B. H. Lower, *Nanomicrobiology*. New York, NY: Springer New York, 2014.

[51] J. Baumgartner, G. Morin, N. Menguy, T. Perez Gonzalez, M. Widdrat, J. Cosmidis, and D. Faivre, “Magnetotactic bacteria form magnetite from a phosphate-rich ferric hydroxide via nanometric ferric (oxyhydr)oxide intermediates.,” *Proc. Natl. Acad. Sci. U. S. A.*, vol. 110, no. 37, pp. 14883–8, Sep. 2013.

[52] H. Nudelman and R. Zarivach, “Structure prediction of magnetosome-associated proteins.,” *Front. Microbiol.*, vol. 5, no. January, p. 9, Jan. 2014.

[53] D. Schüler and E. Baeuerlein, “Iron-limited growth and kinetics of iron uptake in Magnetospirillum gryphiswaldense,” *Arch. Microbiol.*, vol. 166, no. 5, pp. 301–307, Nov. 1996.

[54] D. Schüler and E. Baeuerlein, “Dynamics of Iron Uptake and Fe 3 O 4 Biomineralization during Aerobic and Microaerobic Growth of Magnetospirillum gryphiswaldense,” vol. 180, no. 1, pp. 159–162, 1998.

[55] D. Faivre, N. Menguy, M. Posfai, and D. Schuler, “Environmental parameters affect the physical properties of fast-growing magnetosomes,” *Am. Mineral.*, vol. 93, no. 2–3, pp. 463–469, Feb. 2008.

[56] J. Li and Y. Pan, “Environmental Factors Affect Magnetite Magnetosome Synthesis in Magnetospirillum magneticum AMB-1: Implications for Biologically Controlled Mineralization,” *Geomicrobiol. J.*, vol. 29, no. 4, pp. 362–373, May 2012.

[57] U. Heyen and D. Schüler, “Growth and magnetosome formation by microaerophilic Magnetospirillum strains in an oxygen-controlled fermentor.,” *Appl. Microbiol. Biotechnol.*, vol. 61, no. 5–6, pp. 536–44, Jun. 2003.

[58] R. Popa, W. Fang, K. H. Nealson, V. Souza-egipsy, T. S. Berquó, S. K. Banerjee, and L. R. Penn, “Effect of oxidative stress on the growth of magnetic particles in Magnetospirillum magneticum,” pp. 49–57, 2009.

[59] K. Bagramyan, A. Galstyan, and A. Trchounian, “Redox potential is a determinant in the Escherichia coli anaerobic fermentative growth and survival: effects of impermeable oxidant,” *Bioelectrochemistry*, vol. 51, no. 2, pp. 151–156, Jun. 2000.

[60] C.-G. Liu, C. Xue, Y.-H. Lin, and F.-W. Bai, “Redox potential control and applications in microaerobic and anaerobic fermentations.,” *Biotechnol. Adv.*, vol. 31, no. 2, pp. 257–65, 2013.

[61] C. T. Lefèvre, M. Bennet, L. Landau, P. Vach, D. Pignol, D. a Bazylinski, R. B. Frankel, S. Klumpp, and D. Faivre, “Diversity of magneto-aerotactic behaviors and oxygen sensing mechanisms in cultured magnetotactic bacteria.,” *Biophys. J.*, vol. 107, no. 2, pp. 527–38, Jul. 2014.

[62] S. L. Simmons, D. A. Bazylinski, and K. J. Edwards, “South-Seeking Magnetotactic,” *Science (80-.).*, vol. 311, no. January, pp. 371–375, 2006.

[63] T. Matsunaga, T. Sakaguchi, and F. Tadakoro, “Magnetite formation by a magnetic bacterium capable of growing aerobically,” *Appl. Microbiol. Biotechnol.*, vol. 35, no. 5, Aug. 1991.

[64] T. Matsunaga and N. Tsujimura, “Respiratory inhibitors of a magnetic bacterium Magnetospirillum sp. AMB-1 capable of growing aerobically,” *Appl. Microbiol. Biotechnol.*, vol. 39, no. 3, Jun. 1993.

[65] F. Zhang, K. Yu-Zhang, S. Zhao, T. Xiao, M. Denis, and L. Wu, “Metamorphosis of Magnetospirillum magneticum AMB-1 cells,” *Chinese J. Oceanol. Limnol.*, vol. 28, no. 2, pp. 304–309, Mar. 2010.

[66] K. H. Schleifer, D. Schüler, S. Spring, M. Weizenegger, R. Amann, W. Ludwig, and M. Köhler, “The Genus Magnetospirillum gen. nov. Description of Magnetospirillum gryphiswaldense sp. nov. and Transfer of Aquaspirillum magnetotacticum to Magnetospirillum magnetotacticum comb. nov.,” *Syst. Appl. Microbiol.*, vol. 14, no. 4, pp. 379–385, Oct. 1991.

[67] D. Bazylinski and T. Williams, “Ecophysiology of magnetotactic bacteria,” *... magnetosomes Bact.*, no. September, 2007.

[68] B. F. Widdel F, “Gram-negative mesophilic sulfate reducing baacteria,” in *The Prokaryotes*, 2nd ed., Springer, 1992, pp. 3352–3378.

[69] D. Schüler, R. Uhl, and B. Edmund, “A simple light scattering method to assay magnetism in Magnetospirillum gryphiswaldense,” vol. 132, no. I 995, pp. 139–145, 1995.

[70] L. et al. Day, “Familly Inoviriadae.,” *Virus Taxon. Nomencl. VirusesNinth Rep. Int. Commettee Taxon. Viruses*, 2011.

[71] J. Rakonjac, “Filamentous Bacteriophages: Biology and Applications,” *eLS*, 2012.

[72] G. P. Smith, “The Phage Nanoparticle Toolkit,” in *Phage Nanobiotechnology*, no. 17, 2011, pp. 1–11.

[73] G. Iannolo, O. Minenkova, R. Petruzzelli, and G. Cesareni, “Modifying filamentous phage capsid: limits in the size of the major capsid protein.,” *J. Mol. Biol.*, vol. 248, no. 4, pp. 835–44, May 1995.

[74] S. S. Sidhu, “Engineering M13 for phage display.,” *Biomol. Eng.*, vol. 18, no. 2, pp. 57–63, Sep. 2001.

[75] L. Chasteen, J. Ayriss, P. Pavlik, and a R. M. Bradbury, “Eliminating helper phage from phage display.,” *Nucleic Acids Res.*, vol. 34, no. 21, p. e145, Jan. 2006.

[76] J. Rakonjac, N. J. Bennett, J. Spagnuolo, D. Gagic, and M. Russel, “Filamentous bacteriophage: biology, phage display and nanotechnology applications.,” *Curr. Issues Mol. Biol.*, vol. 13, no. 2, pp. 51–76, Jan. 2011.

[77] et al. Huang, “Programmable assembly of nanoarchitectures using genetically engineered viruses.,” *Nano Lett.*, 2005.

[78] C. Mao, D. J. Solis, B. D. Reiss, S. T. Kottmann, R. Y. Sweeney, A. Hayhurst, G. Georgiou, B. Iverson, and A. M. Belcher, “Virus-based toolkit for the directed synthesis of magnetic and semiconducting nanowires.,” *Science*, vol. 303, no. 5655, pp. 213–7, Jan. 2004.

[79] J. Y. et al. Lee, “Fabricating genetically engineered high power lithium ion batteries using multiple virus genes,” *Science (80-.).*, no. May, pp. 1051–1056, 2009.

[80] W.-J. Chung, J.-W. Oh, K. Kwak, B. Y. Lee, J. Meyer, E. Wang, A. Hexemer, and S.-W. Lee, “Biomimetic self-templating supramolecular structures.,” *Nature*, vol. 478, no. 7369, pp. 364–8, Oct. 2011.

[81] J. Baumgartner, M. A. Carillo, K. M. Eckes, P. Werner, and D. Faivre, “Biomimetic magnetite formation: from biocombinatorial approaches to mineralization effects.,” *Langmuir*, vol. 30, no. 8, pp. 2129–36, Mar. 2014.

[82] L. Yang, X.-H. Peng, Y. A. Wang, X. Wang, Z. Cao, C. Ni, P. Karna, X. Zhang, W. C. Wood, X. Gao, S. Nie, and H. Mao, “Receptor-targeted nanoparticles for in vivo imaging of breast cancer.,” *Clin. Cancer Res.*, vol. 15, no. 14, pp. 4722–32, Jul. 2009.

[83] A. Pollithy, T. Romer, C. Lang, F. D. Müller, J. Helma, H. Leonhardt, U. Rothbauer, and D. Schüler, “Magnetosome expression of functional camelid antibody fragments (nanobodies) in Magnetospirillum gryphiswaldense.,” *Appl. Environ. Microbiol.*, vol. 77, no. 17, pp. 6165–71, Sep. 2011.

[84] J. Speck, K. M. Arndt, and K. M. Müller, “Efficient phage display of intracellularly folded proteins mediated by the TAT pathway.,” *Protein Eng. Des. Sel.*, vol. 24, no. 6, pp. 473–84, Jun. 2011.

[85] J. Baumgartner, “Nucleation and Growth of Magnetite Nanoparticles under Biomimetic Conditions,” 2011.

[86] J. J. Abbott, K. E. Peyer, M. C. Lagomarsino, L. Zhang, L. Dong, I. K. Kaliakatsos, and B. J. Nelson, “How Should Microrobots Swim?,” *Int. J. Rob. Res.*, vol. 28, no. 11–12, pp. 1434–1447, Jul. 2009.

[87] P. Fischer and A. Gosh, “Magnetically actuated propulsion at low Reynolds numbers: towards nanoscale control.,” *Nanoscale*, vol. 3(2), pp. 557–563, 2011.

[88] M. Zeeshan, S. Pane, S. Youn, E. Pellicer, S. Schuerle, J. Sort, S. Fusco, A. Lindo, H. Park, and B. Nelson, “Graphite Coating of Iron Nanowires for Nanorobotic Applications: Synthesis, Characterization and Magnetic Wireless Manipulation.,” *Adv. Funct. Mater.*, vol. 23, no. 7, pp. 823–831, 2013.

[89] S. Kim, F. Qiu, A. Ghanbari, C. Moon, L. Zhang, B. Nelson, and H. Choi, “Characerization of Magnetic Microrobots for Three-Dimensional Cell Culture and Targeted Transportation,” *Adv. Mater.*, vol. 25, no. 41, pp. 863–5868, 2013.

[90] P. Vach, “Solution synthesis and actuation of magnetic nanostructures,” 2014.

[91] R. Dreyfus, J. Baudry, M. Roper, H. Fermigier, H. Stone, and J. Bibette, “Microscopic artificial swimmers,” *Nature*, vol. 437, no. 7060, pp. 862–865, 2005.

[92] L. Zhang, J. J. Abbott, L. Dong, B. E. Kratochvil, D. Bell, and B. J. Nelson, “Artificial bacterial flagella: Fabrication and magnetic control,” *Appl. Phys. Lett.*, vol. 94, no. 6, p. 064107, 2009.

[93] A. Ghosh and P. Fischer, “Controlled propulsion of artificial magnetic nanostructured propellers.,” *Nano Lett.*, vol. 9, no. 6, pp. 2243–5, Jun. 2009.

[94] W. Gao, S. Sattayasamitsathit, K. Manesh, D. Weihs, and J. Wang, “Magnetically Powered Flexible Metal Nanowire Motors.,” *J. Am. Chem. Soc.*, vol. 132, no. 41, pp. 14403–14405, 2010.

[95] O. Pak, W. Gao, J. Wang, and E. Lauga, “High-speed propulsion of flexible nanowire motors:Theory and experiments.,” *Soft Matter*, vol. 7, no. 18, pp. 8169–8181, 2011.

[96] B. Nelson, I. Kalikatsos, and J. Abbott, “Microrobos for minimally invasive medicine.,” *Annu. Rev. Biomed. Eng.*, no. 12, pp. 55–85, 2010.

[97] W. Gao and J. Wang, “The Environmental Impact of Micro/Nanomachones.,” *ACS Nano*, 2014.

[98] Z. Ye and M. Sitti, “Dynamic trapping and two-dimensional transport of swimming microorganisms using a rotating magnetic microrobot.,” *Lab Chip*, 2014.

[99] D. Ghosh, Y. Lee, S. Thomas, A. G. Kohli, D. S. Yun, A. M. Belcher, and K. A. Kelly, “M13-templated magnetic nanoparticles for targeted in vivo imaging of prostate cancer,” *Nat. Nanotechnol.*, vol. 7, no. 10, pp. 677–682, 2012.

[100] J. Townsend, R. Burtovyy, Y. Galabura, and I. Luzinov, “Flexible Chains of Ferromagnetic Nanoparticles.,” *ACS Nano*, no. 7, pp. 6970–6978, Jun. 2014.

[101] A. Cebers, “Flexible Magnetic Filaments,” *Curr. Opin. Colloid Interface Sci*, no. 10, pp. 167–175, 2005.

[102] S. Biswal and A. Gast, “Mechanics of Semiflexible Chains Formed by Poly(ethylene-glycol)-Linked Paramagnetic Particles,” *Phys. Rev E*, no. 68, pp. 021402/1–021402/9, 2003.

[103] J. A. Gough and N. E. Murray, “Sequence diversity among related genes for recognition of specific targets in DNA molecules,” *J.Mol.Biol.*, 1983.

[104] K. Noren and C. Noren, “Construction of high-complexity combinatorial phage display peptide libraries.,” *Methods*, 2001.

[105] J. Sambrook, *Molecular cloning: a laboratory manual*. 1989.

[106] J. Sambrook and D. W. Russell, *Molecular Cloning: A Laboratory Manual*, 3rd ed. Cold Spring Harbor: Cold Spring Harbor Laboratory Press, 2001, pp. 3.17–3.32.

[107] R. L. Wiseman, S. A. Berkowitz, and A. Day, “Different Arrangements of Protein Subunits and Single-stranded Circular DNA in the Filamentous Bacterial Viruses fd and Pf 1,” 1976.

[108] X. Hou and B. T. Jones, “Inductively Coupled Plasma / Optical Emission Spectrometry,” pp. 9468–9485, 2000.

[109] T. Ferreira and W. Rasband, *ImageJ User Guide*. .

[110] O. Paris, C. Li, S. Siegel, G. Weseloh, F. Emmerling, H. Riesemeier, A. Erko, and P. Fratzl, “A new experimental station for simultaneous X-ray microbeam scanning for small- and wide-angle scattering and fluorescence at BESSY II,” *J. Appl. Cryst.*, vol. 40, pp. 466–470, 2007.

[111] M. Schmitz, “High-resolution synchrotron x-ray scattering reveals the difference in the ultrastructure of biogenic and abiotic magnetite nanoparticles,” Berlin, 2010.

[112] A. Hammersley, “The FIT2D Home Page,” 2004. [Online]. Available: http://www.esrf.eu/computing/scientific/FIT2D/.

[113] C. Lee, “AutoFit.” .

[114] A. Patterson, “The Scherrer Formula for X-Ray Particle Size Determination,” *Phys. Rev.*, vol. 56, pp. 978–982, 1939.

[115] A. A. Khan, “Tobacco Mosaic Virus (TMV) as a nanoscaffold for inorganic assemblies,” University of Basque Country, 2012.

[116] *Zetasizer Nano Series*. 2005.

[117] D. Nečas and P. Klapetek, “Gwyddion: an open-source software for SPM data analysis,” *Cent. Eur. J. Phys.*, vol. 10, no. 1, pp. 181–188, Nov. 2011.

[118] M. Bennet, “Influence of magnetic fields on magneto-aerotaxis.,” *PLoS One*, 2014.

[119] M. Bennet, A. McCarthy, D. Fix, M. R. Edwards, F. Repp, P. Vach, J. W. C. Dunlop, M. Sitti, G. S. Buller, S. Klumpp, and D. Faivre, “Influence of magnetic fields on magneto-aerotaxis.,” *PLoS One*, vol. 9, no. 7, p. e101150, Jan. 2014.

[120] R. P. Blakemore, D. Maratea, and R. S. Wolfe, “Isolation and Pure Culture of a Freshwater Magnetic Spirillum in Chemically Defined Medium,” *J.Bacteriol*, vol. 140, no. 2, pp. 720–729, 1979.

[121] A. Zehnder and W. Wuhrmann, “Titanium (III) Citrate as a Nontoxic Oxidation-Reduction Buffering System for the Culture of Obligate Anaerobes,” *Science (80-.).*, 1976.

[122] S. S. Staniland, C. Moisescu, and L. G. Benning, “Cell division in magnetotactic bacteria splits magnetosome chain in half.,” *J. Basic Microbiol.*, vol. 50, no. 4, pp. 392–6, Aug. 2010.

[123] D. Murat, A. Quinlan, H. Vali, and A. Komeili, “Comprehensive genetic dissection of the magnetosome gene island reveals the step-wise assembly of a prokaryotic organelle.,” *Proc. Natl. Acad. Sci. U. S. A.*, vol. 107, no. 12, pp. 5593–8, Mar. 2010.

[124] X. I. N. H. Ua, D. E. A. B. Azylinski, B. E. D. Evouard, M. Iha, R. I. B. F. Rankel, and P. E. R. B. Useck, “Magnetite from magnetotactic bacteria : Size distributions and twinning,” vol. 83, pp. 1387–1398, 1998.

[125] D. a. Bazylinski, “Biologically Controlled Mineralization in Prokaryotes,” *Rev. Mineral. Geochemistry*, vol. 54, no. 1, pp. 217–247, Jan. 2003.

[126] R. Blakemore, K. Short, D. Bazylinski, C. Rosenblatt, and R. Frankel, “Microaerobic conditions are required for magnetite formation within Aquaspirillum magnetotacticum.,” *Geomicrobiol. J.*, vol. 4, pp. 53–71, 1985.

[127] C. Jogler and D. Schüler, “Genomics, genetics, and cell biology of magnetosome formation.,” *Annu. Rev. Microbiol.*, vol. 63, pp. 501–21, Jan. 2009.

[128] G. a Jones and M. D. Pickard, “Effect of titanium (III) citrate as reducing agent on growth of rumen bacteria.,” *Appl. Environ. Microbiol.*, vol. 39, no. 6, pp. 1144–7, Jun. 1980.

[129] O. N. Oktyabrsky and G. V. Smirnova, “Dynamics of Redox Potential in Bacterial Cultures Growing on Media Containing Different Sources of Carbon , Energy and Nitrogen,” vol. 9, pp. 203–209, 1989.

[130] E. Alphandéry, S. Faure, O. Seksek, F. Guyot, and I. Chebbi, “Chains of magnetosomes extracted from AMB-1 magnetotactic bacteria for application in alternative magnetic field cancer therapy.,” *ACS Nano*, vol. 5, no. 8, pp. 6279–96, Aug. 2011.

[131] E. Alphandéry, M. Amor, F. Guyot, and I. Chebbi, “The effect of iron-chelating agents on Magnetospirillum magneticum strain AMB-1: stimulated growth and magnetosome production and improved magnetosome heating properties.,” *Appl. Microbiol. Biotechnol.*, vol. 96, no. 3, pp. 663–70, Nov. 2012.

[132] C. Moisescu, I. I. Ardelean, and L. G. Benning, “The effect and role of environmental conditions on magnetosome synthesis.,” *Front. Microbiol.*, vol. 5, no. February, p. 49, Jan. 2014.

[133] K. D. Young, “The selective value of bacterial shape.,” *Microbiol. Mol. Biol. Rev.*, vol. 70, no. 3, pp. 660–703, Sep. 2006.

[134] E. Katzmann, F. D. Müller, C. Lang, M. Messerer, M. Winklhofer, J. M. Plitzko, and D. Schüler, “Magnetosome chains are recruited to cellular division sites and split by asymmetric septation.,” *Mol. Microbiol.*, vol. 82, no. 6, pp. 1316–29, Dec. 2011.

[135] J. Green and M. S. Paget, “Bacterial redox sensors.,” *Nat. Rev. Microbiol.*, vol. 2, no. 12, pp. 954–66, Dec. 2004.

[136] H. Tamegai and Y. Fukumori, “Magnetospirillum magnetotacticum,” vol. 347, pp. 22–26, 1994.

[137] A. M. N. Silva, X. Kong, M. C. Parkin, R. Cammack, and R. C. Hider, “Iron(III) citrate speciation in aqueous solution.,” *Dalton Trans.*, no. 40, pp. 8616–25, Oct. 2009.

[138] T. C. Johnstone and E. M. Nolan, “Beyond iron: non-classical biological functions of bacterial siderophores.,” *Dalton Trans.*, vol. 44, no. 14, pp. 6320–39, Apr. 2015.

[139] T. Hunter, L. Esser, D. Van Der Helm, and J. Deisenhofer, “Structural Basis of Gating by the Outer Membrane Transporter FecA,” *Science (80-.).*, vol. 295, no. March, pp. 1715–1720, 2002.

[140] R. J. Calugay, Y. Okamura, A. T. Wahyudi, H. Takeyama, and T. Matsunaga, “Siderophore production of a periplasmic transport binding protein kinase gene defective mutant of Magnetospirillum magneticum AMB-1.,” *Biochem. Biophys. Res. Commun.*, vol. 323, no. 3, pp. 852–7, Oct. 2004.

[141] B. T. Volwne, “BIOTECHNOLOGY TECHNIQUES Volwne 10 No.7 (July 1996) p.495500 Received 7th May.,” vol. 7, no. 7, pp. 495–500, 1996.

[142] T. Matsunaga, H. Togo, T. Kikuchi, and T. Tanaka, “Production of luciferase-magnetic particle complex by recombinant Magnetospirillum sp. AMB-1,” *Biotechnol. Bioeng.*, vol. 70, no. 6, pp. 704–709, Dec. 2000.

[143] Y. Liu, G. R. Li, F. F. Guo, W. Jiang, Y. Li, and L. J. Li, “Large-scale production of magnetosomes by chemostat culture of Magnetospirillum gryphiswaldense at high cell density.,” *Microb. Cell Fact.*, vol. 9, p. 99, Jan. 2010.

[144] W. F. Guerint and R. P. Blakemore, “Redox Cycling of Iron Supports Growth and Magnetite Synthesis by Aquaspirillum magnetotacticum,” vol. 58, no. 4, pp. 1102–1109, 1992.

[145] C. Yang, H. Takeyama, and T. Matsunaga, “Iron feeding optimization and plasmid stability in production of recombinant bacterial magnetic particles by Magnetospirillum magneticum AMB-1 in fed-batch culture,” *J. Biosci. Bioeng.*, vol. 91, no. 2, pp. 213–216, Jan. 2001.

[146] W. W. Yu, J. C. Falkner, C. T. Yavuz, and V. L. Colvin, “Synthesis of monodisperse iron oxide nanocrystals by thermal decomposition of iron carboxylate salts.,” *Chem. Commun. (Camb).*, no. 20, pp. 2306–7, Oct. 2004.

[147] “NanoTech Ocean.” [Online]. Available: https://www.oceannanotech.com/spec.php?cid=69&pid=126&s_id=847.

[148] W. Chung, “Chemical modulation of M13 bacteriophage and its functional opportunities for nanomedicine,” pp. 5825–5836, 2014.

[149] P. J. Vach and D. Faivre, “The triathlon of magnetic actuation: rolling, propelling, swimming with a single magnetic material.,” *Sci. Rep.*, vol. 5, p. 9364, Jan. 2015.

[150] C. Mao, D. J. Solis, B. D. Reiss, S. T. Kottmann, R. Y. Sweeney, A. Hayhurst, G. Georgiou, B. Iverson, and A. M. Belcher, “Virus-based toolkit for the directed synthesis of magnetic and semiconducting nanowires.,” *Science*, vol. 303, no. 5655, pp. 213–7, Jan. 2004.

[151] J. Labille and J. Brant, “R eview Stability of nanoparticles in water R eview,” vol. 5, pp. 985–998, 2010.

[152] L. Yang, H. Liang, T. E. Angelini, J. Butler, R. Coridan, J. X. Tang, and G. C. L. Wong, “Self-assembled virus-membrane complexes.,” *Nat. Mater.*, vol. 3, no. 9, pp. 615–9, Sep. 2004.

[153] P. J. Vach, N. Brun, M. Bennet, L. Bertinetti, M. Widdrat, J. Baumgartner, S. Klumpp, P. Fratzl, and D. Faivre, “Selecting for function: solution synthesis of magnetic nanopropellers.,” *Nano Lett.*, vol. 13, no. 11, pp. 5373–8, Nov. 2013.

[154] S. Hagen, T. Baumann, H. J. Wagner, V. Morath, B. Kaufmann, A. Fischer, S. Bergmann, P. Schindler, K. M. Arndt, and K. M. Müller, “Modular adeno-associated virus (rAAV) vectors used for cellular virus-directed enzyme prodrug therapy.,” *Sci. Rep.*, vol. 4, p. 3759, Jan. 2014.

[155] G. Vemuri, E. Altman, D. Sangurdekar, A. Khodursky, and M. Eiteman, “Overflow metabolism in Escherichia coli during steady-state growth: transcriptional regulation and effect of the redox ratio,” *Appl. Environ. Microbiol.*, vol. 72, pp. 3653–61, 2006.

[156] C. Riondet, R. Cachon, Y. Wache, G. Alcaraz, and C. Divies, “Extracellular oxidoreduction potential modifies carbon and electron flow in Escherichia coli.,” *J. Bacteriol.*, vol. 182, pp. 620–6, 2000.

[157] P. E. Bell, A. L. Mills, and J. S. Herman, “Biogeochemical conditions favoring magnetite formation during anaerobic iron reduction.,” *Appl. Environ. Microbiol.*, vol. 53, pp. 2610–2616, 1987.

[158] L. Girbal, “How neutral red modified carbon and electron flow in Clostridium acetobutylicum grown in chemostat culture at neutral pH,” *FEMS Microbiol. Rev.*, vol. 16, pp. 151–62, 1995.

[159] S. Peguin and P. Soucaille, “Modulation of metabolism of Clostridium acetobutylicum grown in chemostat culture in a three-electrode potentiostatic system with methyl viologen,” *Biotechnol. Bioeng.*, no. 51, pp. 342–8, 1996.

[160] S. Tottori, L. Zhang, F. Qiu, K. Krawczyk, A. Franco-Obregon, and B. Nelson, “Magnetic helical micromachines: Fabrication, Controlled Swimming, and Cargo Transport.,” *Adv. Mater.*, vol. 26, no. 6, pp. 811–816, 2012.

[161] M. Babincova, V. Altanerova, C. Altaner, P. Cicmanec, and P. Babinec, “In vivo heating of magnetic nanoparticles in alternating magnetic field,” *Med. Phys.*, vol. 31, no. 8, pp. 2219–2221, 2004.

6. Appendix

Abbreviations

AMB-1	*Magnetospirillum magneticum*
AFM	Atomic Force Microscopy
Asp	Aspartate
C_{mag}	Coefficient of magnetically induced differential light scattering
Cm	Chloramphenicol
DLS	Dynamic Light Scattering
E.coli	*Escherichia coli*
EDTA	EthyleneDiamineTetraAcetic acid
EDX	X-ray spectroscopy
FSM	Flask standard medium
FWHM	Full width at half maximum
Fe	Iron
Glu	Glutamate
Hepes	4-(2-hydroxyethyl)-1-piperazineethanesulfonic acid
HR-TEM	High resolution transmission electron microscopy
IPTG	Isopropyl β-D-1-thiogalactopyranoside
ICP – OES	Inductively coupled plasma optical emission spectrometry
LB medium	Luria Bertani Medium
MQ-water	Milli-Q®-water
mam/Mam	Clas of genes, refers to magnetosome membrane/ respective proteins
ΔmamAB	Mutant of AMB-1 that does not produce magnetosomes
M	Molar
M13	Filamentous phage type

MD	Multidomain
MTB	Magnetotactic bacteria
MM	Magnetosome membrane
MSR-1	*Magnetospirillum gryphiswaldense*
mL	Milliliter
mM	Millimolar
mT	Mili-Tesla
nm	Nanometer
OD_{565}	Optical density at a wavelength of 565 nm
OATZ	Oxic anoxic transition zone
ORP	Oxidation-reduction potential
PEG	Polyethylene glycol
PEI NPs	Polyethylenimine nanoparticles
pH	Negative logarithm of molar concentration of hydronium ions in solution
pI	Isoelectric point
polyR	Poly-L-arginine
RT	Room temperature
RBP	Red fluorescent protein (RFP) – binding nanobody
SEM	Scanning Electron Microscopy
SD	Single domain
SP	Superparamagnetic
SSD	Stable single domain
TBS	Tris-buffered saline
TEM	Transmission Electron Microscopy
Tet	Tetracycline
WB	Washing buffer
XRD	X-ray diffraction

Eigentständigkeitserklärung

Hiermit versichere, dass ich die vorgelegte Arbeit eigenständig und nur unter Verwendunger angegenenen Literatur und Hilfsmittel erarbeitet und verfasst habe.

Agata Olszewska

Potsdam, September 2015

Acknowledgments

The work presented in this thesis would not be successfully achieved without help of many people. In the first place I would like to thank Dr. Damien Faivre for first of all believing in me and giving me a chance to join his group. Never endless support of Damien helped me to fulfill not only my scientific goals and to gain enormous knowledge on the topic of magnetite. Dr. Faivre also showed me how to become an independent and creative scientist and these lessons will remain forever in my memory.

I would like to acknowledge Prof. Peter Fratzl for giving me a change to work in Biomaterials Department and for creating amazing working atmosphere by uniting people who became not only my colleagues but also my close friends.

I would like to thank Prof. Katja Arndt form University of Potsdam for supervising me during these three years and for brainstorming discussions on the topic of bacteriophages.

I am very grateful to Dr. Mathieu Bennet, almost like a brother, Dr. Teresa P. Gonzalez, Dr. Maria Antonietta Carillo, Dr. Carmen Valverde Tercedor, my three favorite aunties, Dr. Jens Baumgartner (if you don't know.. ask Jens.. he always knows) that stood by and went through my writing process together with me. Special thanks go to Dr. Peter Vach for his never ending patience in explaining me the principles of magnetism.

I would like to thank my group, past and present members for making absolutely great working atmosphere. Many special thanks go to Katharina and Gabriele, my two master students. Without you, I would never fulfill all of the tasks. Extra pair of hands was very helpful. Many thanks to: Victoria, Livnat, Christophe, Janet, Erika, Clemens, Matt, Karin, Felix, Lena, Igor, Lorenzo, Roman (my formatting hero), Marie, Franzi, Luca, Admir, Nadya, Cecile, Tina, Yael, Bat-El, Osnat. You really made my time at the institute. Sara…I hope you survived the last weeks with me in the office. It must have been hard, but you are a huge part of this thesis too. Again many thanks to all of you Golmers!

But the biggest Dziękuję goes to my family. Bez Was nie udałoby się osiągnąć tego, co mam. Byliście dla mnie wsparciem każdego dnia. Tobie Marcu też dziękuję.